Global analysis of polarized DIS & SIDIS data with improved small-x helicity evolution

Daniel Adamiak,[1,2] Nicholas Baldonado,[3] Yuri V. Kovchegov,[1] W. Melnitchouk,[2] Daniel Pitonyak,[4] Nobuo Sato,[2] Matthew D. Sievert,[3] Andrey Tarasov,[5,6] and Yossathorn Tawabutr[7,8]

[1] *Department of Physics, The Ohio State University, Columbus, Ohio 43210, USA*
[2] *Jefferson Lab, Newport News, Virginia 23606, USA*
[3] *Department of Physics, New Mexico State University, Las Cruces, New Mexico 88003, USA*
[4] *Department of Physics, Lebanon Valley College, Annville, Pennsylvania 17003, USA*
[5] *Department of Physics, North Carolina State University, Raleigh, North Carolina 27695, USA*
[6] *Joint BNL-SBU Center for Frontiers in Nuclear Science (CFNS) at Stony Brook University, Stony Brook, New York 11794, USA*
[7] *Department of Physics, University of Jyväskylä, P.O. Box 35, 40014 University of Jyväskylä, Finland*
[8] *Helsinki Institute of Physics, P.O. Box 64, 00014 University of Helsinki, Finland*

Jefferson Lab Angular Momentum (JAM) Collaboration

(Dated: August 3, 2023)

We analyze the world polarized deep-inelastic scattering (DIS) and semi-inclusive DIS (SIDIS) data at low values of $x < 0.1$, using small-x evolution equations for the flavor singlet and nonsinglet helicity parton distribution functions (hPDFs). The hPDFs for quarks, antiquarks, and gluons are extracted and evolved to lower values of x to make predictions for the future Electron-Ion Collider (EIC). We improve on our earlier work by employing the more realistic large-N_c &N_f limit of the revised small-x helicity evolution, and incorporating running coupling corrections along with SIDIS data into the fit. We find an anti-correlation between the signs of the gluon and flavor-singlet quark hPDFs. While the existing low-x polarized DIS and SIDIS data are insufficient to constrain the initial conditions for the polarized dipole amplitudes in the helicity evolution equations, future EIC data will allow more precise predictions for hPDFs and the g_1 structure function for x values beyond those probed at the EIC. Using the obtained results, we discuss the contributions to the proton spin from quark and gluon spins at small x.

CONTENTS

I. INTRODUCTION

A. General motivation

The proton spin puzzle has been one of the most intriguing and profound mysteries in our understanding of the proton structure for over three decades (for reviews see Refs. [1–9]). The main challenge is to determine, both qualitatively and quantitatively, how the proton spin is distributed among the spins and orbital angular momenta (OAM) of its quark and gluon constituents. The question is usually formulated in terms of spin sum rules, such as the Jaffe-Manohar sum rule [10] (see also the Ji sum rule [11]), that decompose the proton spin of 1/2 (in units of $\hbar$) into the sum of the quark (S_q) and gluon (S_G) spins and the OAM carried by the quarks (L_q) and gluons (L_G),

$$S_q + L_q + S_G + L_G = \frac{1}{2}\,. \tag{1}$$

Each of the contributions in Eq. (1) can, in turn, be written as the integral of a partonic function over the longitudinal momentum fraction x carried by the parton. For example,

$$S_q(Q^2) = \frac{1}{2}\int_0^1 \mathrm{d}x\ \Delta\Sigma(x,Q^2)\,, \qquad\qquad S_G(Q^2) = \int_0^1 \mathrm{d}x\ \Delta G(x,Q^2)\,, \tag{2}$$

with similar expressions for the OAM contributions [12–16], where $\Delta\Sigma(x,Q^2)$ is the flavor singlet combination of the quark helicity parton distribution functions (hPDFs) $\Delta q(x,Q^2)$ (quark flavor q) and $\Delta G(x,Q^2)$ is the gluon hPDF [10]. The goal of current research in the field of proton spin physics is to determine $\Delta\Sigma(x,Q^2)$, $\Delta G(x,Q^2)$, $L_q(x,Q^2)$, and $L_G(x,Q^2)$ across a broad range of x and Q^2 in order to quantify how much of the proton spin is carried by the partons in different kinematic regions.

The standard way to address the proton spin puzzle is by extracting the hPDFs $\Delta q(x,Q^2)$ and $\Delta G(x,Q^2)$ from experimental data using collinear factorization along with the spin-dependent Dokshitzer-Gribov-Lipatov-Altarelli-Parisi (DGLAP) evolution equations [17–19] to relate observables at different Q^2. There has been a number of very successful extractions of hPDFs over the years within this approach [20–34]. Nevertheless, the DGLAP-based methodology has a drawback: since the DGLAP equations evolve PDFs in Q^2, they cannot truly predict the x dependence of PDFs. The x dependence is greatly affected by the functional form of the PDF parametrization at the initial momentum scale Q_0^2, which gives the initial conditions for the DGLAP evolution. The parameters are then determined by optimizing agreement between the theoretical calculations to the experimental measurements. In this way, the experimental data, in the x range where it is available, make up for the inability of DGLAP evolution to predict the x dependence of PDFs. Conversely, in the x region which has not yet been probed experimentally, DGLAP-based predictions typically acquire a broad uncertainty band due to extrapolation errors. This is particularly true in the small-x region. Since no experiment, present or future, can perform measurements down to $x = 0$, further theoretical input is needed to constrain the hPDFs at low x. The benefit of small-x helicity evolution is it makes a genuine prediction for the hPDFs at small x given some initial conditions at a higher x_0. Due to the integrals in Eq. (2), precise control over the behavior of hPDFs at small x is mandatory to resolving the proton spin puzzle.

B. Proton spin at small x

The first resummation of hPDFs at small x was performed in the pioneering work by Bartels, Ermolaev and Ryskin (BER) [35, 36], who employed the infrared evolution equations (IREE) formalism from Refs. [37–41]. The BER IREE resummed double logarithms of x, *i.e.* powers of the parameter $\alpha_s\,\ln^2(1/x)$ (with α_s the strong coupling constant),

which is referred to as the double-logarithmic approximation (DLA). The leading small-x asymptotics for the flavor singlet combination of quark hPDFs and the gluon hPDF can be written as

$$\Delta\Sigma(x,Q^2) \sim \Delta G(x,Q^2) \sim \left(\frac{1}{x}\right)^{\alpha_h}, \tag{3}$$

with α_h the helicity intercept. BER found $\alpha_h = 3.66\sqrt{\frac{\alpha_s N_c}{2\pi}}$ in the pure-gluon case and $\alpha_h = 3.45\sqrt{\frac{\alpha_s N_c}{2\pi}}$ for $N_f = 4$ (the numbers 3.66 and 3.45 were calculated numerically, the latter for $N_c = 3$, with N_c/N_f being the number of quark colors/flavors). These intercepts are numerically large, with $\alpha_h > 1$ for realistic coupling $\alpha_s = 0.2 - 0.3$, making the integrals (2) divergent as $x \to 0$. One may hope that the higher-order corrections in α_s, when calculated, would lower the intercept α_h below 1, making the integrals (2) convergent. In addition, at very small x, parton saturation corrections (see Refs. [42–49] for reviews) are likely to significantly modify the asymptotics (3) by slowing down (or completely stopping) the growth of hPDFs with decreasing x (see, *e.g.*, [50] for the impact of saturation effects on the unpolarized flavor nonsinglet evolution). Recently, the BER approach has been applied to the OAM distributions as well [51].

Over the past decade a new approach to helicity evolution at small x has been developed [52–65] employing the shock wave/s-channel evolution formalism originally constructed in Refs. [66–78] for unpolarized eikonal scattering. The main idea behind the works [52–65] is that the sub-eikonal, sub-sub-eikonal, etc., quantities obey small-x evolution equations similar to the eikonal ones [69–78], resulting from an s-channel gluon (or quark) cascade (see Refs. [57, 58, 79–92] for the formalism of sub-eikonal and sub-sub-eikonal evolution in high-energy scattering). The sub-eikonal quantities are suppressed by one power of x compared to the eikonal ones, sub-sub-eikonal quantities are suppressed by two powers of x, etc.

The equations developed in Refs. [52, 54, 57, 58, 60, 65] were also derived in the DLA. Similar to the unpolarized evolution equations [69–78], the helicity evolution equations [52, 54, 57, 58, 65] only take on a closed form in the large-N_c [93] and large-N_c&N_f [94] limits. In that case they become the evolution equations for the so-called "polarized dipole amplitudes," which are dipole scattering amplitudes with an insertion of one gluon or two quark operators at the sub-eikonal level into the light-cone Wilson lines [57, 58, 65, 86]. The earlier version of this evolution, constructed in Refs. [52, 54, 57] (which we will refer to as KPS) led to an intercept of $\alpha_h = \frac{4}{\sqrt{3}}\sqrt{\frac{\alpha_s N_c}{2\pi}} \approx 2.31\sqrt{\frac{\alpha_s N_c}{2\pi}}$ in the large-N_c limit [55, 56], significantly smaller than the intercept of $\alpha_h = 3.66\sqrt{\frac{\alpha_s N_c}{2\pi}}$ found by BER in the same limit. The KPS evolution has recently been augmented [65] by inclusion of the operators which couple what can be interpreted as the OAM of the gluon probe (in $A^- = 0$ light-cone gauge of the projectile) to the spin of the proton.[1] The revised evolution equations, which we will refer to as the KPS-CTT equations [52, 58, 65], have been solved at large N_c both numerically [65] and analytically [95]. While the former reference found the numerical value of the intercept to be $\alpha_h = 3.66\sqrt{\frac{\alpha_s N_c}{2\pi}}$, appearing to agree with BER, the analytic solution [95] found that the BER and KPS-CTT intercepts at large N_c disagree in the third decimal point. Very recently, a numerical solution of the large-N_c&N_f version of the KPS-CTT evolution [96] established a disagreement with BER (in the same limit) at the 2–3% level, with the discrepancy increasing with N_f. While the observed differences between the two sets of results appear to demand further theoretical investigation, they are sufficiently small to allow one to proceed with rigorous phenomenological applications of the KPS-CTT evolution equations [52, 54, 57, 58, 65].

The first phenomenological application of the polarized dipole amplitude formalism, more precisely its KPS version, was performed by a subset of the present authors in Ref. [97]. In that work a successful "proof-of-principle" fit of the world polarized DIS data for $x < 0.1$ and $Q^2 > m_c^2$ (with m_c the charm quark mass) based solely on small-x helicity evolution was performed. Since the analysis of Ref. [97] was limited to DIS data, only the g_1 structure functions of the proton and neutron were extracted instead of the individual flavor hPDFs. The impact of DIS data from the EIC on our ability to predict the g_1 structure function at small-x was also estimated. In addition, in order to demonstrate that it is possible to extract the combinations $\Delta q^+(x,Q^2) \equiv \Delta q(x,Q^2) + \Delta\bar{q}(x,Q^2)$ for $q = u, d, s$ using small-x helicity evolution, parity-violating DIS EIC pseudodata was utilized. We refer to $\Delta q^+(x,Q^2)$ as the flavor *singlet* hPDFs, whereas the flavor *nonsinglet* hPDFs are similarly defined as $\Delta q^-(x,Q^2) \equiv \Delta q(x,Q^2) - \Delta\bar{q}(x,Q^2)$.

C. Subject of this work

In the present paper we perform, for the first time, a phenomenological analysis based on the KPS-CTT version of small-x helicity evolution with several other significant new features beyond the work of Ref. [97]. Instead of the

[1] We thank Florian Cougoulic, Alex Kovner, and Feng Yuan for suggesting this interpretation of those operators.

large-N_c limit of evolution employed in Ref. [97], we base our analysis on the large-$N_c\&N_f$ limit. In addition to the polarized DIS data, we also include in our analysis polarized SIDIS data. Since the SIDIS data is sensitive to the individual quark and anti-quark helicity PDFs, $\Delta q(x,Q^2)$ and $\Delta\bar{q}(x,Q^2)$, it is not sufficient to just use the flavor singlet helicity evolution from Ref. [65], which only yields the $\Delta q^+(x,Q^2)$ combination (in addition to the gluon hPDF $\Delta G(x,Q^2)$). One also needs the flavor nonsinglet quark hPDFs $\Delta q^-(x,Q^2)$. Those are constructed using the large-N_c small-x helicity evolution equation for the flavor nonsinglet case from Ref. [54]. Finally, to make the calculation more realistic and avoid the integrals (2) diverging at $x\to 0$, we include running coupling corrections into the kernel of the evolution equations (both flavor singlet and nonsinglet). We make the coupling run with the daughter dipole size, which ends up effectively reducing the intercept α_h for the flavor singlet hPDFs below 1. (The intercept of the flavor nonsinglet hPDFs is smaller than 1 even at fixed coupling in the realistic $\alpha_s = 0.2-0.3$ range; still, for consistency, we apply running coupling corrections to the flavor nonsinglet helicity evolution as well.) The analysis of SIDIS data also requires input for fragmentation functions, which are not specific to the small-x evolution at hand; therefore, we employ the existing JAM fragmentation functions for pions, kaons, and unidentified hadrons from Ref. [34].

The paper is structured as follows. We begin in Sec. II by outlining the polarized dipole amplitude formalism developed in Refs. [52, 54, 57, 58, 65] and explicitly writing out the flavor-singlet KPS-CTT large $N_c\&N_f$ DLA small-x helicity evolution equations with running coupling corrections, along with the flavor nonsinglet helicity evolution equation derived in Ref. [54]. We also present the details of our numerical methodology in solving these evolution equations. We describe the calculation of observables (double-longitudinal spin asymmetries) in DIS and SIDIS, particularly detailing the calculation of the polarized SIDIS cross section at small x. We explain our analysis of the world polarized DIS and SIDIS low-x data and describe the implementation of the KPS-CTT evolution within the JAM Bayesian Monte Carlo framework. The results of our analysis are presented in Sec. III, which include plots of data versus theory, the hPDFs, and the g_1 structure function as well as an estimate of how much of the proton spin is carried by the spins of partons at small x. We also conduct an EIC impact study on the aforementioned quantities. Conclusions and an outlook are given in Sec. IV.

II. METHODOLOGY

A. Flavor singlet evolution at small x

The small-x helicity formalism in the light-cone operator treatment (LCOT) framework along with the large-$N_c\&N_f$ small-x evolution equations for helicity were revised in Ref. [65]. In the new formalism, the (DIS) g_1 structure function is given by

$$g_1(x,Q^2) = \frac{1}{2}\sum_q e_q^2\,\Delta q^+(x,Q^2)\,, \tag{4}$$

where e_q is the quark electric charge as a fraction of the magnitude of the electron's charge. The flavor singlet quark hPDFs in the DLA take the form [58, 65]

$$\Delta q^+(x,Q^2) \equiv \Delta q(x,Q^2) + \Delta\bar{q}(x,Q^2) = -\frac{N_c}{2\pi^3}\int\limits_{\Lambda^2/s}^{1}\frac{\mathrm{d}z}{z}\int\limits_{1/zs}^{\min\left[1/zQ^2,1/\Lambda^2\right]}\frac{\mathrm{d}x_{10}^2}{x_{10}^2}\left[Q_q(x_{10}^2,zs)+2\,G_2(x_{10}^2,zs)\right]. \tag{5}$$

The gluon hPDF in the DLA is [57]

$$\Delta G(x,Q^2) = \frac{2N_c}{\alpha_s\pi^2}\,G_2\!\left(x_{10}^2=\frac{1}{Q^2},zs=\frac{Q^2}{x}\right). \tag{6}$$

Note the (flavor singlet) quark and gluon hPDFs are expressed in terms of the impact-parameter-integrated polarized dipole amplitudes Q_q and G_2, whose operator definitions can be found in Refs. [52, 58, 65] and Ref. [57], respectively. The dipole amplitudes depend on the transverse size of the dipole $x_{10} = |\mathbf{x}_1-\mathbf{x}_0|$, where the "polarized" (sub-eikonally interacting) line is located at $\mathbf{x}_1$ and the unpolarized (standard) Wilson line is at $\mathbf{x}_0$ in the transverse plane. The amplitudes also depend on the center-of-mass energy squared s of the projectile–proton scattering. The dimensionless longitudinal momentum fraction z can be thought of as the momentum fraction of the softest of the two lines in the dipole. (However, this definition is somewhat imprecise, and it is more accurate to think of zs as the effective energy of the dipole–proton scattering [52, 54, 64].) The momentum scale Λ denotes our infrared (IR) cutoff and is the scale characterizing the proton. No dipole can be larger than $1/\Lambda$, that is, $x_{ij} < 1/\Lambda$.

At small x, Eq. (4) was derived in Refs. [52, 54, 55]. However, the contribution of G_2 to Δq^+ in Eq. (5) was recognized only recently [65]. Given that G_2 is closely related to the gluon hPDF ΔG, as follows from Eq. (6), Eqs. (4) and (5) show that in our LCOT approach the contribution of ΔG to g_1 comes in through Δq^+ [65, 96] (see more on this below). We have also expanded the definition of the amplitude Q_q to include dependence on the quark flavor $q = u, d, s$, such that we have three different amplitudes Q_u, Q_d and Q_s for the light flavors, which is necessary since the quark spinor field operators are flavor dependent. The operator definition for the three flavors is the same, but the flavor dependence can enter through the initial condition of the dipole amplitude evolution.

While Eq. (4) appears to correspond to the leading-order (LO) expression in the collinear factorization approach to polarized DIS (see, *e.g.*, Eq. (4.5) in Ref. [98]), in the LCOT framework it contains more information than that. In collinear factorization at the next-to-leading order (NLO) and beyond, the expression for the g_1 structure function also involves the contribution of ΔG. More precisely, one can write [18, 19, 99–108]

$$g_1(x,Q^2) = \frac{1}{2}\sum_q e_q^2 \left\{ \Delta q^+(x,Q^2) + \int\limits_x^1 \frac{\mathrm{d}z}{z} \left[\Delta c_q(z)\, \Delta q^+\Big(\frac{x}{z}, Q^2\Big) + \Delta c_G(z)\, \Delta G\Big(\frac{x}{z}, Q^2\Big)\right]\right\}, \tag{7}$$

with the coefficient functions $\Delta c_q(z)$ and $\Delta c_G(z)$ calculated order-by-order in perturbation theory. In the $\overline{\text{MS}}$ scheme, the small-x large-$N_c\&N_f$ coefficient functions are [99] (see also [108] for the three-loop contribution, which we do not show explicitly here)

$$\Delta c_q(z) = \frac{\alpha_s N_c}{4\pi}\, \ln\frac{1}{z} + \frac{5}{12}\left(\frac{\alpha_s N_c}{4\pi}\right)^2 \left[1 - 4\,\frac{N_f}{N_c}\right] \ln^3\frac{1}{z} + \mathcal{O}(\alpha_s^3)\,, \tag{8a}$$

$$\Delta c_G(z) = -\frac{\alpha_s}{2\pi}\, \ln\frac{1}{z} - \frac{11}{2}\left(\frac{\alpha_s}{4\pi}\right)^2 N_c\, \ln^3\frac{1}{z} + \mathcal{O}(\alpha_s^3)\,. \tag{8b}$$

Note that after the z-integration in Eq. (7), the contribution from the order-α_s terms in Eqs. (8) becomes of the order $\alpha_s\, \ln^2(1/x)$, the contribution from the order-α_s^2 terms in Eqs. (8) becomes of the order $[\alpha_s\, \ln^2(1/x)]^2$, etc. Consequently, in the collinear factorization power counting, the contributions from $\Delta c_q(z)$ and $\Delta c_G(z)$ in Eq. (7) are NLO and beyond, allowing one to truncate the expansion at a given order in α_s determined by the accuracy of the calculation. In our DLA small-x power counting, the leading small-x parts of $\Delta c_q(z)$ and $\Delta c_G(z)$ are already included to all orders in the powers of $\alpha_s\, \ln^2(1/x)$. This is precisely what Eq. (4) accomplishes [96]. While it appears to be just the LO part of Eq. (7), the fact that Δq^+ in it is evolved with the DLA small-x helicity evolution [52, 54, 57, 58, 65], resuming powers of both $\alpha_s\, \ln^2(1/x)$ and $\alpha_s\, \ln(1/x)\, \ln\big(Q^2/Q_0^2\big)$, implies that Eq. (4) contains both the DLA DGLAP evolution of Δq^+, which mixes it with ΔG (by resumming the powers of $\alpha_s\, \ln(1/x)\, \ln\big(Q^2/Q_0^2\big)$), and the leading small-x parts of the coefficient functions $\Delta c_q(z)$ and $\Delta c_G(z)$, resummed to all orders in $\alpha_s\, \ln^2(1/x)$, bringing in the ΔG and additional Δq^+ contributions into g_1, as expected from Eq. (7) (see [96] for a more detailed discussion). The fact that all these contributions are contained in Eq. (4), which looks much simpler than Eq. (7), appears to suggest that we are working in the "polarized DIS scheme" [96] for our hPDFs (cf. [109] for the standard DIS scheme), where ΔG does not contribute to g_1 directly, unlike the more widely used $\overline{\text{MS}}$ scheme from Eq. (7). Other small-x calculations, such as the NLO BFKL evolution [110, 111] (in the small-x power counting), result in the spin-independent GG anomalous dimension in the DIS scheme [102]. This appears to be similar to our calculation giving a polarized DIS scheme result, with the difference between the anomalous dimensions in different schemes being proportional to N_f [96, 102].

The polarized dipole amplitudes Q_q and G_2, which enter Eqs. (4), (5) and (6), are found by solving the small-x evolution equations. The DLA large-$N_c\&N_f$ revised evolution equations at fixed coupling are given by Eqs. (155) in Ref. [65] (see also Refs. [52, 58]). The existing numerical solution [96] of Eqs. (155) from Ref. [65] (with fixed coupling) leads to a large intercept α_h for the flavor singlet hPDFs (see Eq. (3) with the intercept values in the text following that equation), making the integrals in Eq. (2) divergent as $x \to 0$. As we discussed above, this divergence may be regulated by higher-order corrections and/or by the onset of saturation, which is likely to slow down the growth of hPDFs as $x \to 0$. As the unpolarized small-x evolution [66–78] is single-logarithmic, resumming powers of $\alpha_s\, \ln(1/x)$, a consistent inclusion of saturation effects is beyond the double-logarithmic approximation employed here. While, strictly-speaking, phenomenology based on small-x evolution in the DLA should work with the high intercepts found in Ref. [96], it appears unphysical to perform an analysis of experimental data with a formalism that would yield an infinite amount of spin at small x. While we cannot include the single-logarithmic (resumming powers of $\alpha_s\, \ln(1/x)$) corrections to the revised DLA evolution equations (155) from Ref. [65], since they have not been fully calculated yet (see Ref. [64] for the single-logarithmic corrections to the earlier KPS evolution), we can include running-coupling corrections into the DLA evolution. A similar approximation was employed in the BER framework [112, 113] and for the spin-independent eikonal small-x evolution [114, 115], resulting in successful phenomenology.

In the DLA equations (155) from Ref. [65] the scale of the coupling could be given by either the "parent" (x_{10}) or the "daughter" (x_{21} or x_{32}) dipole. The running coupling corrections to the (un-revised) KPS evolution, calculated in

Ref. [64] (along with other single-logarithmic corrections), indicate that at DLA the coupling runs with the daughter dipole size. For the neighbor dipole amplitudes $\overline{\Gamma},\widetilde{\Gamma}$, and Γ_2, introduced in Refs. [52, 54, 57, 58, 60, 65] and also entering helicity evolution equations, the coupling runs with the dipole size x_{32}, which determines the next emission's lifetime and is integrated over in the kernel [64]. Therefore, we proceeded by running the coupling with the daughter dipole size (or, more precisely, with the dipole size that we integrate over in the kernel) in all the terms of the KPS-CTT evolution. (See Refs. [116–120] for calculations and analyses of the running coupling corrections in the unpolarized small-x evolution case.) The resulting running-coupling version of the large-N_c&N_f helicity evolution equations (155) from [65] reads

$$\begin{aligned}
Q_q(x_{10}^2,zs) = Q_q^{(0)}(x_{10}^2,zs) &+ \frac{N_c}{2\pi}\int_{1/x_{10}^2 s}^{z}\frac{\mathrm{d}z'}{z'}\int_{1/z's}^{x_{10}^2}\frac{\mathrm{d}x_{21}^2}{x_{21}^2}\,\alpha_s\!\left(\frac{1}{x_{21}^2}\right)\Big[2\,\widetilde{G}(x_{21}^2,z's) + 2\,\widetilde{\Gamma}(x_{10}^2,x_{21}^2,z's) \\
&+ Q_q(x_{21}^2,z's) - \overline{\Gamma}_q(x_{10}^2,x_{21}^2,z's) + 2\,\Gamma_2(x_{10}^2,x_{21}^2,z's) + 2\,G_2(x_{21}^2,z's)\Big] \\
&+ \frac{N_c}{4\pi}\int_{\Lambda^2/s}^{z}\frac{\mathrm{d}z'}{z'}\int_{1/z's}^{\min\left[x_{10}^2 z/z',1/\Lambda^2\right]}\frac{\mathrm{d}x_{21}^2}{x_{21}^2}\,\alpha_s\!\left(\frac{1}{x_{21}^2}\right)\Big[Q_q(x_{21}^2,z's) + 2\,G_2(x_{21}^2,z's)\Big]\,,
\end{aligned} \tag{9a}$$

$$\begin{aligned}
\overline{\Gamma}_q(x_{10}^2,x_{21}^2,z's) = Q_q^{(0)}(x_{10}^2,z's) &+ \frac{N_c}{2\pi}\int_{1/x_{10}^2 s}^{z'}\frac{\mathrm{d}z''}{z''}\int_{1/z''s}^{\min[x_{10}^2,x_{21}^2 z'/z'']}\frac{\mathrm{d}x_{32}^2}{x_{32}^2}\,\alpha_s\!\left(\frac{1}{x_{32}^2}\right)\Big[2\,\widetilde{G}(x_{32}^2,z''s) \\
&+ 2\,\widetilde{\Gamma}(x_{10}^2,x_{32}^2,z''s) + Q_q(x_{32}^2,z''s) - \overline{\Gamma}_q(x_{10}^2,x_{32}^2,z''s) + 2\,\Gamma_2(x_{10}^2,x_{32}^2,z''s) + 2\,G_2(x_{32}^2,z''s)\Big] \\
&+ \frac{N_c}{4\pi}\int_{\Lambda^2/s}^{z'}\frac{\mathrm{d}z''}{z''}\int_{1/z''s}^{\min\left[x_{21}^2 z'/z'',1/\Lambda^2\right]}\frac{\mathrm{d}x_{32}^2}{x_{32}^2}\,\alpha_s\!\left(\frac{1}{x_{32}^2}\right)\Big[Q_q(x_{32}^2,z''s) + 2\,G_2(x_{32}^2,z''s)\Big]\,,
\end{aligned} \tag{9b}$$

$$\begin{aligned}
\widetilde{G}(x_{10}^2,zs) = \widetilde{G}^{(0)}(x_{10}^2,zs) &+ \frac{N_c}{2\pi}\int_{1/x_{10}^2 s}^{z}\frac{\mathrm{d}z'}{z'}\int_{1/z's}^{x_{10}^2}\frac{\mathrm{d}x_{21}^2}{x_{21}^2}\,\alpha_s\!\left(\frac{1}{x_{21}^2}\right)\Big[3\,\widetilde{G}(x_{21}^2,z's) + \widetilde{\Gamma}(x_{10}^2,x_{21}^2,z's) \\
&+ 2\,G_2(x_{21}^2,z's) + \left(2-\frac{N_f}{2N_c}\right)\Gamma_2(x_{10}^2,x_{21}^2,z's) - \frac{1}{4N_c}\sum_q\overline{\Gamma}_q(x_{10}^2,x_{21}^2,z's)\Big] \\
&- \frac{1}{8\pi}\int_{\Lambda^2/s}^{z}\frac{\mathrm{d}z'}{z'}\int_{\max[x_{10}^2,\,1/z's]}^{\min\left[x_{10}^2 z/z',1/\Lambda^2\right]}\frac{\mathrm{d}x_{21}^2}{x_{21}^2}\,\alpha_s\!\left(\frac{1}{x_{21}^2}\right)\left[\sum_q Q_q(x_{21}^2,z's) + 2\,N_f\,G_2(x_{21}^2,z's)\right],
\end{aligned} \tag{9c}$$

$$\begin{aligned}
\widetilde{\Gamma}(x_{10}^2,x_{21}^2,z's) = \widetilde{G}^{(0)}(x_{10}^2,z's) &+ \frac{N_c}{2\pi}\int_{1/x_{10}^2 s}^{z'}\frac{\mathrm{d}z''}{z''}\int_{1/z''s}^{\min[x_{10}^2,x_{21}^2 z'/z'']}\frac{\mathrm{d}x_{32}^2}{x_{32}^2}\,\alpha_s\!\left(\frac{1}{x_{32}^2}\right)\Big[3\,\widetilde{G}(x_{32}^2,z''s) \\
&+ \widetilde{\Gamma}(x_{10}^2,x_{32}^2,z''s) + 2\,G_2(x_{32}^2,z''s) + \left(2-\frac{N_f}{2N_c}\right)\Gamma_2(x_{10}^2,x_{32}^2,z''s) - \frac{1}{4N_c}\sum_q\overline{\Gamma}_q(x_{10}^2,x_{32}^2,z''s)\Big] \\
&- \frac{1}{8\pi}\int_{\Lambda^2/s}^{z'x_{21}^2/x_{10}^2}\frac{\mathrm{d}z''}{z''}\int_{\max[x_{10}^2,\,1/z''s]}^{\min\left[x_{21}^2 z'/z'',1/\Lambda^2\right]}\frac{\mathrm{d}x_{32}^2}{x_{32}^2}\,\alpha_s\!\left(\frac{1}{x_{32}^2}\right)\left[\sum_q Q_q(x_{32}^2,z''s) + 2\,N_f\,G_2(x_{32}^2,z''s)\right],
\end{aligned} \tag{9d}$$

$$G_2(x_{10}^2,zs) = G_2^{(0)}(x_{10}^2,zs) + \frac{N_c}{\pi}\int\limits_{\Lambda^2/s}^{z}\frac{\mathrm{d}z'}{z'}\int\limits_{\max\left[x_{10}^2,\frac{1}{z's}\right]}^{\min\left[\frac{z}{z'}x_{10}^2,\frac{1}{\Lambda^2}\right]}\frac{\mathrm{d}x_{21}^2}{x_{21}^2}\,\alpha_s\!\left(\frac{1}{x_{21}^2}\right)\Big[\widetilde{G}(x_{21}^2,z's) + 2\,G_2(x_{21}^2,z's)\Big]\,, \tag{9e}$$

$$\Gamma_2(x_{10}^2,x_{21}^2,z's) = G_2^{(0)}(x_{10}^2,z's) + \frac{N_c}{\pi}\int\limits_{\Lambda^2/s}^{z'\frac{x_{21}^2}{x_{10}^2}}\frac{\mathrm{d}z''}{z''}\int\limits_{\max\left[x_{10}^2,\frac{1}{z''s}\right]}^{\min\left[\frac{z'}{z''}x_{21}^2,\frac{1}{\Lambda^2}\right]}\frac{\mathrm{d}x_{32}^2}{x_{32}^2}\,\alpha_s\!\left(\frac{1}{x_{32}^2}\right)\Big[\widetilde{G}(x_{32}^2,z''s) + 2\,G_2(x_{32}^2,z''s)\Big]\,. \tag{9f}$$

The running coupling in Eqs. (9) is given by the standard one-loop expression,

$$\alpha_s(Q^2) = \frac{12\pi}{11N_c - 2N_f}\frac{1}{\ln\Big(Q^2/\Lambda^2_{\rm QCD}\Big)}, \tag{10}$$

with $\Lambda_{\rm QCD}$ the QCD confinement scale. We have also modified Eqs. (9) compared to Eqs. (155) in Ref. [65] in two additional ways: first, we are now treating the momentum scale Λ as the infrared cutoff (assuming that $\Lambda > \Lambda_{\rm QCD}$); second, since the amplitude Q_q is now flavor dependent, we replaced the N_f factors from Ref. [65] by flavor sums $\Big(\sum_q\Big)$. Eqs. (9) also include the dipole amplitude $\widetilde{G}$, which is defined in Ref. [65]: as one can see from Eqs. (4), (5) and (6), the g_1 structure function and hPDFs do not depend on this dipole amplitude: this will affect our analysis below. Following Refs. [52, 54, 57, 58, 60, 65] we have introduced the impact-parameter integrated "neighbor dipole amplitudes" $\overline{\Gamma}_q(x_{10}^2, x_{32}^2, zs)$, $\widetilde{\Gamma}(x_{10}^2, x_{32}^2, zs)$ and $\Gamma_2(x_{10}^2, x_{32}^2, zs)$ for the amplitudes Q_q, $\widetilde{G}$ and G_2, respectively, with physical dipole transverse size x_{10} and lifetime $\sim x_{32}^2 z$. This lifetime for the neighbor dipole amplitudes depends on the transverse size of another (adjacent) dipole, giving rise to the "neighbor" amplitude name.

The inhomogeneous terms (initial conditions) in Eqs. (9) can be calculated at the Born level for a longitudinally polarized massless quark target instead of the proton. This gives [52, 54, 57, 65]

$$\widetilde{G}^{(0)}(x_{10}^2, zs) = Q_q^{(0)}(x_{10}^2, zs) = \frac{\alpha_s^2 C_F}{2N_c}\pi\Big[C_F \ln\frac{zs}{\Lambda^2} - 2\ln\left(zsx_{10}^2\right)\Big], \qquad G_2^{(0)}(x_{10}^2, zs) = \frac{\alpha_s^2 C_F}{N_c}\pi \ln\frac{1}{x_{10}\Lambda}, \tag{11}$$

where $C_F = (N_c^2-1)/(2N_c)$ is the Casimir operator in the fundamental representation of SU(N_c). These expressions will motivate our choice of the initial conditions for our phenomenological analysis. (While strictly-speaking we should have included running coupling corrections into the expressions (11) as well, the fixed-coupling form has a sufficient variety of dependence on the relevant variables zs and x_{10} to motivate a fairly broad class of initial conditions we will implement below.)

B. Flavor nonsinglet evolution at small x

As one can see from Eq. (4) in the previous subsection, measurements of the g_1 structure function in DIS off a nucleon are only sensitive to a specific linear combination of $\Delta q^+(x, Q^2)$. Such DIS measurements were the topic of our previous study [97]. However, the polarized SIDIS process, as we will see below, provides information on the individual flavor hPDFs $\Delta q(x, Q^2)$, or, equivalently, on both $\Delta q^+(x, Q^2)$ and $\Delta q^-(x, Q^2) \equiv \Delta q(x, Q^2) - \Delta\bar{q}(x, Q^2)$. The above evolution equations (9) only allow us to calculate $\Delta q^+(x, Q^2)$. To perform the polarized SIDIS data analysis we need to supplement them with the small-x helicity evolution in the flavor nonsinglet channel.

A closed evolution equation at small x yielding $\Delta q^-(x, Q^2)$ in the LCOT framework can be obtained in the large-N_c limit, which is equivalent to the large-N_c&N_f limit for the flavor nonsinglet helicity evolution in DLA. (In the DLA, the flavor nonsinglet evolution is N_f-independent, since virtual quark bubbles do not contribute. Thus, the large-N_c and large-N_c&N_f limits are identical for flavor nonsinglet evolution.) Employing Eq. (54b) of [54] we write in the DLA

$$\Delta q^-(x, Q^2) \equiv \Delta q(x, Q^2) - \Delta\bar{q}(x, Q^2) = \frac{N_c}{2\pi^3}\int\limits_{\Lambda^2/s}^{1}\frac{{\rm d}z}{z}\int\limits_{1/zs}^{\min\left[1/zQ^2, 1/\Lambda^2\right]}\frac{{\rm d}x_{10}^2}{x_{10}^2}\, G_q^{\rm NS}(x_{10}^2, zs)\,. \tag{12}$$

We see that $\Delta q^-(x, Q^2)$ only depends on one (impact-parameter integrated) polarized dipole amplitude, $G_q^{\rm NS}(x_{10}^2, zs)$, for each flavor $q = u, d, s$. The definition of this dipole amplitude can be found in Eqs. (55) of Ref. [54]. Just as in the flavor singlet case, the nonsinglet dipole amplitude can be determined by solving the small-x evolution equation, which reads [54]

$$G_q^{\rm NS}(x_{10}^2, z) = G_q^{{\rm NS}\,(0)}(x_{10}^2, z) + \frac{N_c}{4\pi}\int\limits_{\Lambda^2/s}^{z}\frac{{\rm d}z'}{z'}\int\limits_{1/z's}^{\min\left[x_{10}^2 z/z', 1/\Lambda^2\right]}\frac{{\rm d}x_{21}^2}{x_{21}^2}\,\alpha_s\Big(\frac{1}{x_{21}^2}\Big)\, G_q^{\rm NS}(x_{21}^2, z'). \tag{13}$$

To be consistent with the flavor-singlet evolution, we have also inserted a running coupling into Eq. (13), modifying it slightly compared to the fixed-coupling flavor nonsinglet evolution equation derived in Ref. [54]. The inhomogeneous

term in Eq. (13) can also be calculated at Born level for a quark target [54]:

$$G_q^{\mathrm{NS}\,(0)}(x_{10}^2, zs) = \frac{\alpha_s^2 C_F^2}{N_c}\pi \ln\frac{zs}{\Lambda^2}. \tag{14}$$

This expression will again motivate our choice of the flavor nonsinglet initial conditions in phenomenology.

C. Numerical implementation of the flavor singlet and nonsinglet evolution

Similar to our previous works [55, 61, 65, 96], small-x helicity evolution equations simplify if one performs the following change of variables,

$$\eta^{(n)} = \sqrt{\frac{N_c}{2\pi}}\ln\frac{z^{(n)}s}{\Lambda^2}, \qquad s_{ij} = \sqrt{\frac{N_c}{2\pi}}\ln\frac{1}{x_{ij}^2\Lambda^2}. \tag{15}$$

Here $z^{(n)} = z, z', z'', \ldots$, while $\eta^{(n)} = \eta, \eta', \eta'', \ldots$. Note that this form, in contrast to the earlier works, removes the factor $\sqrt{\alpha_s}$ from the definition of the variables η and s_{ij}, so that the one-loop running of the coupling can be implemented via (cf. Eq. (10))

$$\alpha_s(s_{21}) = \sqrt{\frac{N_c}{2\pi}}\frac{12\pi}{(11N_c - 2N_f)}\frac{1}{(s_{21}+s_0)}, \qquad s_0 = \sqrt{\frac{N_c}{2\pi}}\ln\frac{\Lambda^2}{\Lambda_{\mathrm{QCD}}^2}. \tag{16}$$

Since we assume that $\Lambda > \Lambda_{\mathrm{QCD}}$, we have $s_0 > 0$. As all our dipole sizes are smaller than $1/\Lambda$, we see that $s_{21} > 0$, thus avoiding the Landau pole at $s_{21} = -s_0 < 0$ in the coupling. (In general, having an IR cutoff for the dipole sizes, $x_{ij} < 1/\Lambda$, implies that all $s_{ij} > 0$.)

Before discretizing our evolution equations, we need to impose the starting value of x for our evolution (cf. Ref. [97]). For $z = 1$ and $x_{10} = 1/Q$, we have the "rapidity" variable $y \equiv \eta - s_{10} = \sqrt{\frac{N_c}{2\pi}}\ln\frac{1}{x}$. Hence, if our evolution starts at some value of x labeled by x_0, then the $x < x_0$ condition implies that $\eta - s_{10} > \sqrt{\frac{N_c}{2\pi}}\ln\frac{1}{x_0} \equiv y_0$. Regarding the value of x_0, it was observed in Ref. [97], using the older (KPS) version of our helicity evolution, that good-χ^2 fits of the polarized DIS data can be obtained with $x_0 = 0.1$ (and even for a slightly higher values of x_0). This is in contrast to the $x_0 = 0.01$ starting point of the evolution [69–78] for phenomenological analyses of the unpolarized observables (see, *e.g.*, Refs. [114, 115]). As discussed in Sec. III A below, it was speculated in Ref. [97] that such a discrepancy could be attributed to the helicity evolution resumming the double-logarithmic parameter $\alpha_s \ln^2(1/x)$ while the unpolarized evolution [71–78, 121, 122] resums single logarithms $\alpha_s \ln(1/x)$. This way, the resummation parameter for helicity evolution is larger at small x, making the helicity evolution start at larger x values. We thus put $x_0 = 0.1$ in all our analyses below.[2]

The full process of discretizing our flavor singlet and nonsinglet evolution equations with running coupling is detailed in Appendix A. In the end, the discretized version of Eqs. (9) written in terms of the variables (15) reads

$$\begin{aligned} Q_q[i,j] = {} & Q_q[i,j-1] + Q_q^{(0)}[i,j] - Q_q^{(0)}[i,j-1] \\ & + \Delta^2 \sum_{i'=i}^{j-2-y_0} \alpha_s[i']\Big[\frac{3}{2}Q_q[i',j-1] + 2\widetilde{G}[i',j-1] + 2\widetilde{\Gamma}[i,i',j-1] \\ & - \overline{\Gamma}_q[i,i',j-1] + 3G_2[i',j-1] + 2\Gamma_2[i,i',j-1]\Big] \\ & + \frac{1}{2}\Delta^2 \sum_{j'=j-1-i}^{j-2} \alpha_s[i+j'-j+1]\Big[Q_q[i+j'-j+1,j'] + 2G_2[i+j'-j+1,j']\Big], \end{aligned} \tag{17a}$$

$$\overline{\Gamma}_q[i,k,j] = \overline{\Gamma}_q[i,k-1,j-1] + Q_q^{(0)}[i,j] - Q_q^{(0)}[i,j-1] \tag{17b}$$

[2] Note that the $x < x_0$ condition is applied only to our small-x helicity evolution equations. The expressions for the g_1 structure function (4) and the quark (5) and gluon (6) hPDFs remain as shown above: for $x > x_0$ they are driven by the initial conditions/inhomogeneous terms for our evolution (cf. Ref. [97]). The coupling in Eq. (6) runs with Q^2.

$$+\Delta^2\sum_{i'=k-1}^{j-2-y_0}\alpha_s[i']\Big[\frac{3}{2}Q_q[i',j-1]+2\widetilde{G}[i',j-1]+2\widetilde{\Gamma}[i,i',j-1]$$
$$-\overline{\Gamma}_q[i,i',j-1]+3G_2[i',j-1]+2\Gamma_2[i,i',j-1]\Big]\,,$$

$$\widetilde{G}[i,j]=\widetilde{G}[i,j-1]+\widetilde{G}^{(0)}[i,j]-\widetilde{G}^{(0)}[i,j-1] \tag{17c}$$
$$+\Delta^2\sum_{i'=i}^{j-2-y_0}\alpha_s[i']\Big[3\widetilde{G}[i',j-1]+\widetilde{\Gamma}[i,i',j-1]$$
$$+2G_2[i',j-1]+\big(2-\frac{N_f}{2N_c}\big)\Gamma_2[i,i',j-1]-\frac{1}{4N_c}\sum_q\overline{\Gamma}_q[i,i',j-1]\Big]$$
$$-\Delta^2\frac{1}{4N_c}\sum_{j'=j-1-i}^{j-2}\alpha_s[i+j'-j+1]\Big[\sum_q Q_q[i+j'-j+1,j']+2N_fG_2[i+j'-j+1,j']\Big]\,,$$

$$\widetilde{\Gamma}[i,k,j]=\widetilde{\Gamma}[i,k-1,j-1]+\widetilde{G}^{(0)}[i,j]-\widetilde{G}^{(0)}[i,j-1] \tag{17d}$$
$$+\Delta^2\sum_{i'=k-1}^{j-2-y_0}\alpha_s[i']\Big[3\widetilde{G}[i',j-1]+\widetilde{\Gamma}[i,i',j-1]$$
$$+2G_2[i',j-1]+\big(2-\frac{N_f}{2N_c}\big)\Gamma_2[i,i',j-1]-\frac{1}{4N_c}\sum_q\overline{\Gamma}_q[i,i',j-1]\Big]\,,$$

$$G_2[i,j]=G_2[i,j-1]+G_2^{(0)}[i,j]-G_2^{(0)}[i,j-1] \tag{17e}$$
$$+2\Delta^2\sum_{j'=j-1-i}^{j-2}\alpha_s[i+j'-j+1]\Big[\widetilde{G}[i+j'-j+1,j']+2G_2[i+j'-j+1,j']\Big]\,,$$

$$\Gamma_2[i,k,j]=\Gamma_2[i,k-1,j-1]+G_2^{(0)}[i,j]-G_2^{(0)}[i,j-1]\,, \tag{17f}$$

where the numerical step sizes are chosen such that $\Delta\eta=\Delta s_{10}=\Delta s_{21}\equiv\Delta$, and the indices are defined by $\{\eta,s_{10},s_{21}\}\to\{i,j,k\}\cdot\Delta$. Eqs. (17) allow us to compute the numerical solution for the flavor singlet evolution equations (9). Note that it is only necessary to loop over the ranges dictated by our physical assumptions, $0\le i\le k\le j\le j_{max}$ and $i<j$. Furthermore, it is useful to notice that the neighbor dipole amplitudes reduce to their dipole-amplitude counterparts when $k=i$, that is,

$$\overline{\Gamma}_q[i,k=i,j]=Q_q[i,j]\,, \tag{18a}$$
$$\widetilde{\Gamma}[i,k=i,j]=\widetilde{G}[i,j]\,, \tag{18b}$$
$$\Gamma_2[i,k=i,j]=G_2[i,j]\,. \tag{18c}$$

We can continue this convention and write the quark and gluon hPDFs from Eqs. (5) and (6) in the new variables,

$$\Delta q^+(x,Q^2)=-\frac{1}{\pi^2}\int_0^{\sqrt{\frac{N_c}{2\pi}}\ln\frac{Q^2}{x\,\Lambda^2}}\mathrm{d}\eta\int_{\max\left[0,\eta-\sqrt{\frac{N_c}{2\pi}}\ln\frac{1}{x}\right]}^{\eta}\mathrm{d}s_{10}\;\left[Q_q(s_{10},\eta)+2\,G_2(s_{10},\eta)\right]\,, \tag{19}$$

and

$$\Delta G(x,Q^2)=\frac{2N_c}{\alpha_s(Q^2)\,\pi^2}\,G_2\left(s_{10}=\sqrt{\frac{N_c}{2\pi}}\ln\frac{Q^2}{\Lambda^2},\,\eta=\sqrt{\frac{N_c}{2\pi}}\,\ln\frac{Q^2}{x\Lambda^2}\right)\,, \tag{20}$$

where the only difference compared to ΔG from Eq. (6) is the running coupling.

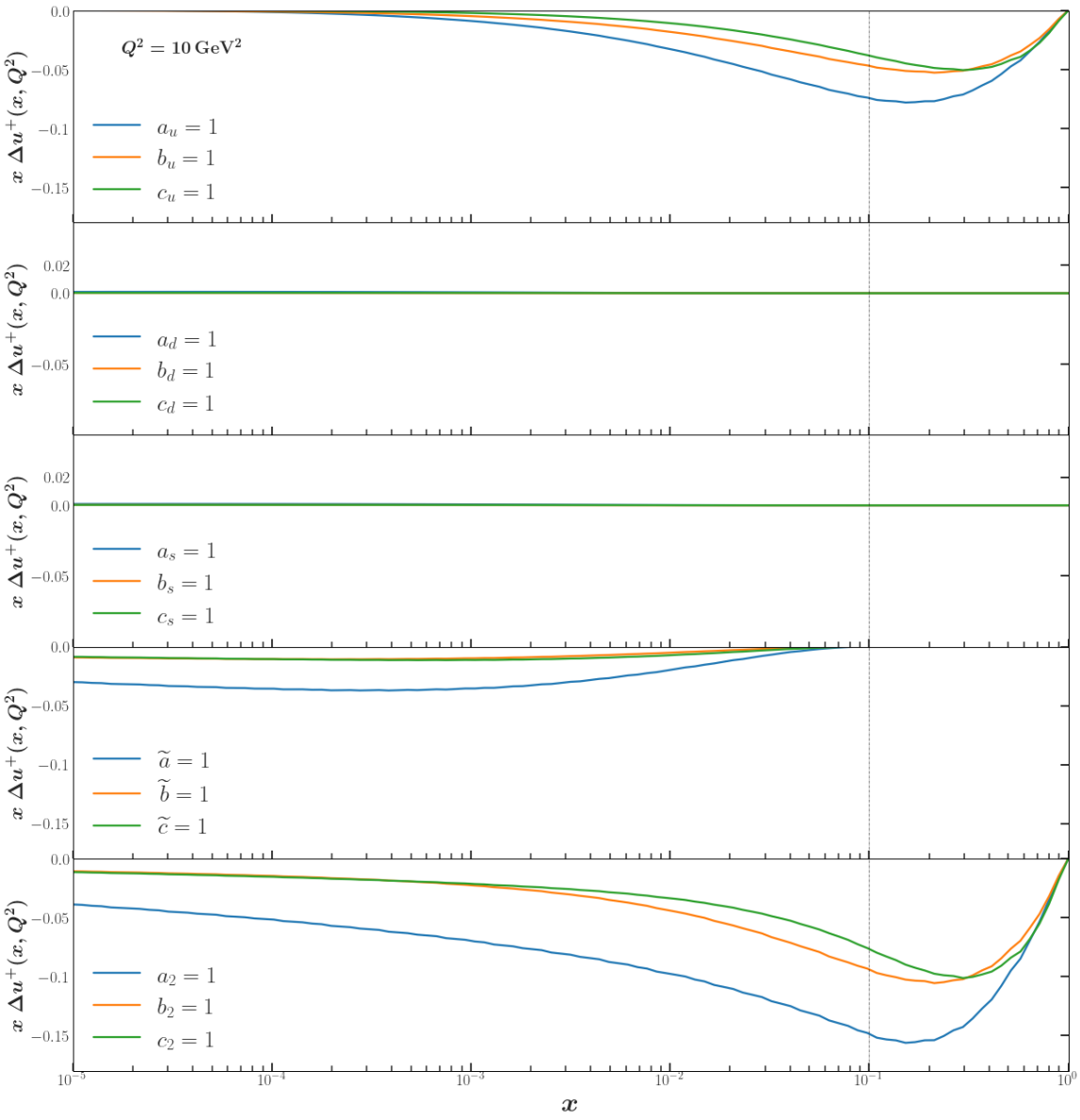

FIG. 1. The u-quark hPDF, $x\Delta u^+(x)$, constructed solely out of each basis function in the range $x \in [10^{-5}, 1]$. The legend in each panel shows which basis function was used for which curve. For example, the blue curve in the top panel corresponds to $x\Delta u^+(x)$ constructed from the initial conditions $Q_u^{(0)} = \eta$ and $Q_q^{(0)} = \widetilde{G}^{(0)} = G_2^{(0)} = 0$ for $q \in \{d, s\}$. The evolution begins at $x_0 = 0.1$, and the coupling constant runs with the daughter-dipole prescription specified in Eqs. (A1).

The last pieces to consider are the inhomogeneous terms. According to the Born-level initial conditions (11), they can be re-written using our new logarithmic variables as

$$Q_q^{(0)}(s_{10}, \eta) = \widetilde{G}^{(0)}(s_{10}, \eta) = \frac{\alpha_s^2 C_F \pi}{2N_c}\sqrt{\frac{2\pi}{N_c}}\Big[(C_F - 2)\eta + 2s_{10}\Big], \tag{21a}$$

$$G_2^{(0)}(s_{10}, \eta) = \frac{\alpha_s^2 C_F \pi}{2N_c}\sqrt{\frac{2\pi}{N_c}}\, s_{10}\,. \tag{21b}$$

Since Eqs. (21) are linear in η and s_{10}, we follow Ref. [97] and employ the linear-expansion ansatz, *i.e.*,

$$Q_q^{(0)}(s_{10}, \eta) = a_q\,\eta + b_q\,s_{10} + c_q\,, \tag{22a}$$

$$\widetilde{G}^{(0)}(s_{10}, \eta) = \widetilde{a}\,\eta + \widetilde{b}\,s_{10} + \widetilde{c}\,, \tag{22b}$$

$$G_2^{(0)}(s_{10},\eta) = a_2\,\eta + b_2\,s_{10} + c_2\,. \tag{22c}$$

Thus, for the three light flavors we consider, $q = u, d, s$, the full set of initial conditions for the flavor singlet evolution depends on 15 parameters $a_u, b_u, c_u, a_d, \ldots, c_2$ which we will fit to the data. Moreover, because the evolution equations we are solving are linear, their solution can be written as a linear combination of 15 "basis" dipole amplitudes, each of which is constructed by performing the iterative calculation outlined above while setting one parameter (from all the a's, b's and c's) in Eqs. (22) to be 1 and all the other parameters to 0. Furthermore, since all hPDFs and the g_1 structure function depend linearly on the polarized dipole amplitudes, they are also linear combinations of their corresponding basis functions as well.

For example, $\Delta u^+(x)$ can be expressed as a linear combination of the 15 "basis hPDFs" shown in Fig. 1. Since $\Delta u^+(x)$ depends directly on the linear combination $Q_u + 2G_2$ (see Eq. (5)), one may expect that Q_u and G_2 have the largest contributions to $\Delta u^+(x)$ at moderate x. This is indeed the case, with the top and bottom panels in Fig. 1 having the largest-magnitude contributions to $\Delta u^+(x)$. Some of the other amplitudes contribute more significantly at lower x's, as their magnitudes begin to influence those of Q_u and/or G_2 through evolution. At the smallest values of x in Fig. 1, the largest contributor is G_2, followed by $\widetilde{G}$, while the contributions from Q_d and Q_s remain small for all values of x.

A consequence of this observation, that we will return to later, is that the sign of the g_1 structure function is influenced mainly by the sign of G_2 (or, equivalently, the sign of ΔG) and the sign of $\widetilde{G}$. A challenge for phenomenology presents itself: $\widetilde{G}$ is slow to grow and hence less sensitive to available data near $x = x_0$, but it has a potentially large effect on the small-x asymptotics. Unless we have sufficient data from an observable that is directly sensitive to $\widetilde{G}$, constraining that amplitude will be difficult.

Similar to the singlet evolution, the discretization of the nonsinglet evolution equation (13) reads (again, see Appendix A for details)

$$\begin{aligned} G^{\rm NS}[i,j] &= G^{\rm NS}[i,j-1] + G^{\rm NS\,(0)}[i,j] - G^{\rm NS\,(0)}[i,j-1] \\ &\quad + \frac{1}{2}\Delta^2\left[\sum_{i'=i}^{j-2-y_0} \alpha_s[i']\,G^{\rm NS}[i',j-1] + \sum_{j'=j-1-i}^{j-2} \alpha_s[i-j+1+j']\,G^{\rm NS}[i-j+1+j',j']\right]. \end{aligned} \tag{23}$$

The corresponding flavor nonsinglet quark hPDF is given by

$$\Delta q^-(x,Q^2) = -\frac{1}{\pi^2}\int_0^{\sqrt{\frac{N_c}{2\pi}}\ln\frac{Q^2}{x\,\Lambda^2}} {\rm d}\eta \int_{\max\left[0,\eta-\sqrt{\frac{N_c}{2\pi}}\ln\frac{1}{x}\right]}^{\eta} {\rm d}s_{10}\,G^{\rm NS}(s_{10},\eta)\,, \tag{24}$$

with the integrals also discretized and evaluated numerically.

The Born-level approximation (14) is linear in the logarithmic variables (15), so we make a linear expansion ansatz for the inhomogeneous term in the flavor nonsinglet evolution,

$$G_q^{\rm NS\,(0)} = a_q^{\rm NS}\,\eta + b_q^{\rm NS}\,s_{10} + c_q^{\rm NS}, \tag{25}$$

for each of the three light flavors, $q = u, d, s$. This means that flavor nonsinglet hPDFs can be reconstructed as a linear combination of 9 flavor nonsinglet basis functions, generated by putting one of the 9 parameters $(a_u^{\rm NS}, b_u^{\rm NS}, \ldots, c_s^{\rm NS})$ to 1, while setting all others equal to 0. Combining this with the 15 parameters from Eqs. (22) describing the inhomogeneous terms for the flavor singlet dipole amplitudes, we have 24 parameters (and associated basis functions) for the eight amplitudes $(Q_u, Q_d, Q_s, \widetilde{G}, G_2, G_u^{\rm NS}, G_d^{\rm NS}$ and $G_s^{\rm NS})$, which we will fit to describe the world polarized DIS and SIDIS experimental data at low x.

D. SIDIS cross section at small x

We will now derive a formula for the SIDIS structure function $g_1^h(x,z)$ at small x. Using the notation of Ref. [65], we start with the DIS structure function $g_1(x)$ and write it as

$$g_1(x,Q^2) = -\frac{Q^2}{16\pi^2\alpha_{\rm em}\,x}\sum_{\lambda=\pm}\lambda\,\sigma^{\vec{\gamma}^*+\vec{p}\to X}(\lambda,+)\,, \tag{26}$$

where $\sigma^{\vec{\gamma}^*+\vec{p}\to X}(\lambda,\Sigma)$ is the total virtual photon–proton cross section for the proton with helicity Σ and for the transversely polarized virtual photon with polarization λ, and $\alpha_{\rm em}$ is the fine structure constant. The virtual photon–proton cross section is always inelastic at this order in $\alpha_{\rm em}$, as the virtual photon has to decay into a quark–anti-quark pair, with the quark and anti-quark fragmenting into hadrons in the final state.

Consider producing a hadron with a fixed value of $z \equiv P\cdot P_h/P\cdot q$, where P and q are the 4-momenta of the proton and virtual photon, respectively, while P_h is the momentum of the detected hadron, as shown in Fig. 2. At high energy/small x we can work in the frame where the proton has a large P^+ momentum component, while the virtual photon has a large q^- momentum component. Then $z \approx P_h^-/q^-$ is the fraction of the virtual photon's minus momentum carried by the produced hadron. All other components of the hadron's momentum are integrated over. We then write, by analogy to Eq. (26), in the collinear approximation [123–125]

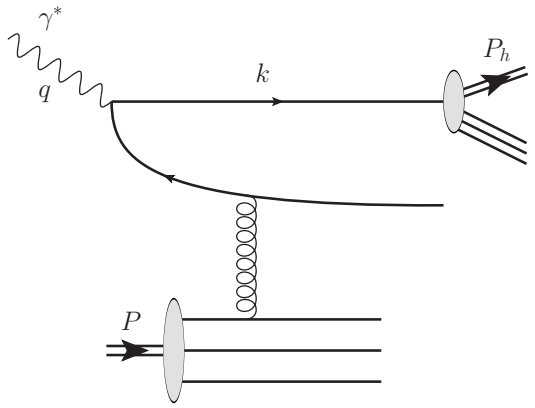

FIG. 2. The SIDIS process at small x. An incoming virtual photon with momentum q decays into a quark–antiquark pair which interacts with the target proton carrying momentum P. The quark and antiquark then fragment into hadrons, and one of these hadrons is detected with momentum P_h.

$$g_1^h(x,z,Q^2) = -\frac{Q^2}{16\pi^2\alpha_{\rm em}\,x}\sum_{\lambda=\pm}\lambda\int {\rm d}^2k_\perp\,{\rm d}^2P_{h\perp}\,\delta^{(2)}(z\,\mathbf{k}_\perp-\mathbf{P}_{h\perp})\sum_{q,\bar q}\frac{{\rm d}\sigma^{\vec{\gamma}^*+\vec{p}\to q+X}}{{\rm d}^2k_\perp}(\lambda,+)\,D_1^{h/q}(z,Q^2)\,, \tag{27}$$

where $\mathbf{k}_\perp$ and $\mathbf{P}_{h\perp}$ are the transverse momentum vectors for the quark and produced hadron in Fig. 2, while $D_1^{h/q}(z,Q^2)$ is the collinear fragmentation function. The sum $\sum_{q,\bar q}$ goes over the produced quarks and antiquarks. While only quark fragmentation is depicted in Fig. 2, an antiquark could instead fragment there, by reverting the particle number flow direction on the quark line in the diagram.

In arriving at Eq. (27) we have employed the aligned jet configuration, dominant in DLA [52, 65], in which $k^-\approx q^-$, such that the produced hadron carries the fraction $P_h^-/k^-\approx P_h^-/q^- = z$ of the quark's momentum. Consequently, we assume that z is not very small, such that the hadron is produced in the forward (virtual photon) direction/current fragmentation region and arises from the fragmentation of the forward-moving quark with 4-momentum k in Fig. 2, and not from the fragmentation of the antiquark, which is separated from the quark by a large rapidity interval. This is similar to the hybrid factorization approach to particle production [126–128]. (The fragmentation of the antiquark in Fig. 2 would contribute to small-z hadron production, and is neglected here since we are interested in order-one values of z.) In addition, the scale in the argument of the fragmentation function could be chosen to be $k_\perp^2$. However, in our small-x kinematics, the typical value of $k_\perp^2$ is not too far from Q^2, allowing us to use Q^2 in the argument of $D_1^{h/q}(z,Q^2)$.

Integrating Eq. (27) over $\mathbf{k}_\perp$ and $\mathbf{P}_{h\perp}$ we obtain

$$g_1^h(x,z,Q^2) = -\frac{Q^2}{16\pi^2\alpha_{\rm em}\,x}\sum_{\lambda=\pm}\lambda\sum_{q,\bar q}\sigma^{\vec{\gamma}^*+\vec{p}\to q+X}(\lambda,+)\,D_1^{h/q}(z,Q^2)\,. \tag{28}$$

Comparing this to Eqs. (26) and (4), we arrive at

$$g_1^h(x,z,Q^2) = \frac{1}{2}\sum_{q,\bar q}e_q^2\,\Delta q(x,Q^2)\,D_1^{h/q}(z,Q^2)\,, \tag{29}$$

reproducing the result in Eq. (2) of Ref. [30] (see also Refs. [123, 129, 130]), derived in the collinear factorization framework. (As we mentioned above, since quarks and antiquarks have different fragmentation functions, the right-hand-side of Eq. (29) cannot be expressed solely in terms of the Δq^+ linear combinations of hPDFs, and the Δq^- functions will enter as well.) We conclude that the expression (29) for the polarized SIDIS structure function is the same in the collinear and small-x formalisms for large z. However, we emphasize that a similar discussion as that surrounding Eq. (7) applies to Eq. (29) regarding its interpretation in the LCOT framework as implicitly including higher-order α_s corrections.

E. Global analysis

Our goal is to describe the world data on the longitudinal double-spin asymmetries in DIS and SIDIS at low x using small-x helicity evolution. We start with the longitudinal DIS asymmetry, $A_\parallel$ (see, *e.g.*, Refs. [29, 131]),

$$A_\parallel = \frac{\sigma^{\downarrow\Uparrow} - \sigma^{\uparrow\Uparrow}}{\sigma^{\downarrow\Uparrow} + \sigma^{\uparrow\Uparrow}} = D(A_1 + \eta A_2)\,, \tag{30}$$

where the arrow $\uparrow$ ($\downarrow$) denotes the lepton spin along (opposite to) the beam direction, and the arrow $\Uparrow$ denotes the target polarization along the beam axis. The kinematic variables are given by

$$D = \frac{y(2-y)(2+\gamma^2 y)}{2(1+\gamma^2)y^2 + (4(1-y) - \gamma^2 y^2)(1+R)}, \quad \eta = \gamma \frac{4(1-y) - \gamma^2 y^2}{(2-y)(2+\gamma^2 y)}\,, \tag{31}$$

where $y = \nu/E$ is fractional energy transfer of the lepton in the target rest frame, $\gamma^2 = 4M^2x^2/Q^2$, and $R = \sigma_L/\sigma_T$ is the ratio of the longitudinal to transverse virtual photoproduction cross sections. When $4M^2x^2 \ll Q^2$ ($\gamma^2 \ll 1$), we have $\eta \ll 1$ and the virtual photon–target asymmetries are

$$A_1 = \frac{g_1 - \gamma^2 g_2}{F_1} \approx \frac{g_1}{F_1}, \quad A_2 = \gamma\, \frac{g_1 + g_2}{F_1} \ll 1\,, \tag{32}$$

implying

$$A_\parallel \approx D\, A_1. \tag{33}$$

Similarly, in polarized SIDIS for the production of a hadron h, the asymmetry A_1^h can be expressed as (see, *e.g.*, Refs. [23, 30])

$$A_1^h = \frac{g_1^h - \gamma^2 g_2^h}{F_1^h} \approx \frac{g_1^h}{F_1^h}\,. \tag{34}$$

In principle there is another observable in the DIS/SIDIS family that could help constrain hPDFs: parity-violating DIS. This process is sensitive to the $g_1^{\gamma Z}$ structure function which is approximately proportional to $\Delta\Sigma$ [132, 133]. Unfortunately there is little to no data for $g_1^{\gamma Z}$ in the small-x ($x < 0.1$) region (see, *e.g.*, Ref. [134]), not allowing us to employ this observable in our analysis.

Between the two scattering processes, we have ten unique observables: two in DIS (proton or deuteron/^{3}He target) and eight in SIDIS (proton or deuteron/^{3}He target with charged pion or kaon final states) from which in principle we can constrain the eight polarized dipole amplitudes (five associated with the flavor singlet hPDFs ($Q_u, Q_d, Q_s, \widetilde{G}, G_2$), and three with the flavor nonsinglet hPDFs ($G_u^{\rm NS}, G_d^{\rm NS}$ and $G_s^{\rm NS}$)). In our formalism, the g_1 and g_1^h structure functions are calculated in terms of hPDFs using Eqs. (4), (29), respectively. (Note that $\Delta q = (\Delta q^+ + \Delta q^-)/2$ and $\Delta\bar{q} = (\Delta q^+ - \Delta q^-)/2$.) This is the bridge connecting small-x helicity evolution to the experimental data. Fitting the hPDFs to $A_\parallel, A_1$ and A_1^h at moderate $x \lesssim 0.1$ allows us to determine the initial conditions of the polarized dipole amplitudes (22), (25). We then evolve the polarized dipole amplitudes toward lower values of x using Eqs. (9) and (13) to obtain hPDFs in that region, and compare with existing data as well as make predictions at smaller x. We mention that the structure functions F_1 and F_1^h involve the unpolarized PDF $q(x, Q^2)$ and, for the latter, the unpolarized fragmentation function (FF) $D_1^{h/q}(z, Q^2)$. We compute F_1 and F_1^h up to next-to-leading order using collinear factorziation and DGLAP evolution, based on the JAM analysis in Ref. [34]. (To be consistent, strictly speaking one should include small-x evolution also for F_1 and F_1^h. However, for us the results of Ref. [34] serve as a faithful proxy of the experimental data for these structure functions. A more comprehensive analysis that also utilizes small-x evolution for F_1 and F_1^h is left for future work.)

Let us present a short discussion about our ability to constrain G_2 and $\tilde{G}$, which are two important polarized dipole amplitudes driving the small-x evolution of the hPDFs. The polarized dipole amplitude G_2 is directly related to the gluon hPDF, per Eq. (20). However, the observables we consider here do not directly couple to the gluon hPDF. Instead, as we saw above, they couple only to quark hPDFs. The dipole amplitude G_2 enters the quark hPDFs Δq^+ along with the dipole amplitude Q_q. Moreover, they always enter in the same linear combination, $Q_q + 2\,G_2$ for $q = u, d, s$ (see Eq. (19)). We see that while G_2 and Q_q couple directly to the spin-dependent structure functions for DIS and SIDIS, we do not have an observable (or a linear combination of observables) in this analysis which separately couples only to G_2 or only to Q_q.

What may help us to separate G_2 and Q_q is the fact that these dipole amplitudes have a different pre-asymptotic form. While it is established numerically that at asymptotically small x, both polarized dipole amplitudes G_2 and Q_q are proportional to the same power of x with the same intercept [96] and are, therefore, probably hard to distinguish, in the pre-asymptotic region where the asymptotic form has not yet been reached, their contributions to the quark hPDFs may be quite different. This can be studied by comparing the Q_u and G_2 basis functions for Δu^+ in Fig. 1, shown in the top and bottom panels of that figure, respectively. If these functions were identical, they could be freely interchanged against each other while still producing the same structure functions: in such a case it would be impossible to separate G_2 and Q_u from the data. Since the contributions of different amplitudes to quark hPDFs differ from each other, as follows from Fig. 1, these basis contributions cannot be adjusted at one value of x while maintaining the same value for the observables at all other x. Therefore, we may be able to separate G_2 and Q_u using the polarized DIS and SIDIS data. However, since the Q_u and G_2 basis functions have similar shapes, per Fig. 1, it might be the case that the uncertainties in the resulting extractions of Q_u and G_2 will be large.

The polarized dipole amplitude $\widetilde{G}$, on the other hand, does not couple to any of the polarized DIS or SIDIS observables we consider here. Rather, it mixes with other polarized dipole amplitudes only through evolution (see Eqs. (9)). This is why the $\widetilde{G}$ basis function of Δu^+ (second from the bottom panel in Fig. 1) appears to be vanishingly small above $x > x_0$. The consequence of this is that in the region of x where the polarized DIS and SIDIS data exist, $5 \times 10^{-3} < x < 0.1$, the $\widetilde{G}$ amplitude is very small and is, therefore, much less constrained by the data than the Q_q and G_2 dipole amplitudes. At small x, however, the $\widetilde{G}$ amplitude is quite large, second only to G_2 (see Fig. 1). As we will see below, $\widetilde{G}$, unconstrained by the existing polarized DIS and SIDIS data, will dominate over the other polarized dipole amplitudes at small x, adversely affecting our ability to make precise predictions at even smaller x. Nevertheless, it is possible that $\widetilde{G}$ might be constrained with slightly more leverage in x. We will discuss this in Sec. III D when we explore the impact of the future EIC data on our uncertainties.

In our global analysis we use the JAM Bayesian Monte Carlo framework (see, *e.g.*, [29, 135, 136]) to randomly sample (roughly 500 times) the space of 24 parameters a, b, c from Eqs. (22) and (25), namely $a_u, b_u, c_u, a_d, \ldots, c_s^{\rm NS}$. For each combination of these parameters, we solve our evolution equations (9) and (13) to determine the polarized dipole amplitudes $Q_u, Q_d, Q_s, \widetilde{G}, G_2, G_u^{\rm NS}, G_d^{\rm NS}$ and $G_s^{\rm NS}$. (The actual numerical solution is facilitated by the basis functions introduced above.) Next, using Eqs. (19) and (24), we calculate the quark hPDFs at small x, which, via Eqs. (4) and (29), can be used to determine the structure functions g_1 and g_1^h that enter the numerator of the asymmetries $A_\parallel, A_1$ (Eqs. (32), (33)) and A_1^h (Eq. (34)), respectively. The χ^2-minimization procedure allows us to construct the posterior distributions of the parameters, and the corresponding solutions of our evolution equations then allow us to infer the quark and gluon hPDFs (the latter via Eq. (20)). These extracted quark and gluon hPDFs, and the quantities that can be computed from them, are the main results of our work, which we present below.

III. RESULTS

In this section we present the results of our numerical analysis. We will concentrate on the proton g_1 structure function, and the quark and gluon hPDFs (along with quantities, such as net spin, that can be computed from them).

A. Data versus theory

Our analysis (JAMsmallx) of the world polarized DIS and SIDIS data at low x utilizes measurements from SLAC [137–141], EMC [142], SMC [143–145], COMPASS [146–148], and HERMES [149, 150] for DIS, and SMC [151], COMPASS [152, 153], and HERMES [154, 155] for SIDIS. The data of interest falls in the Bjorken-x range of $5 \times 10^{-3} < x < 0.1 \equiv x_0$, and the Q^2 range is $1.69\ {\rm GeV}^2 < Q^2 < 10.4\ {\rm GeV}^2$. Since $x \approx Q^2/s$, the minimum cut on Q^2 determines the minimum accessible x in the data set (for a given experimental center-of-mass energy), and conversely the maximum cut on x determines the maximum Q^2. The upper limit on x (denoted by x_0) was chosen based on our previous (DIS-only) work [97], as (almost) the highest value of x which gave a good-χ^2 fit. This x_0 is the point where

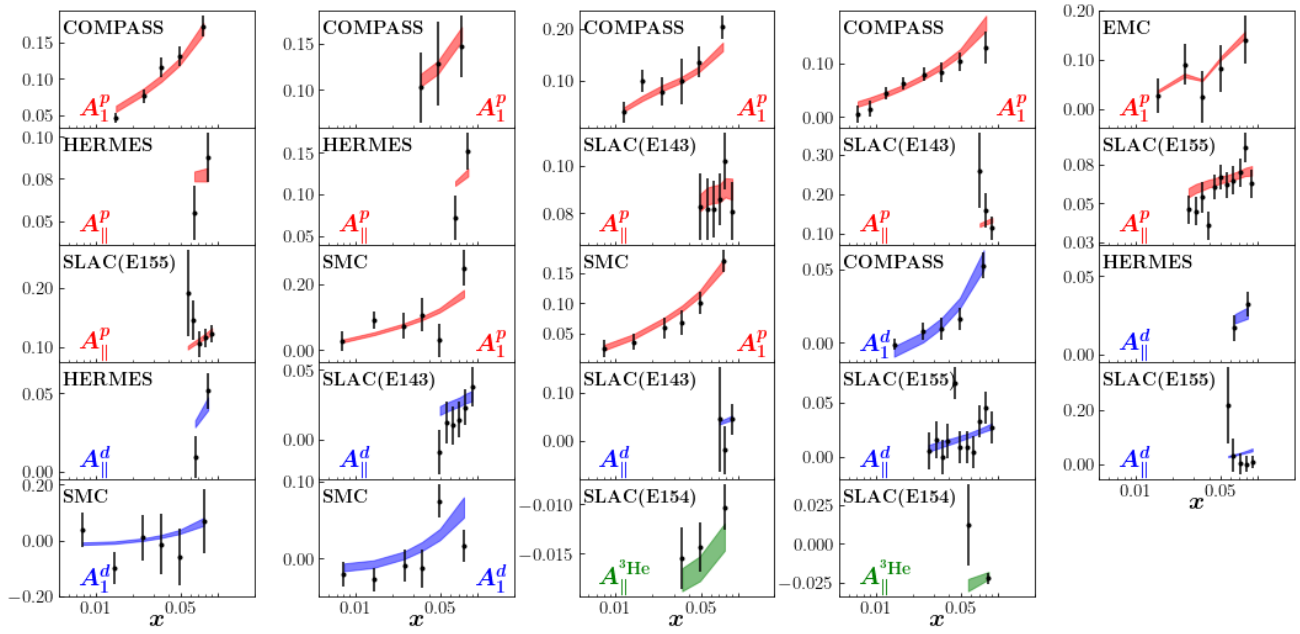

FIG. 3. Comparison of the experimental data and the fit based on our small-x theory for the double-spin asymmetries A_1 and $A_\parallel$ in polarized DIS on a proton (red), deuteron (blue) and ^{3}He (green) target.

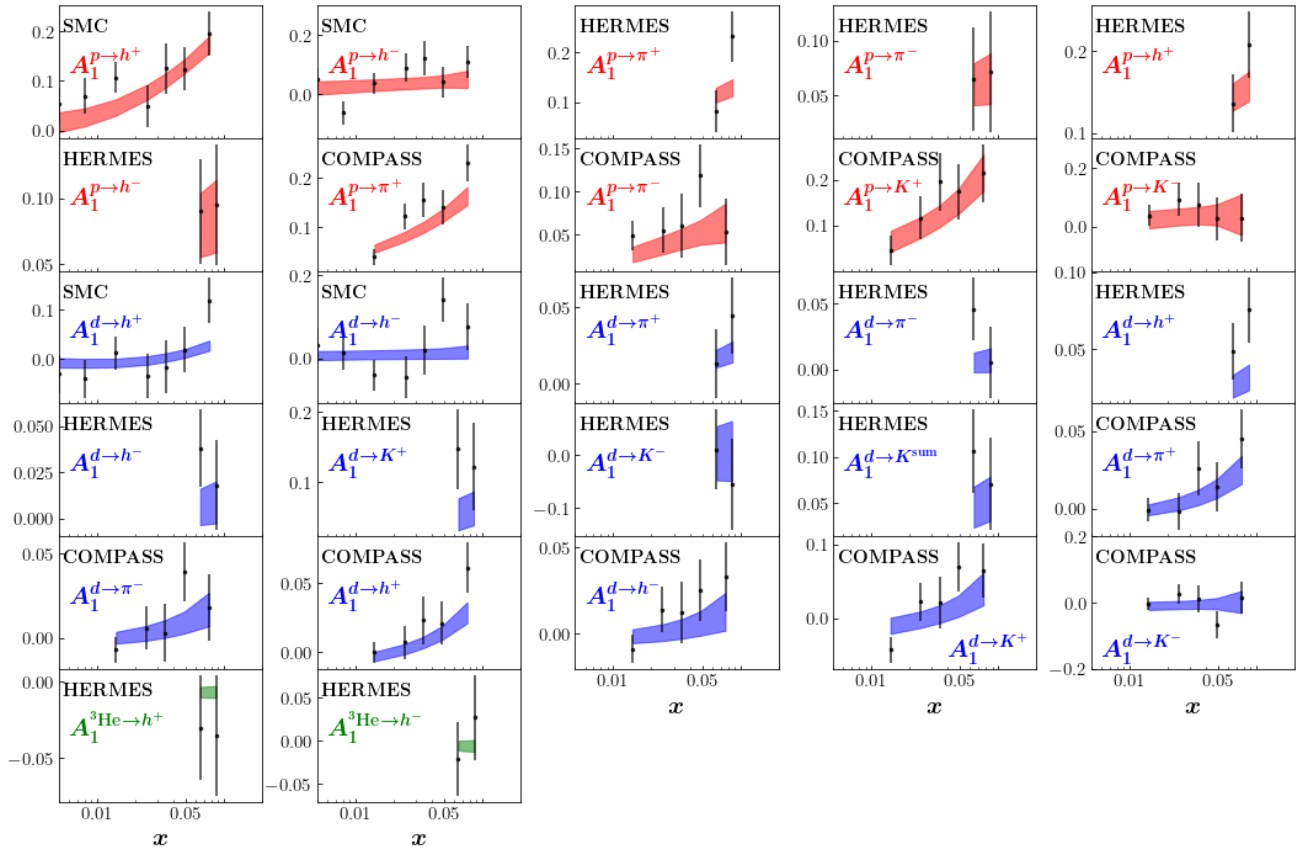

FIG. 4. Comparison of experimental data and fit based on our small-x theory for the double-spin asymmetry A_1^h in polarized SIDIS on a proton (red), deuteron (blue) and ^{3}He (green) target for charged pion, kaon and unidentified hadron final states.

TABLE I. Summary of polarized DIS data included in the fit, separated into A_1 (left) and $A_\parallel$ (right), along with the $\chi^2/N_{\rm pts}$ for each data set.

Data set (A_1)	**Target**	$N_{\rm pts}$	$\chi^2/N_{\rm pts}$
SLAC (E142) [137]	^{3}He	1	0.60
EMC [142]	p	5	0.20
SMC [143, 145]	p	6	1.29
	p	6	0.53
	d	6	0.67
	d	6	2.26
COMPASS [146]	p	5	1.02
COMPASS [147]	p	17	0.74
COMPASS [148]	d	5	0.88
HERMES [149]	n	2	0.73
Total		59	0.91

Data set ($A_\parallel$)	**Target**	$N_{\rm pts}$	$\chi^2/N_{\rm pts}$
SLAC(E155) [140]	p	16	1.28
	d	16	1.62
SLAC (E143) [139]	p	9	0.56
	d	9	0.92
SLAC (E154) [138]	^{3}He	5	1.09
HERMES [150]	p	4	1.54
	d	4	0.98
Total		63	1.19

we start the small-x helicity evolution. The fact that our small-x approach was able to describe data up to such a high value of x could be due to the fact that, unlike the unpolarized Balitsky–Fadin–Kuraev–Lipatov (BFKL) [121, 122], Balitsky–Kovchegov (BK) [69–72] and Jalilian-Marian–Iancu–McLerran–Weigert–Leonidov–Kovner (JIMWLK) [73–78] small-x evolution, which resums powers of $\alpha_s\,\ln(1/x)$ at the leading order, our helicity evolution has a different (larger) resummation parameter, $\alpha_s\ln^2(1/x)$. For $\alpha_s\approx 0.25$, our resumation parameter becomes of order 1 for $x\approx 0.1$. The lower limit of Q^2 is set by the charm quark mass, $m_c^2 = 1.69\,\text{GeV}^2$. This is also the cut placed by the JAM FF set we use [34], which has independent functions for π^+, K^+, h^+ (π^-, K^-, h^- are found through charge conjugation) that we evolve through the DGLAP equations. By analogy to [97], we choose our IR cutoff to be $\Lambda = 1$ GeV. Also, in the Q^2 range specified above, the strong coupling in Eq. (16) is taken with $N_f = 3$ (and $N_c = 3$).

The range of the outgoing hadron momentum fraction z in polarized SIDIS is $0.2 < z < 1.0$, and we do not place any explicit cut on this variable. In practice, the data (after all the appropriate cuts) generally has values of $0.4 < z < 0.6$; some data sets integrate $z\in[0.2,1]$ while others cover $z\in[0.2,0.85]$. After all the cuts we are left 122 polarized DIS data points and 104 polarized SIDIS data points, for a total $N_{\rm pts} = 226$. The overall $\chi^2/N_{\rm pts}$ of our fit, based on the central theory curves, is 1.03. The breakdown of the data by experiment, along with our $\chi^2/N_{\rm pts}$ for those individual data sets, is shown in Table I for DIS and Table II for SIDIS. The plots of the experimental data versus our JAMsmallx theory are shown in Fig. 3 for polarized DIS and Fig. 4 for polarized SIDIS. Overall, our results demonstrate very good agreement with the existing world data.

B. Proton g_1 structure function

We now examine our result for the g_1 structure function of the proton to analyze the predictive capability of our formalism. Our calculation of g_1^p for all replicas is given in Fig. 5. This is the result of 500 individual fits of the experimental data where the (quark and gluon) hPDFs were extracted and then (the quark ones) used to compute g_1^p. We color code each replica by its asymptotic sign at small x in order to clarify the structure of the plot as well as help establish correlations with the hPDFs below. While g_1^p is well constrained in the region where there is experimental data ($5\times10^{-3} < x < 10^{-1}$), it is largely unconstrained at smaller x. The major difficulty in constraining g_1^p is caused by the insensitivity of the data to the G_2 and $\widetilde{G}$ amplitudes described above.

That being said, the asymptotic solution of the large-N_c&N_f evolution equations [96] guarantees that the small x behavior of g_1^p must be exponential in $\ln(1/x)$. This implies that it has to pick a sign (positive or negative) when $x\to 0$. Our results indicate (see Fig. 7) that, given the existing experimental data constraining our formalism, the asymptotic sign is likely to be picked by $x = 3.5\times10^{-4}$ with 10% uncertainty, with the uncertainty decreasing to 5% at approximately $x = 2.5\times10^{-5}$. Currently, 70% of the replicas are asymptotically positive and 30% are asymptotically negative. These percentages are stable as the number of replicas increases. The primary source of uncertainty is how low in x one must go to determine the sign, as some replicas that appear positive may undergo a sign change at smaller x.

TABLE II. Summary of the polarized SIDIS data on A_1^h included in the fit, along with the $\chi^2/N_{\rm pts}$ for each data set.

Dataset (A_1^h)	**Target**	**Tagged Hadron**	$N_{\rm pts}$	$\chi^2/N_{\rm pts}$
SMC [144]	p	h^+	7	1.03
	p	h^-	7	1.45
	d	h^+	7	0.82
	d	h^-	7	1.49
HERMES [154]	p	π^+	2	2.39
	p	π^-	2	0.01
	p	h^+	2	0.79
	p	h^-	2	0.05
	d	π^+	2	0.47
	d	π^-	2	1.40
	d	h^+	2	2.84
	d	h^-	2	1.22
	d	K^+	2	1.81
	d	K^-	2	0.27
	d	$K^+ + K^-$	2	0.97
HERMES [155]	^{3}He	h^+	2	0.49
	^{3}He	h^-	2	0.29
COMPASS [152]	p	π^+	5	1.88
	p	π^-	5	1.10
	p	K^+	5	0.42
	p	K^-	5	0.31
COMPASS [153]	d	π^+	5	0.50
	d	π^-	5	0.78
	d	h^+	5	0.90
	d	h^-	5	0.86
	d	K^+	5	1.50
	d	K^-	5	0.78
Total			104	1.01

1. *Sign of g_1^p and quantifying numerical ambiguity*

From Fig. 5 alone, one can make the qualitative observation that indeed each replica of g_1^p grows exponentially with $\ln(1/x)$ as we suggested earlier, and the color indicates the asymptotic sign of g_1^p for that given replica. We mentioned in the previous section that the exponential behavior of helicity functions in our theory makes it difficult for a given replica to maintain a near-zero value, and thus it must eventually choose to (rapidly) increase in magnitude towards positive or negative values. Given the numerical nature of our global analysis, we cannot compute each fitted replica down to $x = 0$ (corresponding to $\ln x \to -\infty$), so the color-coding and sign assignment is determined by the slope of a replica at the lowest-computed value of x: if the slope increases (decreases) as x goes to zero, then it is considered "asymptotically" positive (negative). To balance our time and computational resources, the results discussed in this section use replica data computed down to $x_{\rm asymp} = 10^{-7.5}$. One may realize potential issues with this system: a given replica may have multiple different "asymptotic" signs depending on the lowest computed value of x.

Any given replica is defined by its specific combination of basis functions, and since our Bayesian analysis samples parameters (Eq. 21) that may be either positive or negative, competition between basis functions can result in nodes. Replicas with two nodes in $g_1^p(x)$, such as the one illustrated in Fig. 6, can occur for linear combinations of similar basis functions with opposite signs, as in the top/bottom panels of Fig. 1. These changes in sign can occur at various values of x depending on the initial conditions, making the prediction of the asymptotic sign dependent on what x value is used to make the prediction.

Careful readers may have already noticed this from Fig. 5, where there are a few red-coded replicas that appear to be growing negative (and a blue-coded replica that appears to be growing positive) at $x = 10^{-5}$. This is due to

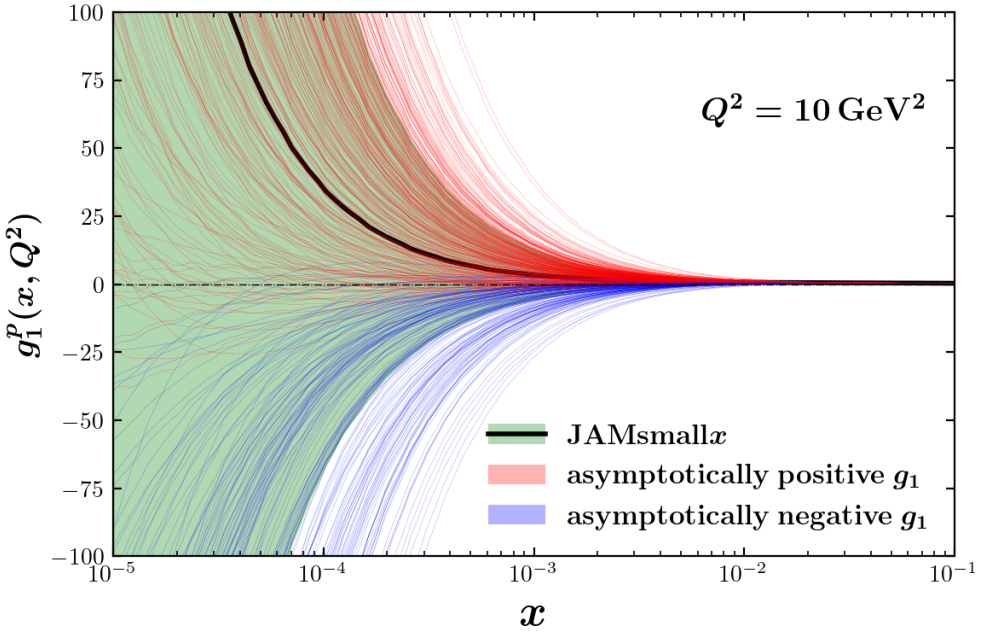

FIG. 5. The small-x calculation of the g_1 structure function of the proton. The black curve is the mean of all the replicas with the green band giving the 1σ uncertainty. Red (blue) curves are solutions that are asymptotically positive (negative).

each of these replicas having a delayed critical point ($\frac{\mathrm{d}\, g_1^p(x)}{\mathrm{d}\, x} = 0$) that occurs at $x < 10^{-5}$, where a different basis function takes over the growth and the replica changes the sign of its slope. These critical points also are connected to the issue of *ambiguity*, where at a specific value of x we may be able to measure that a replica is *growing* positive (or negative) but has a magnitude that is actively negative (or positive), leaving its asymptotic sign unconfirmed. Luckily, investigations of these incidents show that they occur in a statistically small portion of replicas from the perspective of our considerably small x_{asymp}.

Since our goal is predictability at small x, we decided to quantify the amount of ambiguity by its probability density in x. That is, for each replica we count the smallest-x instance of ambiguity, and take note of where in x it occurred. For example, Fig. 6 shows a replica that begins positive (true for all replicas) and evolution drives it more positive until it reaches a critical point, after which the replica then grows negative. After the critical point (in the gray region), the replica will be considered *ambiguous* until it crosses $g_1^p(x_1) = 0$, and then it is considered asymptotically negative (in the blue region). Only when the sign of g_1^p and the sign of its first derivative (as x decreases) agree can the replica be considered asymptotically positive or negative. If we wanted to predict the asymptotic sign of the replica based on an observation at $x = x_{\mathrm{pred}}$ that resides in this (blue) region, then we would predict that this replica is "asymptotically negative" as $x \to 0$. However, this same replica has a small-x critical point (around $x = 10^{-4}$) that causes the sign of its slope to change; the replica observed in the (gray) region (on the left) between the critical point and $g_1^p(x_2) = 0$ would be considered ambiguous again. After crossing zero a second time, a prediction made at $x_{\mathrm{pred}} < x_2$ would therefore designate the replica to be "asymptotically positive." The smallest-x instance of ambiguity is thus counted in a bin at x_2. In this way, each replica is counted exactly once, and replicas that oscillate multiple times about the $g_1^p = 0$ axis only have their most delayed ambiguity counted. We can define the number of replicas that have their smallest-x instance of ambiguity in a particular bin of x as $C_A(x)$ (the counts of ambiguities) and make a histogram. The ambiguity count $C_A(x)$ is normalized such that it sums to the total number of replicas N_{ambig} containing at least one ambiguity:

$$\sum_{x=x_{\mathrm{asymp}}}^{x_0} N_{\mathrm{ambig}} \leq N_{\mathrm{tot}}\,. \tag{35}$$

Because some replicas are always unambiguous across the entire range of x, the ambiguity count is less than the total number of replicas: $N_{\mathrm{ambig}} \leq N_{\mathrm{tot}}$.

Now suppose we want to predict the asymptotic behavior of g_1^p at small x based on the behavior of the function at some value x_{pred}. Knowledge of the ambiguity count $C_A(x)$ allows us to estimate the accuracy of this prediction by

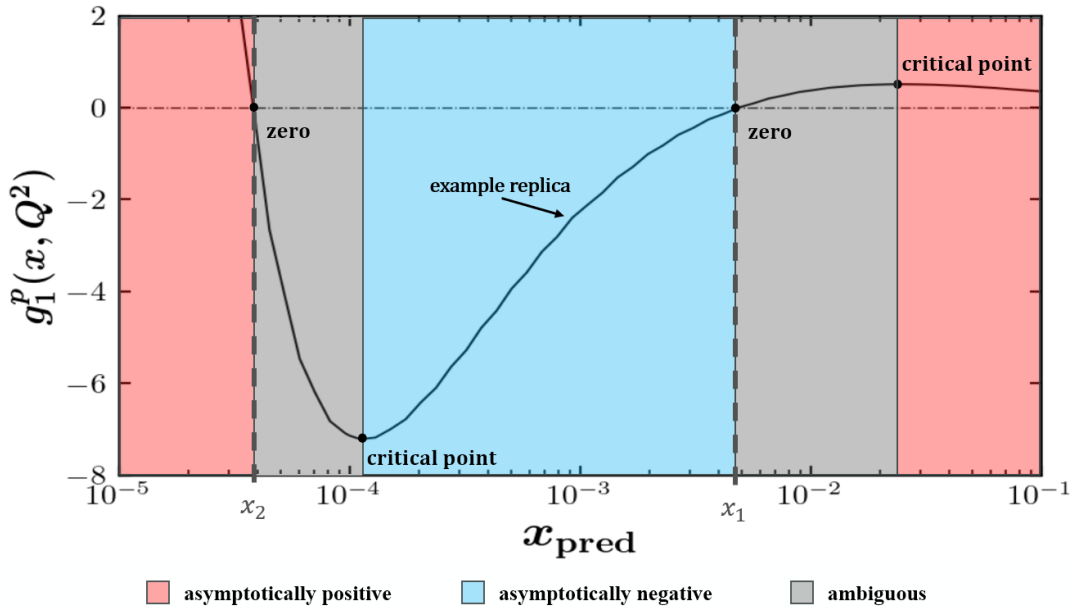

FIG. 6. An example replica of $g_1^p(x, Q^2 = 10\,\mathrm{GeV}^2)$ that demonstrates how the asymptotic sign is dependent on x_{pred}. If x_{pred} resides in the red (blue) region then the replica will be considered asymptotically positive (negative) according to the sign of the first derivative (for decreasing x), and its agreement with the sign of the magnitude. If x_{pred} resides in either gray region then the asymptotic sign is ambiguous due to a contradiction between the sign of the slope and the sign of the magnitude.

estimating the probability that an unobserved ambiguity remains at $x_{\mathrm{asymp}} < x < x_{\mathrm{pred}}$. This probability is given by a summation as in Eq. (35), but over the truncated range in x:

$$\mathcal{A}(x_{\mathrm{pred}}) = \frac{1}{N_{\mathrm{rep}}} \sum_{x=x_{\mathrm{asymp}}}^{x_{\mathrm{pred}}} C_A(x)\,. \tag{36}$$

From the normalization condition (35), we see that Eq. (36) implies the truncated moment is normalized at $x_{\mathrm{pred}} = x_0$ to the total fraction of replicas containing at least one ambiguity:

$$\mathcal{A}(x_0) = \frac{N_{\mathrm{ambig}}}{N_{\mathrm{rep}}}\,. \tag{37}$$

From the left panel of Fig. 7 we see that the number of smallest-x ambiguities decreases greatly as x approaches zero. The right panel shows we must go down to approximately $x = 3.5 \times 10^{-4}$, 2.5×10^{-5}, and 6×10^{-7} to capture the asymptotic sign with 10%, 5%, and 1% uncertainty, respectively. This is strong justification that $x_{\mathrm{asymp}} = 10^{-7.5}$ is reasonably low enough to capture the asymptotic sign of our replicas with low uncertainty. Due to Eq. (37) we also know how many replicas are completely unambiguous; since we impose our evolution to begin at $x_0 = 0.1$, the running integral at that point quantifies the total ratio of replicas that have at least one ambiguity. According to the right panel of Fig. 7, approximately 50% of replicas choose their asymptotic sign immediately as evolution begins. Note that the data constrains the initial condition for g_1^p to be positive, so all completely unambiguous replicas are asymptotically positive.

Furthermore, splitting the replicas by their asymptotic sign (not shown in Fig. 7) allows us to also investigate how early (or late) the different solutions are chosen relative to each other. We gather that ambiguously negative replicas tend to choose their sign earlier than their positive counterparts, with the caveat that the majority of asymptotically positive replicas do not have any ambiguities at all. Approximately 75% of asymptotically positive replicas are completely unambiguous, and the remaining 25% are determined by $x \approx 2 \times 10^{-5}$ with 5% uncertainty. Though fewer in number, a still significant portion of replicas are asymptotically negative, 95% of which are confirmed by $x \approx 4.3 \times 10^{-4}$. This suggests that using a lower x_{pred} will affect the positive-identified and negative-identified solutions differently. In particular, a lower x_{pred} is likely to identify a greater number of asymptotically positive solutions by correcting replicas that would have been misidentified as asymptotically negative at a higher x_{pred}. This asymmetric impact on positive-identified versus negative-identified solutions can be traced back to constraints from the data at large x, which strongly prefers $g_1^p > 0$. The fact that this positive preference persists down to small x suggests that

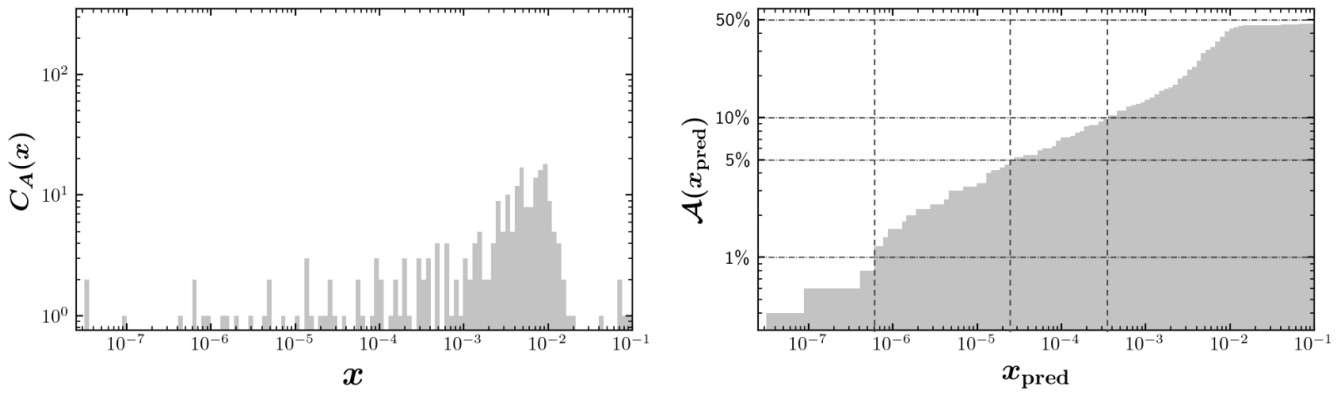

FIG. 7. (Left) Histogram that counts the number of replicas with a smallest-x ambiguity at a given value of x. (Right) The running sum of the ambiguity histogram, telling us what percentage of replicas have an ambiguity below a given value of x.

the polarized dipole(s) which dominate the small-x asymptotics are partially (but not fully) constrained by the large-x data. This will be discussed in detail in Sec. III B 3.

We performed a similar analysis of the smallest-x critical points of each replica (rather than the ambiguities). On average, the smallest-x critical point occurs 4% earlier in $\ln(1/x)$ than its smallest-x zero. Since the ambiguous region of a replica is precisely the region in x between its critical point and zero, this small 4% difference indicates that any remaining ambiguities are quickly resolved at small x. Thus, we conclude that, from the perspective of Fig. 7, if we had data down to $x \approx 10^{-5}$ we could determine the asymptotic sign of g_1^p with high certainty ($> 95\%$).

2. *Asymptotic behavior of g_1^p*

Collectively utilizing the information in Figs. 5 and 7 paints a curious picture: there are many more g_1^p replicas that adopt their asymptotic forms early than there are replicas that change their signs at small x. This results in some clustering behavior, *e.g.*, in the left panel of Fig. 7 there is a cluster of replicas around $x = 5 \times 10^{-3}$, implying that these replicas share similar critical points and rates of growth. As mentioned previously, the majority of replicas have no ambiguities and adopt their asymptotic growth rather quickly, effectively clustering their critical points at $x = x_0 \equiv 0.1$ (not explicitly shown). This behavior supports the idea that early adoption of asymptotic growth is preferred, whereas replicas with late critical points are fewer in nature. Consequently, we expect that there should be a form of bimodality in g_1^p between the rapidly growing *positive* solutions versus the rapidly growing *negative* solutions. This is a novel result, which we quantitatively analyze below.

While Fig. 5 may appear to show the anticipated bimodality (red versus blue curves), upon closer inspection the values of g_1^p are normally distributed, both at small x ($x = 10^{-3}$) and very small x ($x = 10^{-7.45}$), as depicted in Fig. 8. To uncover the bimodal behavior it is necessary to construct a new observable related to the *curvature* of

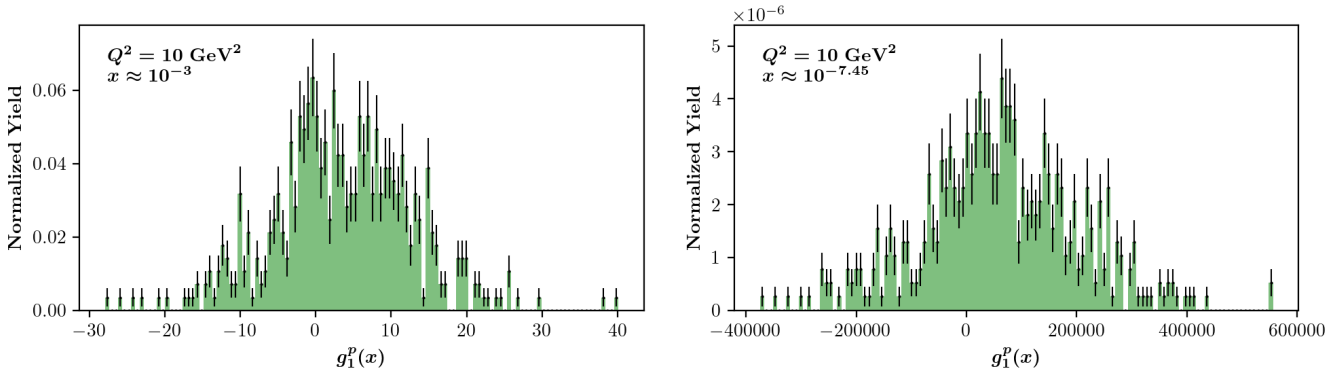

FIG. 8. Histograms counting all values of g_1^p at $x = 10^{-3}$ (left) and $10^{-7.45}$ (right), displaying normal distributions centered slightly above zero.

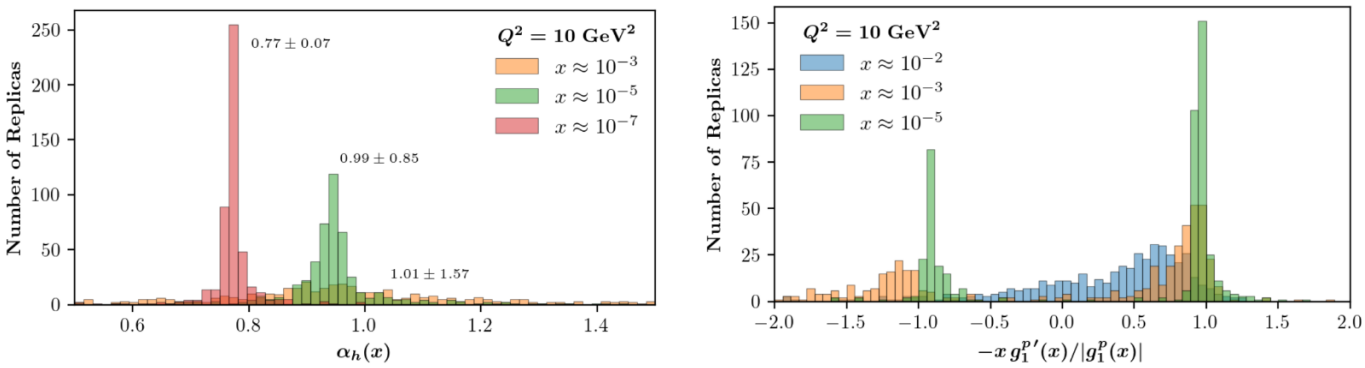

FIG. 9. (Left) Histograms utilizing Eq. (38) showing that as x decreases, the intercept $\alpha_h(x)$ becomes more constrained as a consequence of the small-x evolution equations. (Right) Keeping information on the sign dependence by using Eq. (39) produces bimodal peaks at $\pm\alpha_h(x)$. At large x there is no asymptotic behavior, and for smaller values of x two refined peaks emerge.

g_1^p which is sensitive to how quickly our evolution equations drive the g_1^p replicas toward the asymptotic limit. The emphasis, therefore, is not so much on g_1^p as on the exponent of its power-law behavior at small-x, *i.e.*, $g_1^p(x) \sim x^{-\alpha_h}$. The generalized x-dependent exponent $\alpha_h(x)$ can be extracted through the logarithmic derivative of g_1^p:

$$\lim_{x\to 0} g_1^p(x) \equiv g_1^{p\,(0)}\, x^{-\alpha_h(x)} \qquad \therefore \qquad \alpha_h(x) \equiv \frac{1}{g_1^p(x)} \frac{\mathrm{d}\, g_1^p(x)}{\mathrm{d}\ln(1/x)}, \tag{38}$$

where $g_1^{p\,(0)} = \text{const}$. Examining the distribution of $\alpha_h(x)$ across replicas can provide complementary information to the distribution of $g_1^p(x)$ itself. Notably, the exponent provides a meaningful way to scale the solutions: if they have the same $\alpha_h(x)$, they have the same *curvature*, whether the magnitude of $g_1^p(x)$ is large or small. To further capture the *signed* behavior of $g_1^p(x)$ at small x and distinguish between solutions trending positive or negative at small x, we can generalize the logarithmic derivative (38) to reflect the sign of g_1^p itself:

$$\alpha_h(x) = \frac{1}{g_1^p(x)} \frac{\mathrm{d}\, g_1^p(x)}{\mathrm{d}\ln(1/x)} \qquad \Rightarrow \qquad \mathrm{Sign}\big[g_1^p(x)\big]\, \alpha_h(x) = \frac{1}{\big|g_1^p(x)\big|} \frac{\mathrm{d}\, g_1^p(x)}{\mathrm{d}\ln(1/x)}\,. \tag{39}$$

Both the effective exponent $\alpha_h(x)$ (38) and its signed generalization (39) are shown in Fig. 9 at varying values of x (from the same global fit that produced Fig. 5). (We remark that if a g_1^p replica has a delayed critical point it will result in a delayed zero that may cause an artificially large ratio if $g_1^{p\prime}(x) \gg g_1^p(x) \approx 0$. In order to avoid these statistical outliers, any replica with a ratio value outside of 5σ from the average are omitted from the results in Fig. 9.) The distribution in the right panel at $x = 10^{-2}$ (blue histogram) is skew-normal, which is expected since we are definitively outside of the asymptotic regime. However, at $x = 10^{-3}$ (yellow histogram) we already see the formation of two separated peaks, one positive and one negative. As x continues to decrease down to $x = 10^{-5}$ (green histogram), the two peaks become more refined as the evolution equations predict specific curvature related to the intercept α_h (see Eq. (39)). Without the sign dependence, as displayed in the left panel of Fig. 9, as $x \to x_{\text{asymp}}$, a single peak emerges that approaches the expected asymptotic value for α_h. The decreasing uncertainties are a consequence of our small-x evolution, where the predictive power constrains the value of $\alpha_h(x)$.

From the perspective of the right panel of Fig. 9 it appears that data sensitive to this curvature at x as large as $x = 10^{-3}$ may be enough to identify which bimodal peak g_1^p belongs to. Unambiguously identifying this curvature will provide us the asymptotic sign of g_1^p as well as the asymptotic sign of all the (flavor singlet) hPDFs, as will be discussed below. The fact that such a conclusion could be made at $x \approx 10^{-3}$ by analyzing the *curvature* of $g_1^p(x)$, compared to $x \approx 10^{-5}$ by studying $g_1^p(x)$ itself (see the discussion around Fig. 7), makes the idea of curvature a useful quantity to consider once future low-x data is available from the EIC.

3. *Origins of asymptotic behavior*

To understand what differentiates the positively and negatively growing solutions for g_1^p displayed in Fig. 5, we examine the polarized dipole amplitude parameters themselves, defined in Eqs. (22). We note that the experimental data is only sensitive to the polarized dipole amplitudes as a whole, and not to any specific basis function. For

example, combining Eqs. (32), (4), and (5) shows that A_1 is constructed from the dipole amplitudes Q_q and G_2, and any combination of parameters that reconstructs the experimental data with good χ^2 is equally valid. An appropriate change of variables can reorganize the basis hPDFs to increase the sensitivity to their overall sign. We can then classify which of these parameters are most correlated with the asymptotic sign of g_1^p. We find enhanced sensitivity to the asymptotic sign of g_1^p from the linear combinations $a' \equiv (a+b)/2$ and $b' \equiv (a-b)/2$. Then the dipole initial condition $G^{(0)} = a\,\eta + b\,s_{10} + c$ can be written as

$$G^{(0)} = a'\,(\eta + s_{10}) + b'\,(\eta - s_{10}) + c\,. \tag{40}$$

These new basis functions are displayed in Fig. 10. Compared to Fig. 1, the alternative parameters a', b' change the shape of the basis hPDFs. In particular, we note that this greatly increases the separation between the $a'_2 = 1$ and $b'_2 = 1$ basis functions at large x where the data provides constraints. When we bin the replicas into asymptotically positive/negative g_1^p at small x, we find the largest difference between the values of $\tilde{a}'$ associated with the two asymptotic behaviors. The asymptotically-positive solutions preferred a negative parameter $\tilde{a}' = -1.56 \pm 2.32$, while the asymptotically-negative solutions preferred the positive $\tilde{a}' = 1.42 \pm 2.34$. No other systematic differences in parameters were observed.

We can understand from the basis hPDFs shown in Fig. 10 why asymptotically-positive/negative g_1^p correlates, respectively, with negative/positive values of $\tilde{a}'$, and why $\tilde{a}'$ shows the greatest discrimination power. First, we note that the basis hPDFs themselves are negative-definite functions of x for positive values of the initial parameters a', b', c, which is simply a consequence of the explicit minus sign in Eq. (5). Second, we note that the hPDFs arising from both the $\widetilde{G}^{(0)}$ (with parameters $\tilde{a}', \tilde{b}', \tilde{c}$) and $G_2^{(0)}$ (with parameters a'_2, b'_2, c_2) initial conditions are comparably large at small x; the $a'_2 = 1$ basis function also being sizeable at large x, whereas the $\widetilde{a}'$ basis function only contributes meaningfully at small-x. The large-x behaviour means that the parameter a'_2, while important for determining the small-x asymptotics, is constrained by higher-x experimental data, and it specifically prefers *negative* values: $a'_2 = -0.98 \pm 1.00$. The origin of the different asymptotic behaviors seen in Fig. 5 therefore appears to be due to the dipole $\widetilde{G}$, which makes no contribution to the basis hPDFs at larger x, and, thus, the sign of $\tilde{a}'$ evades experimental constraints.

To test this hypothesis, we ran fits where all of the $\widetilde{G}$ initial condition parameters $(\tilde{a}, \tilde{b}, \tilde{c})$ were restricted to either be negative-definite or positive-definite, with all other parameters unchanged. All g_1^p replicas in the negative-definite $\widetilde{G}$ fit were asymptotically positive. The positive-definite $\widetilde{G}$ fit was slightly less selective but still generated a 73% majority preferring asymptotically negative g_1^p replicas (recall the original fit in Fig. 5 had a 70% *positive* preference). The results, shown in the top row of Fig. 11, clearly demonstrate that the sign of the $\widetilde{G}$ dipole amplitude determines the small-x asymptotics of g_1^p, as anticipated by the basis functions in Figs. 1 and 10.

The reason $\widetilde{G}$ leads to a g_1^p that is poorly constrained at small x can be seen directly from Eqs. (4)–(6), (9) and

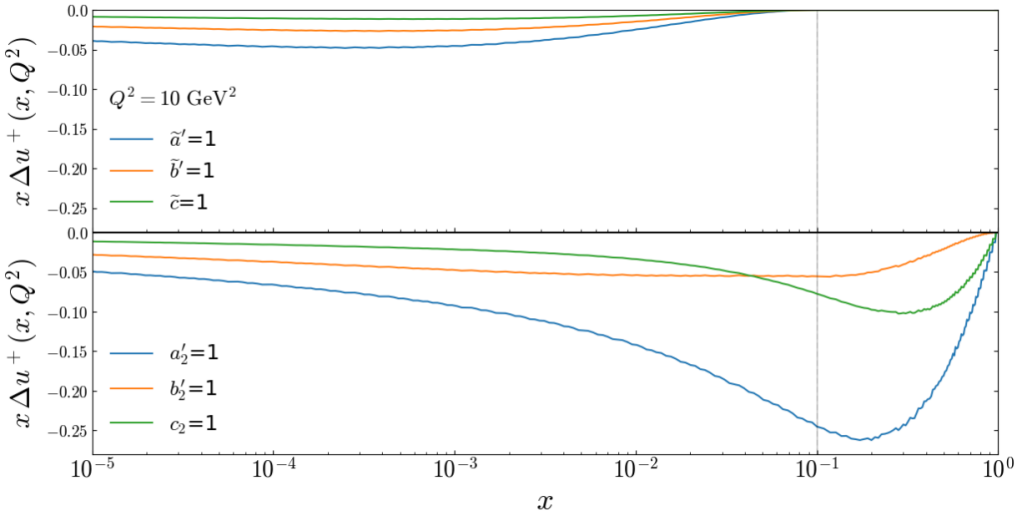

FIG. 10. Basis functions analagous to those in Fig. 1, where instead of plotting the η, s_{10}, and 1 contributions (displayed as the curves in Fig. 1 labeled $a = 1$, $b = 1$, $c = 1$, respectively), we instead show the contributions of $\eta + s_{10}$, $\eta - s_{10}$, and 1 displayed as the curves labeled $a' = 1$, $b' = 1$, and $c' = c = 1$. Here only the $\widetilde{G}$ and G_2 dipole amplitudes are shown.

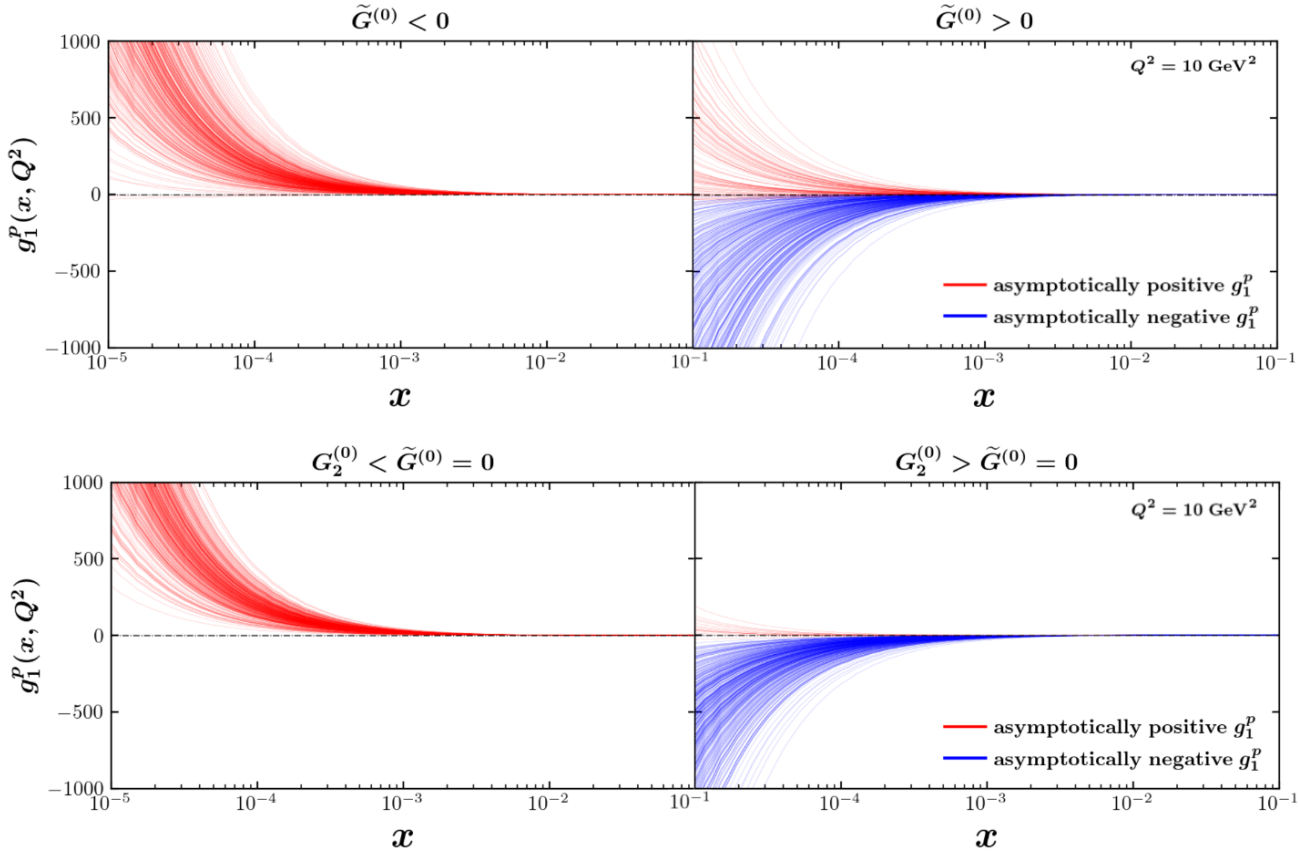

FIG. 11. Comparing the effect $\widetilde{G}$ and G_2 has on the overall sign of $g_1^p(x)$ at small-x. Top row: the priors are restricted so that (left) $\widetilde{G} \leq 0$ and (right) $\widetilde{G} \geq 0$. Bottom row: the priors are restricted so that (left) $G_2 < \widetilde{G} = 0$, and (right) $G_2 > \widetilde{G} = 0$. All other parameters initially are randomly sampled just as they were in the fit shown in Fig. 5. We see that controlling the sign of $\widetilde{G}$ strongly influences the sign of g_1^p, and that the sign of G_2 will also influence the sign of g_1^p.

Eqs. (12), (13), (29): $\widetilde{G}$ does not contribute directly to any hPDF. Whereas all the other (non-neighbor) polarized dipole amplitudes directly enter a DIS/SIDIS observable, the effects of $\widetilde{G}$ are only felt indirectly through its impact on the evolution of the other amplitudes. As a result, hPDFs mediated by $\widetilde{G}$ only become large at very small x (see the top panel of Fig. 10), where there are no constraints from data.

While $\widetilde{G}$ is the driving factor in determining the small-x asymptotics of g_1^p, G_2 also plays a role. In fact, if $\widetilde{G}$ was removed, G_2 would be the most important amplitude in controlling the small-x asymptotics of g_1^p. We see this explicitly when setting the initial conditions for $\widetilde{G}$ all to zero ($\tilde{a} = \tilde{b} = \tilde{c} = 0$) and repeating the previous analysis of now restricting the G_2 initial condition parameters to be always positive or always negative. The result, shown in the bottom panel of Fig. 11, confirms that, although constrained by large-x data, G_2 plays the second-most important role after $\widetilde{G}$ in determining the small-x asymptotics of g_1^p. The negative-definite G_2 fit was 100% selective of asymptotically positive g_1^p replicas, while the positive-definite G_2 fit was 96% selective of asymptotically negative g_1^p replicas.

Knowing now that the dipole amplitude $\widetilde{G}$ controls the small-x asymptotics of g_1^p gives us powerful insight into the hPDF correlations which characterize the fits. Comparing Eqs. (4), (5), and (6) we can draw the conclusion that at asymptotically small x these quantities are simply related by

$$\begin{aligned} g_1^p(x) \propto \Delta q^+(x) \sim -(Q_q + 2G_2) \to -\widetilde{G}, \\ \Delta G(x) \sim G_2 \to \widetilde{G}\,, \end{aligned} \tag{41}$$

where the last step in each line represents the fact that the evolution of Q_q and G_2 is driven by $\widetilde{G}$ (see Eqs. (9)). At small x, the two hPDFs Δq^+ and ΔG are both driven by the same polarized dipole amplitude $\widetilde{G}$, but have opposite signs. Since g_1^p is proportional to Δq^+ (weighted by quark electric charge squared and summed over flavors), it follows that if the quark hPDFs for all flavors have the same sign, then, at small x, g_1^p will have the same sign as the quark hPDFs and opposite sign as the gluon hPDF. These anticipated (anti)correlations among the hPDFs are shown in

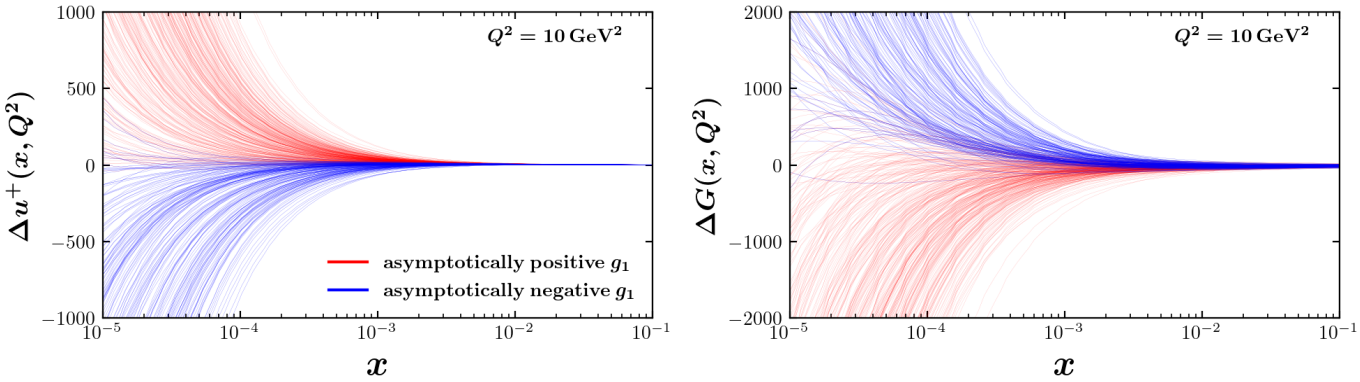

FIG. 12. Color coding the hPDF replicas according to the asympotic sign of g_1^p shows that there is a novel correlation: at small x, quark hPDFs (left) have the same sign as g_1^p (only Δu^+ is shown) while the gluon hPDF (right) has the opposite sign as g_1^p.

Fig. 12, where we plot only Δu^+ and ΔG for brevity. Note that the color coding used for the replicas in Fig. 12 indicates the ultimate asymptotic sign of g_1^p, not the hPDF itself. That is, an hPDF replica is colored red (blue) if the corresponding g_1^p replica is asymptotically positive (negative). The fact that the asymptotic signs of Δq^+ and ΔG are, respectively, correlated and anti-correlated to the sign of g_1^p at small x is a robust, novel prediction of the small-x helicity evolution framework.[3] Thus, in order to better predict the asymptotic sign of g_1^p, Δq^+ and ΔG, we need to better constrain the polarized dipole amplitude $\widetilde{G}$. One option is data from the future EIC, discussed in the next section. We also outline several additional ways in Sec. III E.

C. Calculation of helicity PDFs, net parton spin and axial charges at small x

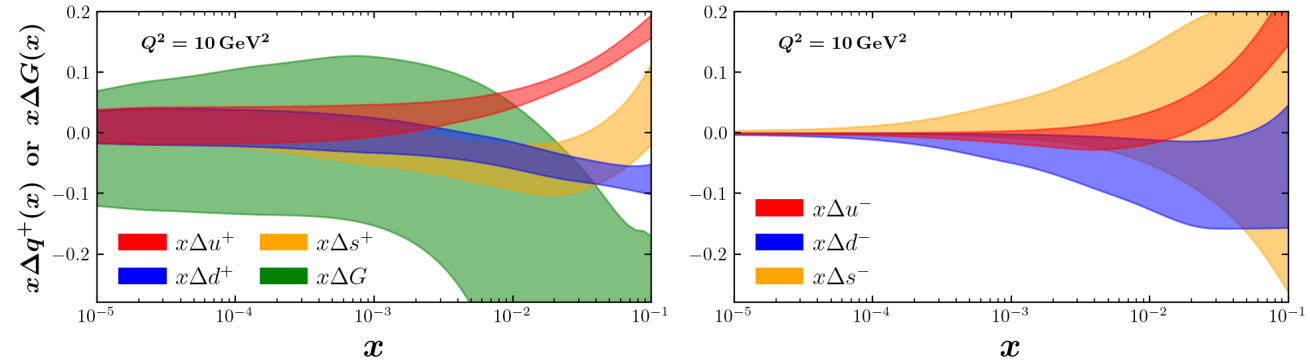

FIG. 13. (Left) Flavor singlet hPDFs $x\Delta u^+$ (red), $x\Delta d^+$ (blue), $x\Delta s^+$ (orange) and $x\Delta G$ (green). The band represents the extraction based on experimental data. (Right) Same as left panel, but for the flavor nonsinglet hPDFs $x\Delta u^-$ (red), $x\Delta d^-$ (blue), $x\Delta s^-$ (orange).

Our results for x times hPDFs are summarized in Fig. 13. Note that our small-x analysis is only valid for $x < x_0 = 0.1$, so the bands in Fig. 13 are only plotted in that range. Similar to the g_1^p structure function, our hPDFs in Fig. 13 exhibit broad uncertainty bands. (Let us stress that in Fig. 13 we plot x times hPDF on the vertical axis: this explains why the error bands in Fig. 13 appear to be smaller than those in Fig. 16, with the latter showing g_1^p without any additional factors of x on the vertical axis.)

[3] We note that no such relationship is exhibited by the nonsinglet hPDFs. When attempting the same strategy of color coding the nonsinglet hPDFs (not shown) according to the asymptotic sign of $g_1^{p\to h}$ (proton SIDIS structure function), no correlations could be identified.

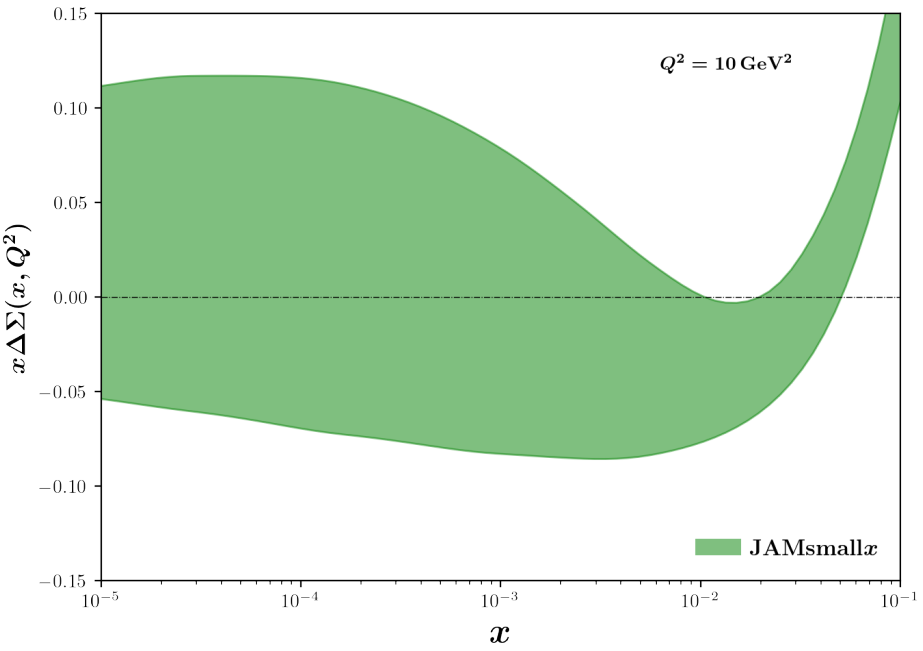

FIG. 14. Flavor singlet helicity function $x\Delta\Sigma(x,Q^2)$. The green band is from fitting existing experimental data.

Studying our hPDFs, one notices that Δs^+ and ΔG are much larger in magnitude than the same hPDFs obtained in the JAM framework using the DGLAP-based approach [30, 33, 34]. To make sure we agree with Refs. [30, 33, 34], we have performed a separate fit of the data setting $\Delta s^+ = \Delta s^- = 0$ and still obtain a good value of $\chi^2/N_{\rm pts} = \ldots$. Therefore, small $|\Delta s^+|$ is indeed consistent with our formalism. A reason for the apparent difference between the magnitude of our Δs^+ and that in Refs. [30, 33, 34] could be due to our extraction being limited to small-x DIS and SIDIS data only, while the analyses in Refs. [30, 33, 34] include large-x data as well. Additionally, some of the largeness of our Δs^+ error band (making the allowed range of Δs^+ values rather wide) possibly is due to the uncertainties in our evolution, driven by the inability of the present polarized DIS and SIDIS data at small x to constrain the amplitudes $\widetilde{G}$ and G_2, as discussed above. This latter reason is certainly the main driving force for the broad error bands in ΔG, as we will elaborate on in Sec. III E.

This conclusion is further supported by the left panel of Fig. 13, which exhibits approximately the same error band for Δu^+, Δd^+ and Δs^+ at small x, below $x \approx 10^{-4}$. This is in contrast to markedly different error bands for Δu^-, Δd^- and Δs^-, shown in in the right panel Fig. 13. The similarity of the error bands for Δu^+, Δd^+ and Δs^+ appears to be driven by the error band of the dipole amplitude G_2, which affects all quark flavors in the same way, per Eq. (19). Since $G_2 \sim \Delta G$, as follows from Eq. (20), we see that our inability to narrow down the error band for the quark hPDFs stems from the same uncertainty in G_2, and, hence, in $\widetilde{G}$, that we discussed above.

Given the hPDFs in Fig. 13, we construct the flavor singlet helicity function,

$$\Delta\Sigma(x,Q^2) \equiv \Delta u^+(x,Q^2) + \Delta d^+(x,Q^2) + \Delta s^+(x,Q^2)\,, \tag{42}$$

for the light flavors considered in our work. We plot $x\Delta\Sigma(x,Q^2)$ in Fig. 14. Again, the uncertainty band at small x based on current experimental data is rather wide. Below we will see that the uncertainties in $\Delta\Sigma$ and ΔG, shown in Figures 13 and 14, are, in fact, correlated, such that the uncertainty associated with their linear combination $\frac{1}{2}\Delta\Sigma + \Delta G$ entering the Jaffe-Manohar sum rule (1) is not as large as one may expect by simply adding the two uncertainties.

Using our results for $\Delta\Sigma(x,Q^2)$ and $\Delta G(x,Q^2)$ we can compute how much spin resides at small x (see Eq. (2)) along with the axial charges. In the left panel of Fig. 15, we plot the quantities

$$\left(\frac{1}{2}\Delta\Sigma + \Delta G\right)_{[x_{\rm max}]}(Q^2) \equiv \int_{10^{-5}}^{x_{\rm max}} {\rm d}x \left(\frac{1}{2}\Delta\Sigma + \Delta G\right)(x,Q^2), \tag{43a}$$

$$g_{A[x_{\max}]}(Q^2) \equiv \int_{10^{-5}}^{x_{\max}} \mathrm{d}x \, \left[\Delta u^+(x,Q^2) - \Delta d^+(x,Q^2)\right], \tag{43b}$$

$$a_{8[x_{\max}]}(Q^2) \equiv \int_{10^{-5}}^{x_{\max}} \mathrm{d}x \, \left[\Delta u^+(x,Q^2) + \Delta d^+(x,Q^2) - 2\,\Delta s^+(x,Q^2)\right], \tag{43c}$$

with the lower limit of $x = 10^{-5}$ picked as a suitable lower bound (smaller values will be explored in the future work). We find the following contributions to the proton spin from the quark and gluon spins in the unmeasured region, $10^{-5} < x < 10^{-3}$: $\Delta\Sigma^{[10^{-3}]}\left(Q^2 = 10\,\mathrm{GeV}^2\right) = 0.1 \pm 0.4$ and $\Delta G^{[10^{-3}]}\left(Q^2 = 10\,\mathrm{GeV}^2\right) = -0.1 \pm 0.6$. Even though there are sizable uncertainties, we conclude that the amount of the proton spin coming from small-x partons could be quite large. The outer bounds of these estimates also allow for the possibility that the quark and gluon spin contained within the small-x region may be even more significant than what has been computed at large x.

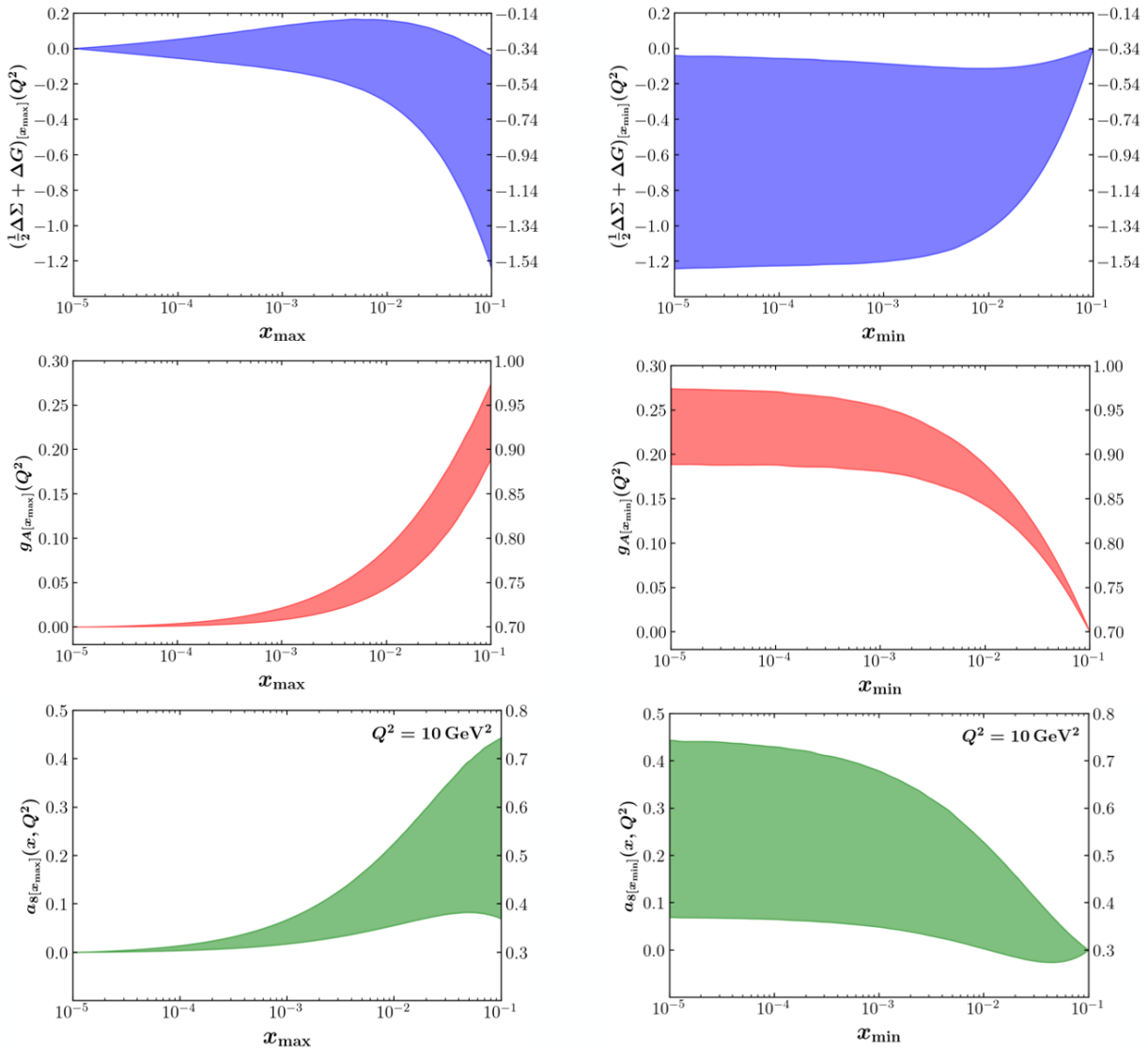

FIG. 15. Plots of the truncated moments $(\frac{1}{2}\Delta\Sigma + \Delta G)(Q^2)$, $g_A(Q^2)$, $a_8(Q^2)$ as functions of x_{max} (left) and x_{min} (right) defined in Eqs. 43 and 44, respectively. All results shown were computed for $Q^2 = 10$ GeV^2. On the right axis of each sub-figure we show what the quantity would be if we included the large-x truncated moment extracted from a DGLAP fit. Respectively, $\int_{0.1}^{1} \mathrm{d}x \left(\frac{1}{2}\Delta\Sigma + \Delta G\right)(x,Q^2) = -0.34$, $\int_{0.1}^{1} \mathrm{d}x\, g_A(x,Q^2) = 0.7$ and $\int_{0.1}^{1} \mathrm{d}x\, a_8(x,Q^2) = 0.3$.

Conversely, one can define more conventional quantities [33, 34, 55]

$$\left(\frac{1}{2}\Delta\Sigma+\Delta G\right)_{[x_{\rm min}]}(Q^2)\equiv\int\limits_{x_{\rm min}}^{x_0}\mathrm{d}x\,\left(\frac{1}{2}\Delta\Sigma+\Delta G\right)(x,Q^2)\,, \tag{44a}$$

$$g_{A[x_{\rm min}]}(Q^2)\equiv\int\limits_{x_{\rm min}}^{x_0}\mathrm{d}x\,\left[\Delta u^+(x,Q^2)-\Delta d^+(x,Q^2)\right], \tag{44b}$$

$$a_{8[x_{\rm min}]}(Q^2)\equiv\int\limits_{x_{\rm min}}^{x_0}\mathrm{d}x\,\left[\Delta u^+(x,Q^2)+\Delta d^+(x,Q^2)-2\,\Delta s^+(x,Q^2)\right], \tag{44c}$$

which are plotted in the right panel of Fig. 15 for our $x_0 = 0.1$. We see that our formalism predicts a negative contribution to the proton spin from the small-x parton helicities within 1σ. Note that, despite the wide error bands in ΔG and $\Delta\Sigma$, as shown in Figs. 13 and 14, the error band in the plot of $\left(\frac{1}{2}\Delta\Sigma+\Delta G\right)_{[x_{\rm max}]}$ in Fig. 15 is narrower than one might have expected if the two were uncorrelated. Both error bands for ΔG and $\Delta\Sigma$ are large and span zero, but as derived in (41) replicas with *negative* ΔG simultaneously possess *positive* $\Delta\Sigma$ (and vice versa). This leads to a cancellation between them, resulting in a total parton helicity contribution $\frac{1}{2}\Delta\Sigma+\Delta G$ which skews negative and is more tightly constrained than either $\Delta\Sigma$ or ΔG alone.

We also conclude from Fig. 15 that, while both $g_A(Q^2)$ and $a_8(Q^2)$ (integrated over all $x\in[0,1]$) are dominated by the large-x partons, the contributions of the small-x partons to these quantities appear to be numerically significant. We also note that this approach of simply adding our small-x truncated moments to the large-x contribution extracted from a DGLAP fit does not equate to the previously established values values of $a_8 = 0.58, 0.46$ [156**?**] and $g_A = 1.269$ [157] . We attribute this to a lack of proper matching between the small-x formalism and the large-x DGLAP extraction. A fully developed matching of our theory onto large-x will allow us to integrate fully up to $x = 1$ without the need of adding in a contribution from a separate formalism with its own caveats. A jumping-off point for such matching is explored in Section III E.

D. Impact of EIC data on g_1^p

In order to study the impact of lower x measurements on our ability to predict the behavior of g_1^p and the hPDFs at even smaller x, we utilized EIC pseudodata for the kinematic region of $10^{-4} < x < 10^{-1}$ and $1.69\ \mathrm{GeV}^2 < Q^2 < 50\ \mathrm{GeV}^2$. The EIC will be capable of going lower in x by reaching higher Q^2, but we do not expect our formalism to be applicable for arbitrarily large Q^2 (DGLAP resummation is needed to fully describe the Q^2 dependence). For DIS on the proton, the pseudodata was at center-of-mass energies $\sqrt{s} = \{29, 45, 63, 141\}$ GeV with integrated luminosity of $100\,\mathrm{fb}^{-1}$, while for the deuteron and ^{3}He beams the pseudodata spanned $\sqrt{s} = \{29, 66, 89\}$ GeV with $10\,\mathrm{fb}^{-1}$ integrated luminosity. These are consistent with the EIC detector design of the Yellow Report, including 2% point to-point uncorrelated systematic uncertainties [9]. For SIDIS on a proton, the pseudodata was at $\sqrt{s} = 141$ GeV, also with a 2% systematic uncertainty [158] (citation might be updated when Charlottes's paper is done). In our earlier work [97], we had relied on parity violating DIS pseudodata in order to disentangle the three light quark (flavor singlet) hPDFs. With the inclusion of SIDIS data, that is no longer necessary. The EIC could provide such data [9], and it would serve as an additional constraint in the future, but we do not consider its impact in the present analysis.

Our current extrapolation of g_1^p covers a wide range of possibilities at small x, so we generate the pseudodata based on three scenarios for g_1^p that are consistent with present data: (1) the mean of the asymptotically positive replicas ("high g_1"), (2) the mean of the asymptotically negative replicas ("low g_1") and (3) the mean of a fit where g_1^p was constrained to have $|g_1^p| < 100$ at $x = 10^{-4}$ ("mid g_1"). These three options have qualitatively distinct behavior and comparing them should inform us if the impact of the EIC is dependent on the precise small-x asymptotics of g_1^p. The results are shown in Fig. 16. We find a dramatic decrease in uncertainties for all three scenarios, even in the extrapolated region of $x < 10^{-4}$. In Fig. 17 we plot the relative uncertainty of g_1^p compared to that of a JAM DGLAP-based extraction using EIC pseudodata [159]. The results confirm the observation above that, when using the genuine predictability of the small-x helicity evolution, control over uncertainties is maintained as we extrapolate to smaller x. In contrast, since the DGLAP-based fit must use an ad-hoc parameterization of the x dependence, it cannot maintain control over the uncertainties into the extrapolation region.

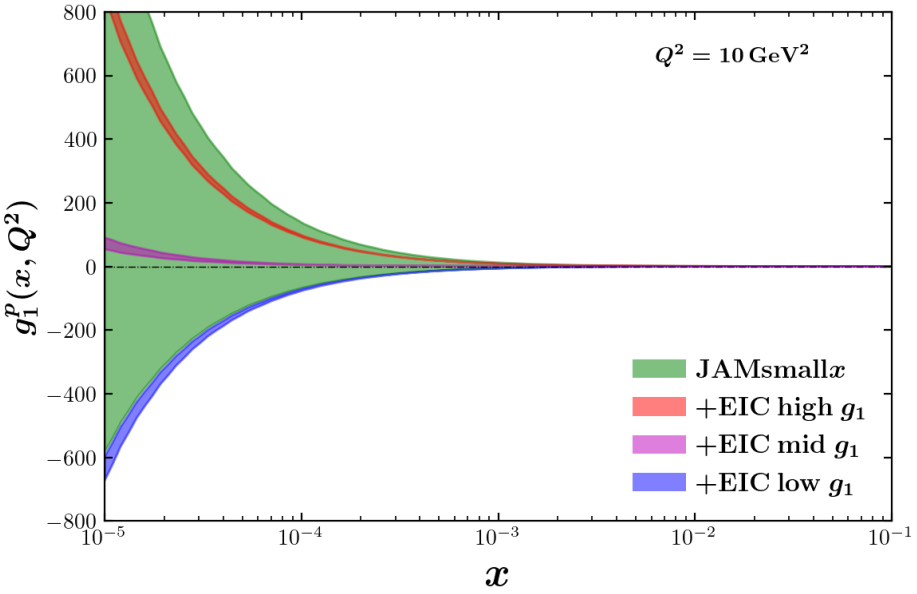

FIG. 16. Extraction of g_1^p from the current low-x experimental data (green, same as Fig. 5) and with EIC pseudodata generated from the mean of the asymptotically positive g_1^p replicas (red), mean of the asymptotically negative g_1^p replicas (blue), and mean of replicas restricted such that $|g_1^p| < 100$ at $x = 10^{-4}$ (magenta).

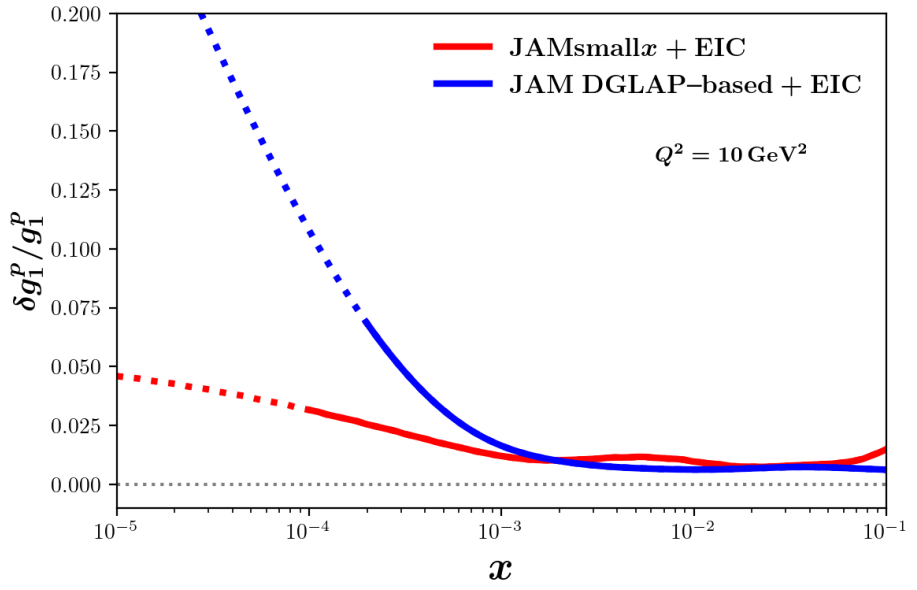

FIG. 17. Relative uncertainty for both this work (red) and a JAM DGLAP-based extraction [159] (blue) for EIC impact studies using the high g_1^p scenario. Dotted lines denote extrapolating beyond lowest x for which pseudodata was generated. For this work, pseudodata was generated down to $x = 10^{-4}$. For the JAM DGLAP-based fit, pseudodata was generated down to $x = 2 \times 10^{-4}$ [159].

E. Imposing additional constraints

While future data from the EIC is a promising way to resolve the issue of sizeable uncertainties in our extracted hPDFs at small-x, it is worth considering other options that might be more immediately accessible. Ideally these constraints would enter in the form of existing data or as theoretical constraints on the initial conditions.

The hPDF with largest uncertainty that we have extracted is $\Delta G(x,Q^2)$, as demonstrated in Fig. 13, so we explored a few options to constrain it. The first such constraint is the positivity constraint, which is the statement that the number densities for positive and negative helicity partons are positive. In particular, for gluons this leads to

$$|\Delta G(x,Q^2)| < G(x,Q^2)\,, \tag{45}$$

where $G(x,Q^2)$ is the unpolarized gluon PDF. (We will set aside issues as to whether Eq. (45) is strictly satisfied under ($\overline{\rm MS}$) renormalization [160].) We imposed this constraint by checking the value of $\Delta G(x,Q^2)$ in the region we trust our evolution, $x < x_0 = 0.1$, and punishing the χ^2 of the fit if the positivity constraint is violated. Unfortunately, by the time our evolution begins, our baseline fit for $\Delta G(x,Q^2)$ and the JAM DGLAP-based $G(x,Q^2)$ [34] are of comparable size. The latter grows much faster at small x than our extraction for $\Delta G(x,Q^2)$, causing the positivity constraint to have a negligible effect. This is perhaps not surprising, given that at small x the unpolarized gluon distribution $G(x,Q^2)$ is eikonal, while ΔG is sub-eikonal, and, hence, suppressed by a power of x.

Another constraint on $\Delta G(x,Q^2)$ that we explored was a preliminary matching onto the (large-x) JAM DGLAP-based extraction of $\Delta G(x,Q^2)$ in Refs. [33, 34]. In particular, we used their SU(3)+positivity scenario. The result is shown in Fig. 18; the red box is bounded by $10^{-1.3} < x < 10^{-1}$ and $0.05 < \Delta G < 0.2$. The motivation is that any complete description of $\Delta G(x,Q^2)$ should agree with DGLAP extractions in this region. The matching is performed in a simple way, by choosing an intermediate region in x and forcing our fit of $\Delta G(x,Q^2)$ to qualitatively agree with the JAM DGLAP-based extraction. This is done in a similar way to the positivity constraint described above, whereby we punish the χ^2 whenever $\Delta G(x,Q^2)$ strays outside of the matching region (red rectangle in Fig. 18). This constraint causes our extracted $\Delta G(x,Q^2)$ to take on mostly positive values at small x, seemingly changing sign from our original extraction. However, note that while the baseline extraction *uncertainty band* grows negative for large x, there are still a significant number of replicas (with good χ^2) that grow positive at large x and overlap with the red region. Forcing $\Delta G(x,Q^2)$ to pass through that area then preferentially selects those replicas. Consequently, the whole uncertainty band for $\Delta G(x,Q^2)$ remains shifted upward even in the small-x region. Given that $g_1^p(x,Q^2) \propto -\Delta G(x,Q^2)$ (41), the matching constraint leads to a quantitative change to the distribution of g_1^p replicas: they are now 40% positive and 60% negative. This demonstrates that input on hPDFs from large x can have a significant effect on the predictions made at small x, motivating future work into a more rigorous matching to DGLAP-based hPDF fits.

A more rigorous way of handling the starting point of evolution, x_0, could alleviate the trouble with constraining $\widetilde{G}$. In this we work, we use $x_0 \equiv 0.1$ as a starting point for our evolution and then use experimental data to fit initial conditions in order to obtain the correct starting values for all of the extracted distributions. Only after these starting values have been determined do we then evolve the distributions in a region dominated by our double logarithmic resummation. In reality, evolution in x begins at $x = 1$, but is sub-leading, with the dominant contribution to the structure functions and distributions of interest at large x given by DGLAP-driven large-x dynamics. The method of matched asymptotic expansions [161, 162] suggests that we start the evolution at $x_0 = 1$, include the DGLAP contributions, but subtract the double counting of logs that are present in both resummations. By starting evolution earlier, $\widetilde{G}$ might become more sensitive to the data. As discussed at the end of Sec. II E, the challenge in constraining $\widetilde{G}$ stems from the fact that it has a small magnitude in the region where there are measurements (see Fig. 1). Part of the reason the magnitude of the $\widetilde{G}$ contribution to Δu^+ is so small there is that $\widetilde{G}$ enters only through evolution, and evolution is delayed until $x_0 = 0.1$. If $x_0 = 1$, $\widetilde{G}$ will start growing sooner and it might then have a large enough contribution to be sensitive to the experimental data.

Lastly, perhaps the most direct way to constrain $\Delta G(x,Q^2)$ is to include in the analysis an observable directly sensitive to it. (Recall that in the polarized DIS and SIDIS processes considered here the contribution from the gluon hPDF is suppressed by a factor of α_s. Two possibilities to introduce ΔG sensitive data are jet and hadron production in polarized proton-proton collisions. The numerator of the double-longitudinal spin asymmetry A_{LL} takes the following form [163]

$$\sigma^{\downarrow\Uparrow} - \sigma^{\uparrow\Uparrow} = \sum_{a,b} \Delta f_{a/A} \otimes f_{b/B} \otimes \sigma_{ab}, \tag{46}$$

where Δf is the parton hPDF for either the quarks or gluon, $a(b)$ is the parton coming from proton $A(B)$, and σ_{ab} is the partonic cross section of parton a interacting with parton b. For hadron production, Eq. (46) needs also to be convoluted with the fragmentation functions. Equation (46) connects the double-spin asymmetry A_{LL} in $\vec{p}+\vec{p}$ collisions to all hPDFs, including ΔG, allowing for the extraction of the latter from data [23, 26, 27, 33, 34]. More work is needed to derive an analogue of Eq. (46) in the small-x evolution framework of KPS-CTT, and initial developments can be found in Ref. [92].

In the future, it will also be interesting to attempt to constrain the large-x behavior of the hPDFs by direct matching onto nonperturbative calculations from lattice QCD. Such matching in the vicinity of $x \sim 0.1$ is actually feasible for

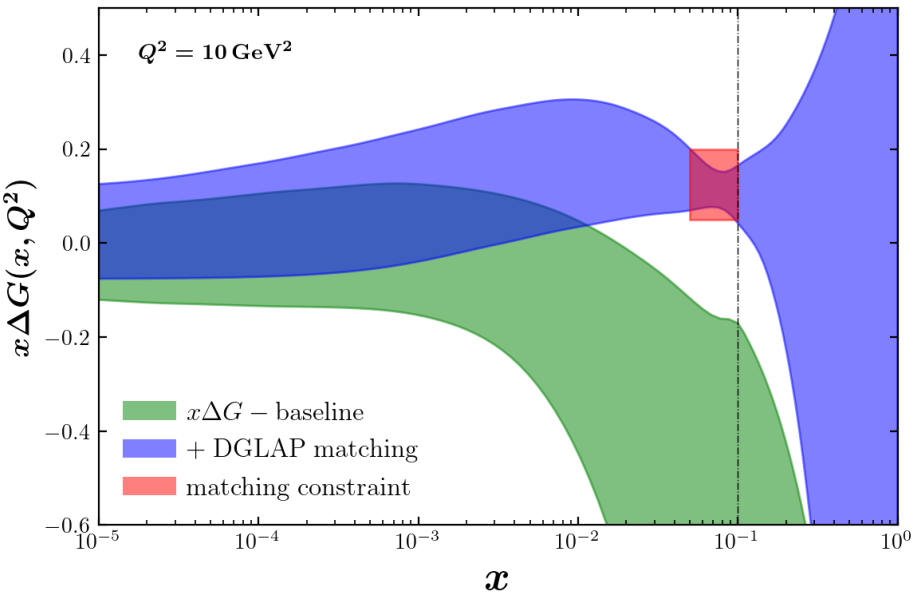

FIG. 18. The result of matching onto the $\Delta G(x)$ extraction from DGLAP [33, 34] at intermediate x. The green band is our baseline fit. The blue band is the result of matching. The light red square is the region where we enforce matching.

the double-logarithmic helicity evolution, unlike for the case of single-logarithmic unpolarized small-x evolution which would require reliable lattice data down to much smaller x.

Recently a new approach to determining the initial conditions for small-x evolution by starting at the level of the proton wave function has been developed in [164]. While that work was done in the context of unpolarized small-x evolution, it is possible that it could be extended to the polarized case, helping us constrain the initial conditions for helicity evolution at hand.

IV. CONCLUSIONS

In this paper we have presented the first phenomenological implementation of the KPS-CTT theoretical framework [52, 58, 65] for the evolution of helicity parton distribution functions. This work represents a significant improvement over our previous study [97] by utilizing the revised evolution equations instead of the original KPS equations. On top of that, we have adopted the large-N_c&N_f limit, enabling a more realistic description of the physics, now including quarks in addition to gluons. Another key advancement of this research is an expansion of our analysis beyond just polarized DIS data by also incorporating polarized semi-inclusive DIS measurements. This allowed us to extract both the flavor singlet and nonsinglet hPDFs, which for the latter was the first implementation of the numeric solution for the KPS evolution of the nonsinglet hPDFs. Moreover, we have included running coupling corrections in the evolution of both flavor singlet and nonsinglet hPDFs, which is another feature of the analysis that makes our approach more rigorous.

Through the application of the JAM Bayesian Monte Carlo framework, we have successfully described all available polarized DIS and SIDIS data below the threshold $x_0 = 0.1$, achieving a very good fit with $\chi^2/N_{\rm pts} = 1.03$. However, when attempting to extend our predictions to lower values of x, the uncertainty associated with our results was found to be substantial. This large uncertainty arises from the inherent insensitivity of the data to the polarized dipole amplitudes G_2 and $\widetilde{G}$. To address this challenge, we discussed several potential future improvements, among which investigating jet or hadron production in longitudinally polarized proton-proton collisions emerges as a promising medium-term solution. However, more theoretical developments are desirable in the short term, where one must identify the observables which can be expressed in terms of the polarized dipole amplitudes G_2 and $\widetilde{G}$.

Another issue which needs to be clarified in the medium term is the impact of the axial anomaly on the g_1 structure function and hPDFs at small x. The role of the axial anomaly in the polarized structure functions, originally pointed out in Refs. [10, 165, 166], has been recently revisited in Refs. [167–170]. The effect appears to be distinct from the DLA of BER and KPS-CTT evolution. Developing the corresponding phenomenology is left for future work.

Based on current experimental data, we find that there could be significant spin coming from small-x partons, but there are large uncertainties in our estimates. Consequently, looking towards the long term, our extensive impact studies conducted for the EIC demonstrate its potential to significantly reduce uncertainties in the hPDFs and the calculation of the contribution to the proton spin from the quark and gluon spins. The inclusion of EIC data would enable more precise statements about the distribution of (spin and orbital) angular momentum within the proton.

ACKNOWLEDGMENTS

We thank Yiyu Zhou and Chris Cocuzza for providing us replicas and calculations for the JAM DGLAP-based analyses. This work has been supported by the U.S. Department of Energy, Office of Science, Office of Nuclear Physics under Award Number DE-SC0004286 (DA and YK), No. DE-SC0020081 (AT), No. DE-AC05-06OR23177 (DA, WM and NS) under which Jefferson Science Associates, LLC, manages and operates Jefferson Lab, and the National Science Foundation under Grants No. PHY-2011763 and No. PHY-2308567 (DP). The work of NS was supported by the DOE, Office of Science, Office of Nuclear Physics in the Early Career Program. This work is also supported by the U.S. Department of Energy, Office of Science, Office of Nuclear Physics, within the framework of the Saturated Glue (SURGE) Topical Theory Collaboration. The work of YT has been supported by the Academy of Finland, by the Centre of Excellence in Quark Matter and project 321840, and under the European Union's Horizon 2020 research and innovation programme by the STRONG-2020 project (grant agreement No 824093) and by the European Research Council, grant agreement ERC-2015-CoG-681707. The content of this article does not reflect the official opinion of the European Union and responsibility for the information and views expressed therein lies entirely with the authors.

Appendix A: Discretization of the flavor singlet and nonsinglet evolution equations

In this Appendix we present the process of discretizing Eqs. (9) and (13) in order to perform their numerical solutions. In addition, we implement the starting point of our evolution at $x = x_0$.

We start with the flavor singlet case. Imposing the $\eta - s_{10} > y_0$, $\eta' - s_{21} > y_0$, $\eta'' - s_{32} > y_0$ constraints, we re-write Eqs. (9) in terms of the variables (15) as

$$\begin{aligned} Q_q(s_{10},\eta) &= Q_q^{(0)}(s_{10},\eta) + \int_{s_{10}+y_0}^{\eta} \mathrm{d}\eta' \int_{s_{10}}^{\eta'-y_0} \mathrm{d}s_{21}\,\alpha_s(s_{21}) \Big[Q_q(s_{21},\eta') + 2\widetilde{G}(s_{21},\eta') + 2\widetilde{\Gamma}(s_{10},s_{21},\eta') \\ &\quad - \overline{\Gamma}_q(s_{10},s_{21},\eta') + 2G_2(s_{21},\eta') + 2\Gamma_2(s_{10},s_{21},\eta') \Big] \\ &\quad + \frac{1}{2} \int_{y_0}^{\eta} \mathrm{d}\eta' \int_{\max[0,s_{10}+\eta'-\eta]}^{\eta'-y_0} \mathrm{d}s_{21}\,\alpha_s(s_{21}) \Big[Q_q(s_{21},\eta') + 2G_2(s_{21},\eta') \Big], \end{aligned} \tag{A1a}$$

$$\begin{aligned} \overline{\Gamma}_q(s_{10},s_{21},\eta') &= Q_q^{(0)}(s_{10},\eta') + \int_{s_{10}+y_0}^{\eta'} \mathrm{d}\eta'' \int_{\max[s_{10},s_{21}-\eta'+\eta'']}^{\eta''-y_0} \mathrm{d}s_{32}\,\alpha_s(s_{32}) \Big[Q_q(s_{32},\eta'') + 2\widetilde{G}(s_{32},\eta'') \\ &\quad + 2\,\widetilde{\Gamma}(s_{10},s_{32},\eta'') - \overline{\Gamma}_q(s_{10},s_{32},\eta'') + 2G_2(s_{32},\eta'') + 2\Gamma_2(s_{10},s_{32},\eta'') \Big] \\ &\quad + \frac{1}{2} \int_{y_0}^{\eta'} \mathrm{d}\eta'' \int_{\max[0,s_{21}+\eta''-\eta']}^{\eta''-y_0} \mathrm{d}s_{32}\,\alpha_s(s_{32}) \Big[Q_q(s_{32},\eta'') + 2G_2(s_{32},\eta'') \Big], \end{aligned} \tag{A1b}$$

$$\begin{aligned} \widetilde{G}(s_{10},\eta) &= \widetilde{G}^{(0)}(s_{10},\eta) + \int_{s_{10}+y_0}^{\eta} \mathrm{d}\eta' \int_{s_{10}}^{\eta'-y_0} \mathrm{d}s_{21}\,\alpha_s(s_{21}) \Big[3\widetilde{G}(s_{21},\eta') + \widetilde{\Gamma}(s_{10},s_{21},\eta') \\ &\quad + 2G_2(s_{21},\eta') + \big(2 - \frac{N_f}{2N_c}\big)\Gamma_2(s_{10},s_{21},\eta') - \frac{1}{4N_c} \sum_q \overline{\Gamma}_q(s_{10},s_{21},\eta') \Big] \\ &\quad - \frac{1}{4N_c} \int_{y_0}^{\eta} \mathrm{d}\eta' \int_{\max[0,s_{10}+\eta'-\eta]}^{\min[s_{10},\eta'-y_0]} \mathrm{d}s_{21}\,\alpha_s(s_{21}) \Big[\sum_q Q_q(s_{21},\eta') + 2N_f G_2(s_{21},\eta') \Big], \end{aligned} \tag{A1c}$$

$$\widetilde{\Gamma}(s_{10},s_{21},\eta') = \widetilde{G}^{(0)}(s_{10},\eta') + \int_{s_{10}+y_0}^{\eta'} \mathrm{d}\eta'' \int_{\max[s_{10},s_{21}-\eta'+\eta'']}^{\eta''-y_0} \mathrm{d}s_{32}\,\alpha_s(s_{32}) \Big[3\widetilde{G}(s_{32},\eta'') + \widetilde{\Gamma}(s_{10},s_{32},\eta'') \tag{A1d}$$

$$+ 2G_2(s_{32},\eta'') + \big(2 - \frac{N_f}{2N_c}\big)\Gamma_2(s_{10},s_{32},\eta'') - \frac{1}{4N_c}\sum_q \overline{\Gamma}_q(s_{10},s_{32},\eta'')\Big]$$

$$- \frac{1}{4N_c}\int_{y_0}^{\eta'+s_{10}-s_{21}} \mathrm{d}\eta'' \int_{\max[0,s_{21}+\eta''-\eta']}^{\min[s_{10},\eta''-y_0]} \mathrm{d}s_{32}\,\alpha_s(s_{32})\Big[\sum_q Q_q(s_{32},\eta'') + 2N_f G_2(s_{32},\eta'')\Big],$$

$$G_2(s_{10},\eta) = G_2^{(0)}(s_{10},\eta) + 2\int_{y_0}^{\eta}\mathrm{d}\eta' \int_{\max[0,s_{10}+\eta'-\eta]}^{\min[s_{10},\eta'-y_0]} \mathrm{d}s_{21}\,\alpha_s(s_{21})\Big[\widetilde{G}(s_{21},\eta') + 2G_2(s_{21},\eta')\Big], \tag{A1e}$$

$$\Gamma_2(s_{10},s_{21},\eta') = G_2^{(0)}(s_{10},\eta') + 2\int_{y_0}^{\eta'+s_{10}-s_{21}}\mathrm{d}\eta'' \int_{\max[0,s_{21}+\eta''-\eta']}^{\min[s_{10},\eta''-y_0]} \mathrm{d}s_{32}\,\alpha_s(s_{32})\Big[\widetilde{G}(s_{32},\eta'') + 2G_2(s_{32},\eta'')\Big]. \tag{A1f}$$

Following Refs. [61, 65, 96], the evolution equations (A1) can be iterated more optimally by considering the recursive form of their Riemann sums. To do so, we begin by writing Eqs. (A1a), (A1c) and (A1e) as the first-order Taylor expansions in η, *e.g.*,

$$Q_q(s_{10},\eta+\Delta) = Q_q(s_{10},\eta) + \Delta\,\frac{\partial}{\partial\eta}Q_q(s_{10},\eta) + \mathcal{O}(\Delta^2)\,, \tag{A2}$$

and Eqs. (A1b), (A1d) and (A1f) as the first-order Taylor expansions in η' and s_{21}, e.g,.

$$\overline{\Gamma}_q(s_{10},s_{21}+\Delta,\eta'+\Delta) = \overline{\Gamma}_q(s_{10},s_{21},\eta') + \Delta\,\frac{\partial}{\partial\eta'}\overline{\Gamma}_q(s_{10},s_{21},\eta') + \Delta\,\frac{\partial}{\partial s_{21}}\overline{\Gamma}_q(s_{10},s_{21},\eta') + \mathcal{O}(\Delta^2)\,. \tag{A3}$$

The expansions for other (neighbor) dipole amplitudes are similar. Note that the transverse sizes in neighbor dipoles are always ordered such that $x_{32} < x_{21} < x_{10}$, which implies that $s_{32} > s_{21} > s_{10}$. Neglecting order-Δ^2 terms for small step sizes $\Delta \ll 1$, Eqs. (A1) can be written as

$$\begin{aligned} Q_q(s_{10},\eta+\Delta) &= Q_q(s_{10},\eta) + Q_q^{(0)}(s_{10},\eta+\Delta) - Q_q^{(0)}(s_{10},\eta) \\ &+ \Delta\int_{s_{10}}^{\eta-y_0}\mathrm{d}s_{21}\,\alpha_s(s_{21})\Big[\frac{3}{2}Q_q(s_{21},\eta) + 2\widetilde{G}(s_{21},\eta) + 2\widetilde{\Gamma}(s_{10},s_{21},\eta) \\ &\quad - \overline{\Gamma}_q(s_{10},s_{21},\eta) + 3G_2(s_{21},\eta) + 2\Gamma_2(s_{10},s_{21},\eta)\Big] \\ &+ \frac{1}{2}\Delta\int_{\eta-s_{10}}^{\eta}\mathrm{d}\eta'\,\alpha_s(s_{10}+\eta'-\eta)\Big[Q_q(s_{10}+\eta'-\eta,\eta') + 2G_2(s_{10}+\eta'-\eta,\eta')\Big]\,, \end{aligned} \tag{A4a}$$

$$\begin{aligned} \overline{\Gamma}_q(s_{10},s_{21}+\Delta,\eta'+\Delta) &= Q_q(s_{10},\eta) + Q_q^{(0)}(s_{10},\eta+\Delta) - Q_q^{(0)}(s_{10},\eta) \\ &+ \Delta\int_{s_{21}}^{\eta'-y_0}\mathrm{d}s_{32}\,\alpha_s(s_{32})\Big[\frac{3}{2}Q_q(s_{32},\eta') + 2\widetilde{G}(s_{32},\eta') \\ &\quad + 2\,\widetilde{\Gamma}(s_{10},s_{32},\eta') - \overline{\Gamma}_q(s_{10},s_{32},\eta') + 3G_2(s_{32},\eta') + 2\Gamma_2(s_{10},s_{32},\eta')\Big]\,, \end{aligned} \tag{A4b}$$

$$\begin{aligned} \widetilde{G}(s_{10},\eta+\Delta) &= \widetilde{G}(s_{10},\eta) + \widetilde{G}^{(0)}(s_{10},\eta+\Delta) - \widetilde{G}^{(0)}(s_{10},\eta) \\ &+ \Delta\int_{s_{10}}^{\eta-y_0}\mathrm{d}s_{21}\,\alpha_s(s_{21})\Big[3\widetilde{G}[i',j-1] + \widetilde{\Gamma}(s_{10},s_{21},\eta) \\ &\quad + 2G_2(s_{21},\eta) + \big(2-\frac{N_f}{2N_c}\big)\Gamma_2(s_{10},s_{21},\eta) - \frac{1}{4N_c}\sum_q\overline{\Gamma}_q(s_{10},s_{21},\eta)\Big] \\ &- \Delta\frac{1}{4N_c}\int_{\eta-s_{10}}^{\eta}\mathrm{d}\eta'\,\alpha_s(s_{10}+\eta'-\eta)\Big[\sum_q Q_q(s_{10}+\eta'-\eta,\eta') + 2N_f G_2(s_{10}+\eta'-\eta,\eta')\Big]\,, \end{aligned} \tag{A4c}$$

$$\begin{aligned} \widetilde{\Gamma}(s_{10},s_{21}+\Delta,\eta'+\Delta) &= \widetilde{\Gamma}(s_{10},s_{21},\eta') + \widetilde{G}^{(0)}(s_{10},\eta'+\Delta) - \widetilde{G}^{(0)}(s_{10},\eta') \\ &+ \Delta\int_{s_{21}}^{\eta'-y_0}\mathrm{d}s_{32}\,\alpha_s(s_{32})\Big[3\widetilde{G}(s_{32},\eta') + \widetilde{\Gamma}(s_{10},s_{32},\eta') \\ &\quad + 2G_2(s_{32},\eta') + \big(2-\frac{N_f}{2N_c}\big)\Gamma_2(s_{10},s_{32},\eta') - \frac{1}{4N_c}\sum_q\overline{\Gamma}_q(s_{10},s_{32},\eta')\Big]\,, \end{aligned} \tag{A4d}$$

$$G_2(s_{10},\eta+\Delta) = G_2(s_{10},\eta) + G_2^{(0)}(s_{10},\eta+\Delta) - G_2^{(0)}(s_{10},\eta) \tag{A4e}$$

$$+ 2\Delta \int_{\eta - s_{10}}^{\eta} \mathrm{d}\eta'\, \alpha_s(s_{10} + \eta' - \eta) \Big[\widetilde{G}(s_{10} + \eta' - \eta, \eta') + 2G_2(s_{10} + \eta' - \eta, \eta') \Big] ,$$

$$\Gamma_2(s_{10}, s_{21} + \Delta, \eta' + \Delta) = \Gamma_2(s_{10}, s_{21}, \eta') + G_2^{(0)}(s_{10}, \eta' + \Delta) - G_2^{(0)}(s_{10}, \eta') . \tag{A4f}$$

Next we discretize the remaining integrals via a left-hand Riemann sum in order to be able to iteratively compute the amplitudes at higher rapidities η, which are required for the calculation of hPDFs and the g_1 structure function at small x. This step is most conveniently performed once we make the change of variables, $\{\eta, s_{10}, s_{21}\} \to \{i, j, k\} \cdot \Delta$. At the end, Eqs. (A4) reduce to the discretized Eqs. (17) in the main text.

The numerical implementation of the flavor nonsinglet evolution equation (13) parallels that of the flavor singlet evolution considered above. We use the variable change from Eqs. (15) and also require that the flavor nonsinglet evolution starts at $x = x_0$, such that $\eta - s_{10} \approx \sqrt{\frac{N_c}{2\pi}} \ln \frac{1}{x} > \sqrt{\frac{N_c}{2\pi}} \ln \frac{1}{x_0} \equiv y_0$. Implementing these modifications in Eq. (13) gives us the following evolution for G^{NS},

$$G^{\mathrm{NS}}(s_{10}, \eta) = G^{\mathrm{NS}\,(0)}(s_{10}, \eta) + \frac{1}{2} \int_{y_0}^{\eta} \mathrm{d}\eta' \int_{\max[0, s_{10} - \eta + \eta']}^{\eta' - y_0} \mathrm{d}s_{21}\, \alpha_s(s_{21})\, G^{\mathrm{NS}}(s_{21}, \eta') . \tag{A5}$$

Discretizing the nonsinglet evolution is mostly similar to that of the singlet evolution. First, we produce a recursion relation using the first order Taylor expansion, simplify it, and discretize it using the left-handed Riemann sum. Differentiating Eq. (A5) yields

$$\begin{aligned} \frac{\partial}{\partial \eta} G^{\mathrm{NS}}(s_{10}, \eta) = \frac{\partial}{\partial \eta} G^{\mathrm{NS}\,(0)}(s_{10}, \eta) + \frac{1}{2} \int_{s_{10}}^{\eta - y_0} \mathrm{d}s_{21}\ \alpha_s(s_{21})\, G^{\mathrm{NS}}(s_{21}, \eta) \\ + \frac{1}{2} \int_{\eta - s_{10}}^{\eta} \mathrm{d}\eta'\ \alpha_s(s_{10} - \eta + \eta') G^{\mathrm{NS}}(s_{10} - \eta + \eta', \eta') , \end{aligned} \tag{A6}$$

where we have also employed the $s_{10} > 0$, $\eta - s_{10} > y_0$ conditions. Using the Taylor expansion in η, c.f. Eq. (A2), we obtain a recursive form of our flavor nonsinglet evolution

$$\begin{aligned} G^{\mathrm{NS}}(s_{10}, \eta) = G^{\mathrm{NS}}(s_{10}, \eta - \Delta\eta) + G^{\mathrm{NS}\,(0)}(s_{10}, \eta) - G^{\mathrm{NS}\,(0)}(s_{10}, \eta - \Delta\eta) \\ + \frac{1}{2}\Delta\eta \int_{s_{10}}^{\eta - y_0} \mathrm{d}s_{21}\ \alpha_s(s_{21})\, G^{\mathrm{NS}}(s_{21}, \eta) + \frac{1}{2}\Delta\eta \int_{\eta - s_{10}}^{\eta} \mathrm{d}\eta'\ \alpha_s(s_{10} - \eta + \eta')\, G^{\mathrm{NS}}(s_{10} - \eta + \eta', \eta') . \end{aligned} \tag{A7}$$

In order to have a numerical solution consistent with the flavor singlet numerical evolution, we again define $\Delta\eta = \Delta s \equiv \Delta$. We also index our numerics in the same way as in the flavor singlet case, $\{\eta, \eta', s_{10}, s_{21}\} \to \{i, i', j, j'\}$. Ultimately, Eq. (A7) yields the discretized Eq. (23) in the main text.

Appendix B: Analytic cross-check of the numerical solution for the flavor nonsinglet evolution

Finding an analytic solution for the large-N_c flavor nonsinglet evolution equation that enforces all of our physical assumptions *and* includes running coupling is, unfortunately, outside the scope of this paper. However, an analytic solution does exist for the large-N_c evolution equations with *fixed* coupling [54], which ignores the $1/\Lambda$ IR cutoff on the transverse size of the dipoles. We can perform a limited cross-check by modifying our numerical solution to use a fixed coupling $\alpha_s = 0.3$, and expand our domain of s_{10} by removing the IR dipole size cutoff, $x_{21} < 1/\Lambda$, employed in Eq. (13). Since the dipole size constraint is enforced by the relation $s_{10} > 0$, we refer to the analytic cross-check regime as the all-s_{10} ($\pm s$) regime.

The revised evolution equation becomes (c.f. Eq. (A5))

$$G^{\mathrm{NS}}_{\pm s}(s_{10}, \eta) = G^{\mathrm{NS}\,(0)}_{\pm s}(s_{10}, \eta) + \frac{\alpha_s}{2} \int_{0}^{\eta} \mathrm{d}\eta' \int_{s_{10} - \eta + \eta'}^{\eta' - y_0} \mathrm{d}s_{21}\, G^{\mathrm{NS}}_{\pm s}(s_{21}, \eta'), \tag{B1}$$

where relaxing the $s_{ij} > 0$ constraint has extended the lower limits of the η' and s_{21} integrals. As expected, changing the phase space of the evolution equation had an effect on our numerical solution, with the discretized flavor nonsinglet equation now being

$$G^{\rm NS}_{\pm s}[i,j] = G^{\rm NS}_{\pm s}[i,j-1] + G^{\rm NS\,(0)}_{\pm s}[i,j] - G^{\rm NS\,(0)}_{\pm s}[i,j-1] + \frac{\alpha_s}{2}\Delta^2\left[\sum_{i'=i}^{j-2-y_0} G^{\rm NS}_{\pm s}[i',j-1] + \sum_{j'=0}^{j-2} G^{\rm NS}_{\pm s}[i-j+1+j',j']\right], \tag{B2}$$

where the notable modifications compared to (23) are the factoring out of the fixed coupling α_s in front of the sum and the different starting point $j' = 0$ of the summation.

We can solve the all-s_{10} evolution equation analytically using Laplace-Mellin transforms (c.f. [54]). To enforce the small-x assumption on our conjugate variables, we define the forward and inverse transforms

$$G^{\rm NS}_{\pm s}(s_{10},\eta) = \int \frac{{\rm d}\omega}{2\pi i} e^{\omega\eta} \int \frac{{\rm d}\lambda}{2\pi i} e^{(\eta - s_{10} - y_0)\lambda} G^{\rm NS}_{\pm s}(\omega,\lambda), \tag{B3a}$$

$$G^{\rm NS}_{\pm s}(\omega,\lambda)\,, = \int_0^\infty d(\eta - s_{10} - y_0) e^{-\lambda(\eta - s_{10} - y_0)} \int_0^\infty {\rm d}\eta\, e^{-\omega\eta} G^{\rm NS}_{\pm s}(s_{10},\eta)\,. \tag{B3b}$$

In Mellin space, the solution presents itself just as it did in Ref. [54],

$$G^{\rm NS}_{\pm s}(\omega,\lambda) = \frac{\omega\lambda}{\lambda - \frac{\alpha_s}{2\omega}} \frac{1}{\omega} G^{\rm NS\,(0)}_{\pm s}(\omega,\lambda)\,. \tag{B4}$$

This is convenient since we only have 3 distinct initial conditions, $G^{\rm NS\,(0)}_{\pm s} = \eta,\, s_{10},\, 1$. First, we will evaluate the nonsinglet evolution beginning with the constant contribution, $G^{\rm NS\,(0)}_{\pm s}(\eta, s_{10}) = 1$.

$$G^{\rm NS\,(0)}_{\pm s}(\omega,\lambda) = \int_0^\infty d(\eta - s_{10} - y_0)\, e^{-\lambda(\eta - s_{10} - y_0)} \int_0^\infty {\rm d}\eta\, e^{-\omega\eta} = \frac{1}{\omega\lambda} \tag{B5}$$

Plugging this into the evolution equation leads to another contour integral with a pole at $\lambda = \alpha/(2\omega)$, which is evaluated via the residue theorem to give

$$G^{\rm NS}_{\pm s}(\eta, s_{10}) = \int \frac{{\rm d}\omega}{2\pi i}\, e^{\omega\eta} \int \frac{{\rm d}\lambda}{2\pi i}\, e^{(\eta - s_{10} - y_0)\lambda} \frac{1}{\lambda - \frac{\alpha_s}{2\omega}} \frac{1}{\omega} = \int \frac{{\rm d}\omega}{2\pi i} e^{\omega\eta + \frac{\alpha_s}{2\omega}(\eta - s_{10} - y_0)} \frac{1}{\omega}\,. \tag{B6}$$

Now we can Taylor-expand the singular ($\sim 1/\omega$) part of the exponential, use the residue theorem, and simplify the result, obtaining

$$G^{\rm NS}_{\pm s}(\eta, s_{10}) = \int \frac{{\rm d}\omega}{2\pi i} e^{\omega\eta} \sum_{n=0}^\infty \frac{1}{n!} \left(\frac{\alpha_s(\eta - s_{10} - y_0)}{2\omega}\right)^n \frac{1}{\omega} = \sum_{n=0}^\infty \frac{1}{(n!)^2} \left(\frac{\alpha_s}{2}\eta(\eta - s_{10} - y_0)\right)^n\,. \tag{B7}$$

This infinite sum is equivalent to the modified Bessel function of the first kind, $I_m(z)$ at $m = 0$,

$$G^{NS,\,1}_{\pm s}(\eta, s_{10}) = I_0\big(\sqrt{\alpha_s}\sqrt{2\eta(\eta - s_{10} - y_0)}\big). \tag{B8}$$

This process is repeated for the η initial condition, $G^{\rm NS\,(0)}_{\pm s}(\eta, s_{10}) = \eta$, giving

$$G^{\rm NS\,(0)}_{\pm s}(\omega,\lambda) = \int_0^\infty d(\eta - s_{10} - y_0)\, e^{-\lambda(\eta - s_{10} - y_0)} \int_0^\infty {\rm d}\eta\, e^{-\omega\eta}\eta = \frac{1}{\omega^2\lambda}\,. \tag{B9}$$

This contour integral has the same pole at $\lambda = \alpha_s/(2\omega)$, resulting in a similar integral,

$$G^{\rm NS}_{\pm s}(\eta, s_{10}) = \int \frac{{\rm d}\omega}{2\pi i} e^{\omega\eta + \frac{\alpha}{2\omega}(\eta - s_{10} - y_0)} \frac{1}{\omega^2}\,. \tag{B10}$$

We use the same Taylor expansion and the above expression for the ω contour integral to obtain

$$G^{\rm NS}_{\pm s}(\eta, s_{10}) = \int \frac{{\rm d}\omega}{2\pi i} e^{\omega\eta} \sum_{n=0}^\infty \frac{1}{n!} \left(\frac{\alpha_s(\eta - s_{10} - y_0)}{2}\right)^n \frac{1}{\omega^{n+2}} = \eta \sum_{n=0}^\infty \frac{1}{(n!)(n+1)!} \left(\frac{\alpha_s}{2}\eta(\eta - s_{10} - y_0)\right)^n\,. \tag{B11}$$

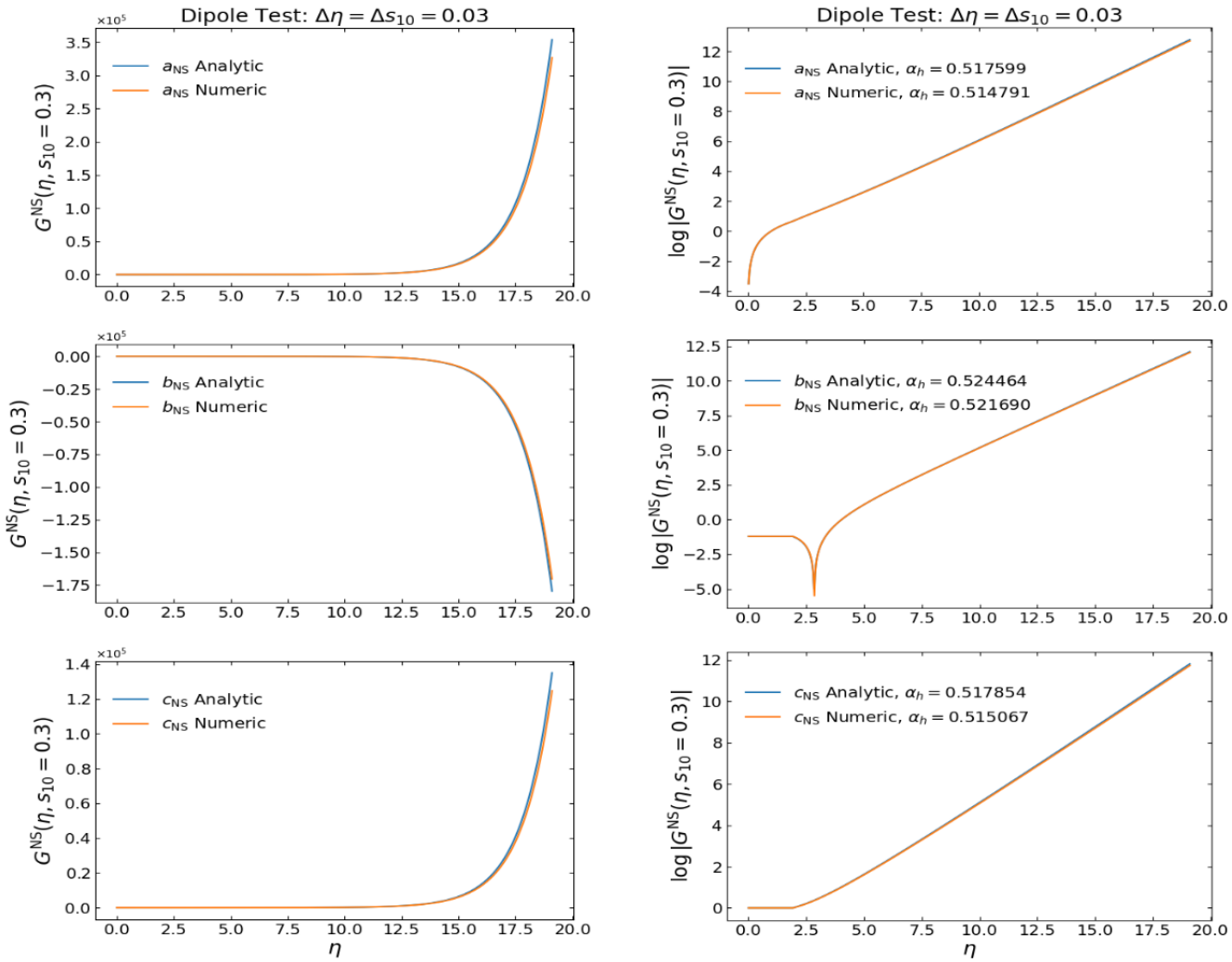

FIG. 19. $G^{\rm NS}(s_{10}, \eta)$ (left) and $\log\left|G^{\rm NS}(s_{10}, \eta)\right|$ (right) plotted as functions of η for a fixed value of $s_{10} = 0.3$. The large-η behavior corresponds to the small-x behavior, and this allows us to see how and when our numerical solution deviates from the analytic. The absolute value of the logarithm allows us to investigate the sign change (the cusp), and the slope of the logarithmic plot will give us a dipole amplitude-level intercept.

This too is proportional to a modified Bessel function of the first kind, now for $m = 1$. The solution is then rewritten as

$$G^{NS,\,\eta}_{\pm s}(\eta, s_{10}) = \frac{1}{\sqrt{\alpha_s}}\sqrt{\frac{2\,\eta}{\eta - s_{10} - y_0}}\, I_1\big(\sqrt{\alpha_s}\sqrt{2\eta(\eta - s_{10} - y_0)}\big). \tag{B12}$$

Lastly, we must solve for the initial condition term $G^{\rm NS}_{\pm s}(\eta, s_{10}) = s_{10}$. Noting that $s_{10} = \eta - (\eta - s_{10} - y_0) - y_0$,

$$G^{\rm NS\,(0)}_{\pm s}(\omega, \lambda) = \int_0^\infty d(\eta - s_{10} - y_0)\, e^{-\lambda(\eta - s_{10} - y_0)} \int_0^\infty {\rm d}\eta\, e^{-\omega\eta}(\eta - (\eta - s_{10} - y_0) - y_0) = \frac{\lambda - \omega - y_0\omega\lambda}{(\omega\lambda)^2}\,. \tag{B13}$$

In this case we have two poles: $\lambda = 0$, $\alpha_s/(2\omega)$. Conveniently, there are no poles in ω at $\lambda = 0$, so that particular integral vanishes. Moving forward with the other λ pole we write

$$\begin{aligned} G^{\rm NS}_{\pm s}(\eta, s_{10}) &= \int \frac{{\rm d}\omega}{2\pi i}\, e^{\omega\eta} \int \frac{{\rm d}\lambda}{2\pi i}\, e^{(\eta - s_{10} - y_0)\lambda}\, \frac{\omega\lambda}{\lambda - \frac{\alpha_s}{2\omega}}\, \frac{1}{\omega}\, \frac{\lambda - \omega - y_0\omega\lambda}{(\omega\lambda)^2} \\ &= \int \frac{{\rm d}\omega}{2\pi i}\, e^{\omega\eta + \frac{\alpha_s}{2\omega}(\eta - s_{10} - y_0)} \left(\frac{1}{\omega^2} - \frac{2}{\alpha_s} - \frac{y_0}{\omega}\right). \end{aligned} \tag{B14}$$

This equation is a linear combination of the two other contributions we derived, plus a new term. This new term can be evaluated in the same way as the previous two. We obtain the following result for the s_{10} contribution:

$$\begin{aligned} G_{\pm s}^{NS,\,s_{10}}(\eta, s_{10}) = &\frac{1}{\sqrt{\alpha_s}}\sqrt{\frac{2\,\eta}{\eta - s_{10} - y_0}}\, I_1\big(\sqrt{\alpha_s}\sqrt{2\eta(\eta - s_{10} - y_0)}\big) \\ &- \frac{1}{\sqrt{\alpha_s}}\sqrt{\frac{2(\eta - s_{10} - y_0)}{\eta}}\, I_1\big(\sqrt{\alpha_s}\sqrt{2\eta(\eta - s_{10} - y_0)}\big) \\ &- y_0\, I_0\big(\sqrt{\alpha_s}\sqrt{2\eta(\eta - s_{10} - y_0)}\big). \end{aligned} \tag{B15}$$

In the end, we arrive at an analytic solution for the flavor nonsinglet evolution equation in the all-s_{10} regime,

$$\begin{aligned} G_{\pm s}^{\rm NS}(\eta, s_{10}) &= a^{\rm NS}\, G_{\pm s}^{NS,\,\eta} + b^{\rm NS}\, G_{\pm s}^{NS,\,s_{10}} + c^{\rm NS}\, G_{\pm s}^{NS,\,1} \\ &= a^{\rm NS}\,\frac{1}{\sqrt{\alpha_s}}\sqrt{\frac{2\,\eta}{\eta - s_{10} - y_0}}\, I_1\big(\sqrt{\alpha_s}\sqrt{2\eta(\eta - s_{10} - y_0)}\big) + \frac{b^{\rm NS}}{\sqrt{\alpha_s}}\sqrt{\frac{2\,\eta}{\eta - s_{10} - y_0}}\, I_1\big(\sqrt{\alpha_s}\sqrt{2\,\eta(\eta - s_{10} - y_0)}\big) \\ &- \frac{b^{\rm NS}}{\sqrt{\alpha_s}}\sqrt{\frac{2(\eta - s_{10} - y_0)}{\eta}}\, I_1\big(\sqrt{\alpha_s}\sqrt{2\eta(\eta - s_{10} - y_0)}\big) - b^{\rm NS} y_0\, I_0\big(\sqrt{\alpha_s}\sqrt{2\eta(\eta - s_{10} - y_0)}\big) \\ &+ c^{\rm NS}\, I_0\big(\sqrt{\alpha_s}\sqrt{2\eta(\eta - s_{10} - y_0)}\big). \end{aligned} \tag{B16}$$

The first place to start our comparisons would be the dipole amplitudes themselves. There are three properties of the flavor nonsinglet dipoles that we can use to cross-check the numerical solution: the general shape of the amplitudes, a sign change in the s_{10} contributions due to the positive starting point and negative growth, and the asymptotic behavior at small x. The latter property is also useful for checking the implementation of our hPDF calculation, since the dipole amplitudes and hPDFs should have the same asymptotics.

We show in Fig. 19 high resolution (small step-size) numerical solutions of the dipole amplitudes, as functions of η for a fixed s_{10}, compared to their analytic counterparts. The general shape and growth of the flavor nonsinglet dipole amplitudes (see the left panels in Fig. 19) shows a good agreement between the numerical and analytic solutions with a reasonably small step-size of $\Delta\eta = \Delta s_{10} = \Delta = 0.03$. One can see that the analytic solution grows in magnitude slightly faster than the numeric solution. The logarithm of the absolute value of the dipole amplitudes, plotted in the right panels of Fig. 19, reveals further quantitative agreement, where we see that the numerical intercept α_h converges to within 1.4% of the analytic solution. The logarithmic scale also allows us to compare the two solutions' large-x (low η) behavior using the location of the sign change (the cusp) in the b_{NS} contribution (the middle right panel of Fig. 19). The lower the fixed s_{10} value, the lower the sign change. We see in Fig. 19 that when $s_{10} = \text{const} = 0.3$ the sign changes coincide just above $\eta = 2.5$, implying that our numerical solution is equally valid as $x \to x_0$. Furthermore, we can delay the sign-change by increasing s_{10} for these plots, and that will allow us to to determine the necessary resolution for retaining agreement as x gets small. This test is given by the left side of Fig. 20, which informs us that a resolution of $\Delta\eta = \Delta s_{10} = \Delta < 0.06$ will retain analytic agreement at the dipole amplitude level. We routinely use $\Delta \leq 0.025$ for our numerics and global analysis.

The dipole amplitude-level agreement gives us confidence to compare how each solution impacts our observables Δq^-. We employ the plots on the right-hand side of Fig. 20 to extract the intercept of the $\ln|\Delta u^-|$ basis functions and confirm that the hPDFs asymptotics given by the analytic and numerical dipole amplitudes match within 1%, and are consistent with the intercept that was computed at the dipole amplitude level. This completes the cross-check of our numerical solution for the flavor nonsinglet evolution equations.

Appendix C: Convergence testing of numerical solutions

The discretization defined in Appendix A is very useful for solving convoluted integral equations which are very difficult if not impossible to solve analytically. The numerical solution is rather straightforward to derive, but it has the same faults as any discrete function, namely the fact that the accuracy of a numerical solution is dependent on the resolution, *i.e.*, the step size. In our case, we have two different variables to work with (η, s_{10}), which results in a two-dimensional grid ($G[i, j]$) for our numerical solution to compute. To simplify the discretization, we defined the step sizes for η and s_{10} to be the same, $\Delta\eta = \Delta s_{10} \equiv \Delta$. The requirement we impose on our numerical solution to confirm its validity is that as the step-size decreases (or as the resolution increases), the computed values should converge to a single output.

We have tested each of our flavor singlet basis functions (Fig. 1) as well as the flavor nonsinglet basis functions (not shown), however, the results can be summarized by their subsequent implementation in calculating the hPDFs

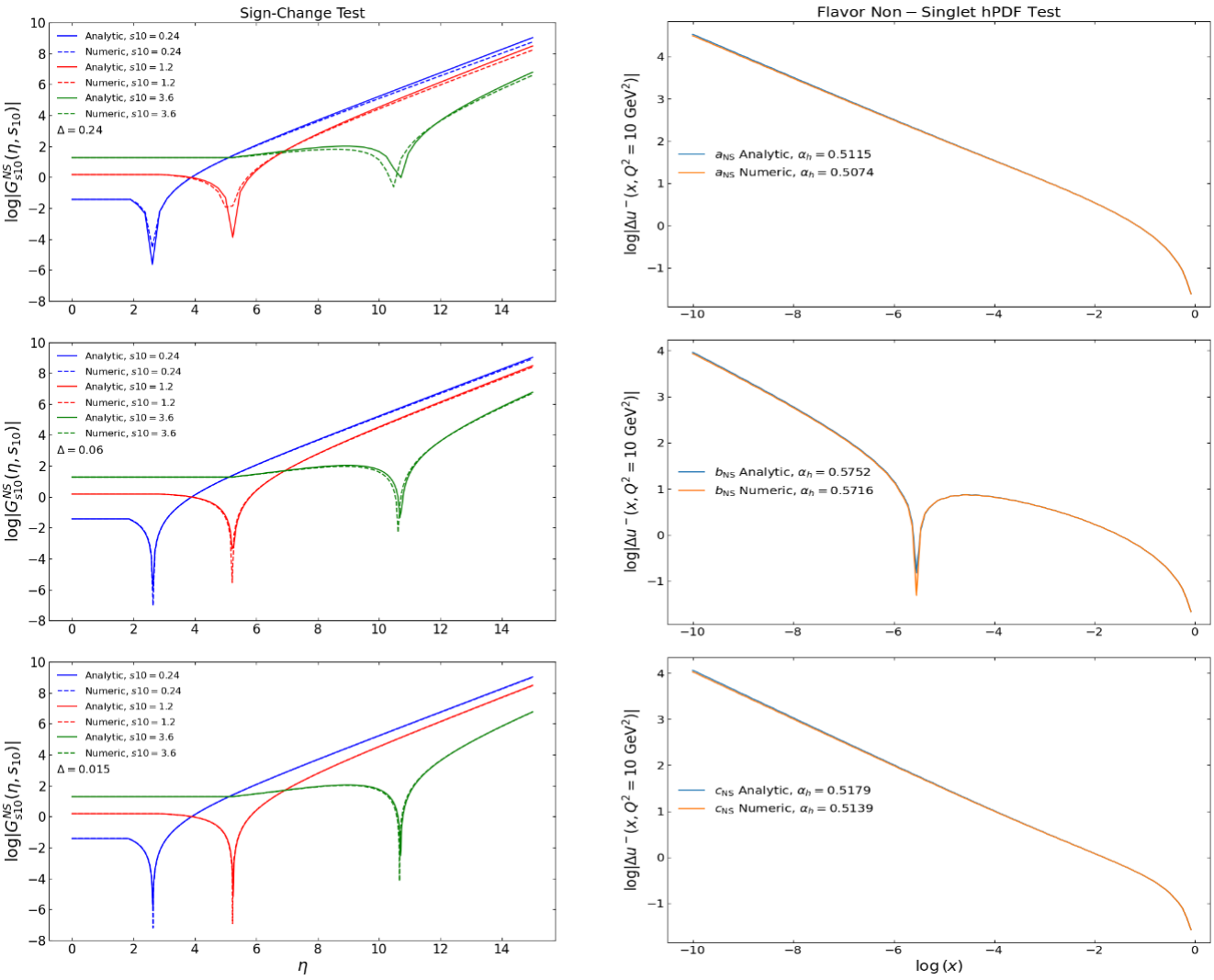

FIG. 20. (Left) A plot of (the logarithm of) the s_{10} contribution to $G_u^{\rm NS}$ (parameterized by $b_u^{\rm NS}$) as a function of η. Each color represents a different fixed value of s_{10}. The location of the sign-change in the amplitude, indicated by the cusp, appears to vary with s_{10}. Smaller step sizes lead to convergence of the sign-change between the analytic and numeric solutions, and $\Delta\eta = \Delta s_{10} = \Delta < 0.06$ retains small-x agreement. (Right) A plot of (the logarithm of) each Δu^- basis functions (parameterized by $a_u^{\rm NS}$, $b_u^{\rm NS}$, and $c_u^{\rm NS}$) as a function of $\log(x)$. Each plot depicts the asymptotic agreement between the numeric and analytic solutions, as well as a measure of the intercept α_h.

$\Delta q^+(x)$ and $\Delta q^-(x)$. The left panel of Fig. 21 shows $x\Delta u^+(x)$ for a "test state" of initial conditions. We define a test state simply as any replica that has been confirmed to fit data with $\frac{\chi^2}{N_{\rm pts}} \approx 1$. This hPDF was plotted multiple times for varying step-sizes, and it is clear that as the step-size decreases the solutions converge to a single output.

The same convergence test was conducted on $x\Delta q^-(x)$ and is displayed in the right panel of Fig. 21. In this case there is also an analytic solution, as discussed in Appendix B. We find not only a convergence of the numerical solution to a single output as Δ becomes smaller, but also that the converged output is exactly that of the analytic solution. We note here that Fig. 21 is a demonstration of the convergence; the results discussed in Sec. III were computed using much higher resolutions $\Delta \approx 0.02$.

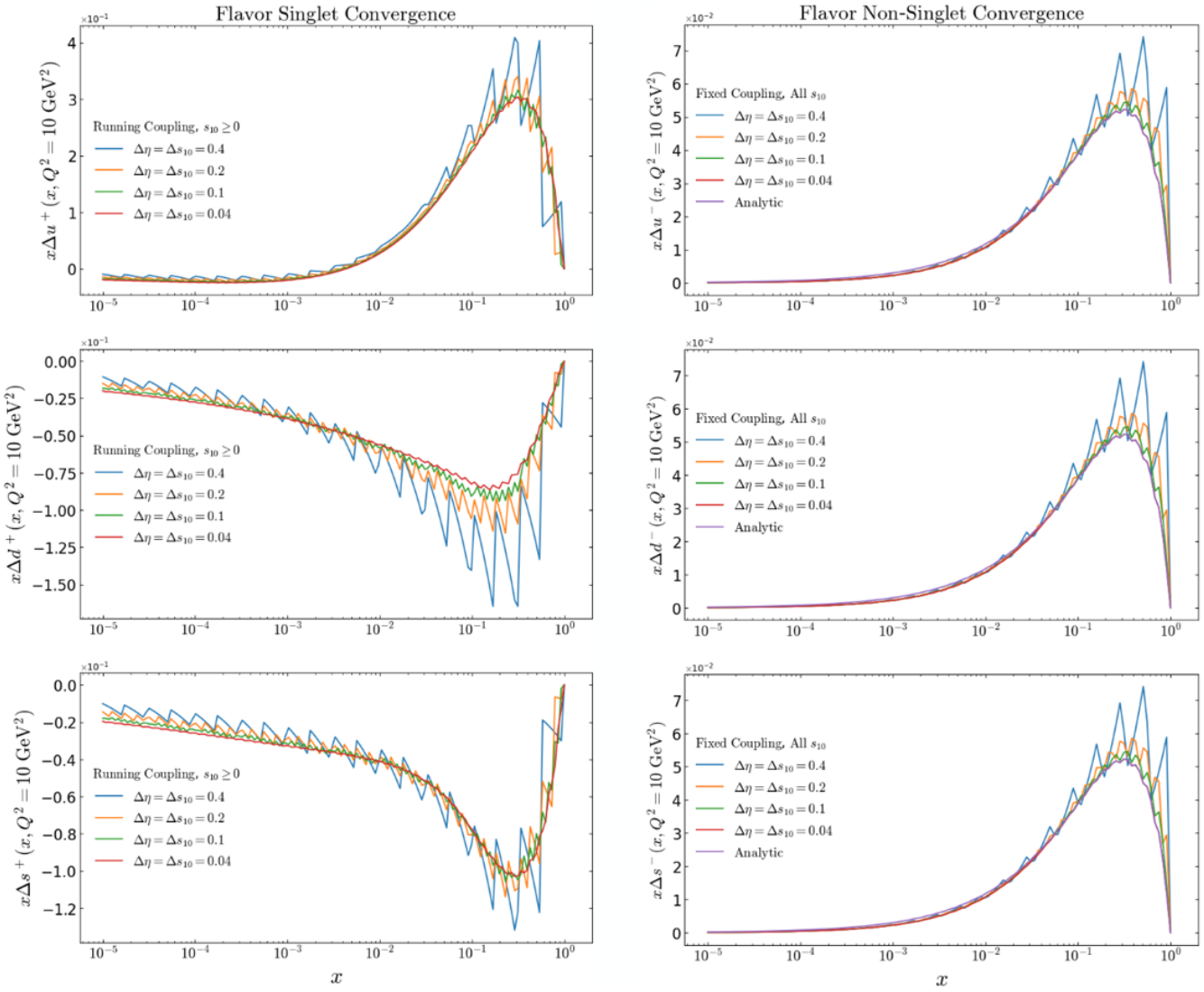

FIG. 21. (Left) A numerical computation of $x\Delta q^+(x)$ for a test state of initial conditions. The graph shows the same numerical solution for various choices of step size, $\Delta = \Delta\eta = \Delta s_{10}$. As the step-size Δ decreases, our numerical solution converges to a single result. (Right) A numerical computation of $x\,\Delta q^-(x)$ that shows the convergence to a single output as Δ decreases. For both $x\Delta q^+(x)$ and $x\Delta q^-(x)$, the single output is described by the analytic solution (B16).

[1] C. A. Aidala, S. D. Bass, D. Hasch and G. K. Mallot, *The Spin Structure of the Nucleon*, *Rev. Mod. Phys.* **85** (2013) 655–691, [1209.2803].

[2] A. Accardi et al., *Electron Ion Collider: The Next QCD Frontier: Understanding the glue that binds us all*, *Eur. Phys. J. A* **52** (2016) 268, [1212.1701].

[3] E. Leader and C. Lorcé, *The angular momentum controversy: What's it all about and does it matter?*, *Phys. Rept.* **541** (2014) 163–248, [1309.4235].

[4] E. C. Aschenauer et al., *The RHIC Spin Program: Achievements and Future Opportunities*, 1304.0079.

[5] E.-C. Aschenauer et al., *The RHIC SPIN Program: Achievements and Future Opportunities*, 1501.01220.

[6] D. Boer et al., *Gluons and the quark sea at high energies: Distributions, polarization, tomography*, 1108.1713.

[7] A. Prokudin, Y. Hatta, Y. Kovchegov and C. Marquet, eds., *Proceedings, Probing Nucleons and Nuclei in High Energy Collisions: Dedicated to the Physics of the Electron Ion Collider: Seattle (WA), United States, October 1 - November 16, 2018*, WSP, 2020. 10.1142/11684.

[8] X. Ji, F. Yuan and Y. Zhao, *What we know and what we don't know about the proton spin after 30 years*, *Nature Rev. Phys.* **3** (2021) 27–38, [2009.01291].

[9] R. Abdul Khalek et al., *Science Requirements and Detector Concepts for the Electron-Ion Collider: EIC Yellow Report*, *Nucl. Phys. A* **1026** (2022) 122447, [2103.05419].

[10] R. L. Jaffe and A. Manohar, *The G(1) Problem: Fact and Fantasy on the Spin of the Proton*, *Nucl. Phys.* **B337** (1990) 509–546.

[11] X. Ji, *Gauge-Invariant Decomposition of Nucleon Spin*, *Phys. Rev. Lett.* **78** (1997) 610–613, [hep-ph/9603249].

[12] S. Bashinsky and R. L. Jaffe, *Quark and gluon orbital angular momentum and spin in hard processes*, *Nucl. Phys.* **B536** (1998) 303–317, [hep-ph/9804397].

[13] P. Hagler and A. Schafer, *Evolution equations for higher moments of angular momentum distributions*, *Phys. Lett.* **B430** (1998) 179–185, [hep-ph/9802362].

[14] A. Harindranath and R. Kundu, *On Orbital angular momentum in deep inelastic scattering*, *Phys. Rev.* **D59** (1999) 116013, [hep-ph/9802406].

[15] Y. Hatta and S. Yoshida, *Twist analysis of the nucleon spin in QCD*, *JHEP* **10** (2012) 080, [1207.5332].

[16] X. Ji, X. Xiong and F. Yuan, *Probing Parton Orbital Angular Momentum in Longitudinally Polarized Nucleon*, *Phys. Rev.* **D88** (2013) 014041, [1207.5221].

[17] V. N. Gribov and L. N. Lipatov, *Deep inelastic e p scattering in perturbation theory*, *Sov. J. Nucl. Phys.* **15** (1972) 438–450.

[18] G. Altarelli and G. Parisi, *Asymptotic Freedom in Parton Language*, *Nucl. Phys.* **B126** (1977) 298.

[19] Y. L. Dokshitzer, *Calculation of the Structure Functions for Deep Inelastic Scattering and e^+e^- Annihilation by Perturbation Theory in Quantum Chromodynamics*, *Sov. Phys. JETP* **46** (1977) 641–653.

[20] M. Gluck, E. Reya, M. Stratmann and W. Vogelsang, *Models for the polarized parton distributions of the nucleon*, *Phys. Rev. D* **63** (2001) 094005, [hep-ph/0011215].

[21] E. Leader, A. V. Sidorov and D. B. Stamenov, *Longitudinal polarized parton densities updated*, *Phys. Rev.* **D73** (2006) 034023, [hep-ph/0512114].

[22] D. de Florian, R. Sassot, M. Stratmann and W. Vogelsang, *Extraction of Spin-Dependent Parton Densities and Their Uncertainties*, *Phys. Rev.* **D80** (2009) 034030, [0904.3821].

[23] E. Leader, A. V. Sidorov and D. B. Stamenov, *Determination of Polarized PDFs from a QCD Analysis of Inclusive and Semi-inclusive Deep Inelastic Scattering Data*, *Phys. Rev. D* **82** (2010) 114018, [1010.0574].

[24] P. Jimenez-Delgado, A. Accardi and W. Melnitchouk, *Impact of hadronic and nuclear corrections on global analysis of spin-dependent parton distributions*, *Phys. Rev. D* **89** (2014) 034025, [1310.3734].

[25] NNPDF collaboration, R. D. Ball, S. Forte, A. Guffanti, E. R. Nocera, G. Ridolfi and J. Rojo, *Unbiased determination of polarized parton distributions and their uncertainties*, *Nucl. Phys.* **B874** (2013) 36–84, [1303.7236].

[26] NNPDF collaboration, E. R. Nocera, R. D. Ball, S. Forte, G. Ridolfi and J. Rojo, *A first unbiased global determination of polarized PDFs and their uncertainties*, *Nucl. Phys.* **B887** (2014) 276–308, [1406.5539].

[27] D. de Florian, R. Sassot, M. Stratmann and W. Vogelsang, *Evidence for polarization of gluons in the proton*, *Phys. Rev. Lett.* **113** (2014) 012001, [1404.4293].

[28] E. Leader, A. V. Sidorov and D. B. Stamenov, *New analysis concerning the strange quark polarization puzzle*, *Phys. Rev.* **D91** (2015) 054017, [1410.1657].

[29] N. Sato, W. Melnitchouk, S. Kuhn, J. Ethier and A. Accardi, *Iterative Monte Carlo analysis of spin-dependent parton distributions*, *Phys. Rev. D* **93** (2016) 074005, [1601.07782].

[30] J. J. Ethier, N. Sato and W. Melnitchouk, *First simultaneous extraction of spin-dependent parton distributions and fragmentation functions from a global QCD analysis*, *Phys. Rev. Lett.* **119** (2017) 132001, [1705.05889].

[31] D. De Florian, G. A. Lucero, R. Sassot, M. Stratmann and W. Vogelsang, *Monte Carlo sampling variant of the DSSV14 set of helicity parton densities*, *Phys. Rev. D* **100** (2019) 114027, [1902.10548].

[32] I. Borsa, G. Lucero, R. Sassot, E. C. Aschenauer and A. S. Nunes, *Revisiting helicity parton distributions at a future electron-ion collider*, *Phys. Rev. D* **102** (2020) 094018, [2007.08300].

[33] Jefferson Lab Angular Momentum (JAM) collaboration, Y. Zhou, N. Sato and W. Melnitchouk, *How well do we know the gluon polarization in the proton?*, *Phys. Rev. D* **105** (2022) 074022, [2201.02075].

[34] Jefferson Lab Angular Momentum (JAM) collaboration, C. Cocuzza, W. Melnitchouk, A. Metz and N. Sato, *Polarized antimatter in the proton from a global QCD analysis*, *Phys. Rev. D* **106** (2022) L031502, [2202.03372].

[35] J. Bartels, B. I. Ermolaev and M. G. Ryskin, *Nonsinglet contributions to the structure function g1 at small x*, *Z. Phys. C* **70** (1996) 273–280, [hep-ph/9507271].

[36] J. Bartels, B. Ermolaev and M. Ryskin, *Flavor singlet contribution to the structure function G(1) at small x*, *Z. Phys. C* **72** (1996) 627–635, [hep-ph/9603204].

[37] V. G. Gorshkov, V. N. Gribov, L. N. Lipatov and G. V. Frolov, *Doubly logarithmic asymptotic behavior in quantum electrodynamics*, *Sov. J. Nucl. Phys.* **6** (1968) 95.

[38] R. Kirschner and L. Lipatov, *Double Logarithmic Asymptotics and Regge Singularities of Quark Amplitudes with Flavor Exchange*, *Nucl. Phys.* **B213** (1983) 122–148.

[39] R. Kirschner, *Reggeon interactions in perturbative QCD*, *Z. Phys. C* **65** (1995) 505–510, [hep-th/9407085].

[40] R. Kirschner, *Regge asymptotics of scattering with flavor exchange in QCD*, *Z. Phys. C* **67** (1995) 459–466, [hep-th/9404158].

[41] S. Griffiths and D. A. Ross, *Studying the perturbative Reggeon*, *Eur. Phys. J. C* **12** (2000) 277–286, [hep-ph/9906550].

[42] L. V. Gribov, E. M. Levin and M. G. Ryskin, *Semihard Processes in QCD*, *Phys. Rept.* **100** (1983) 1–150.

[43] E. Iancu and R. Venugopalan, *The Color glass condensate and high-energy scattering in QCD*. 3, 2003. hep-ph/0303204.

[44] H. Weigert, *Evolution at small x_{bj}: The Color Glass Condensate*, *Prog. Part. Nucl. Phys.* **55** (2005) 461–565,

[hep-ph/0501087].
[45] J. Jalilian-Marian and Y. V. Kovchegov, *Saturation physics and deuteron-Gold collisions at RHIC*, *Prog. Part. Nucl. Phys.* **56** (2006) 104–231, [hep-ph/0505052].
[46] F. Gelis, E. Iancu, J. Jalilian-Marian and R. Venugopalan, *The Color Glass Condensate*, *Ann.Rev.Nucl.Part.Sci.* **60** (2010) 463–489, [1002.0333].
[47] J. L. Albacete and C. Marquet, *Gluon saturation and initial conditions for relativistic heavy ion collisions*, *Prog.Part.Nucl.Phys.* **76** (2014) 1–42, [1401.4866].
[48] Y. V. Kovchegov and E. Levin, *Quantum chromodynamics at high energy*, vol. 33. Cambridge University Press, 2012.
[49] A. Morreale and F. Salazar, *Mining for Gluon Saturation at Colliders*, *Universe* **7** (2021) 312, [2108.08254].
[50] K. Itakura, Y. V. Kovchegov, L. McLerran and D. Teaney, *Baryon stopping and valence quark distribution at small x*, *Nucl. Phys.* **A730** (2004) 160–190, [hep-ph/0305332].
[51] R. Boussarie, Y. Hatta and F. Yuan, *Proton Spin Structure at Small-x*, *Phys. Lett. B* **797** (2019) 134817, [1904.02693].
[52] Y. V. Kovchegov, D. Pitonyak and M. D. Sievert, *Helicity Evolution at Small-x*, *JHEP* **01** (2016) 072, [1511.06737].
[53] Y. Hatta, Y. Nakagawa, F. Yuan, Y. Zhao and B. Xiao, *Gluon orbital angular momentum at small-x*, *Phys. Rev. D* **95** (2017) 114032, [1612.02445].
[54] Y. V. Kovchegov, D. Pitonyak and M. D. Sievert, *Helicity Evolution at Small x: Flavor Singlet and Non-Singlet Observables*, *Phys. Rev. D* **95** (2017) 014033, [1610.06197].
[55] Y. V. Kovchegov, D. Pitonyak and M. D. Sievert, *Small-x asymptotics of the quark helicity distribution*, *Phys. Rev. Lett.* **118** (2017) 052001, [1610.06188].
[56] Y. V. Kovchegov, D. Pitonyak and M. D. Sievert, *Small-x Asymptotics of the Quark Helicity Distribution: Analytic Results*, *Phys. Lett. B* **772** (2017) 136–140, [1703.05809].
[57] Y. V. Kovchegov, D. Pitonyak and M. D. Sievert, *Small-x Asymptotics of the Gluon Helicity Distribution*, *JHEP* **10** (2017) 198, [1706.04236].
[58] Y. V. Kovchegov and M. D. Sievert, *Small-x Helicity Evolution: an Operator Treatment*, *Phys. Rev. D* **99** (2019) 054032, [1808.09010].
[59] Y. V. Kovchegov, *Orbital Angular Momentum at Small x*, *JHEP* **03** (2019) 174, [1901.07453].
[60] F. Cougoulic and Y. V. Kovchegov, *Helicity-dependent generalization of the JIMWLK evolution*, *Phys. Rev. D* **100** (2019) 114020, [1910.04268].
[61] Y. V. Kovchegov and Y. Tawabutr, *Helicity at Small x: Oscillations Generated by Bringing Back the Quarks*, *JHEP* **08** (2020) 014, [2005.07285].
[62] F. Cougoulic and Y. V. Kovchegov, *Helicity-dependent extension of the McLerran-Venugopalan model*, *Nucl. Phys. A* **1004** (2020) 122051, [2005.14688].
[63] G. A. Chirilli, *High-energy Operator Product Expansion at sub-eikonal level*, 2101.12744.
[64] Y. V. Kovchegov, A. Tarasov and Y. Tawabutr, *Helicity Evolution at Small x: the Single-Logarithmic Contribution*, 2104.11765.
[65] F. Cougoulic, Y. V. Kovchegov, A. Tarasov and Y. Tawabutr, *Quark and gluon helicity evolution at small x: revised and updated*, *JHEP* **07** (2022) 095, [2204.11898].
[66] A. H. Mueller, *Soft gluons in the infinite momentum wave function and the BFKL pomeron*, *Nucl. Phys.* **B415** (1994) 373–385.
[67] A. H. Mueller and B. Patel, *Single and double BFKL pomeron exchange and a dipole picture of high-energy hard processes*, *Nucl. Phys.* **B425** (1994) 471–488, [hep-ph/9403256].
[68] A. H. Mueller, *Unitarity and the BFKL pomeron*, *Nucl. Phys.* **B437** (1995) 107–126, [hep-ph/9408245].
[69] I. Balitsky, *Operator expansion for high-energy scattering*, *Nucl. Phys.* **B463** (1996) 99–160, [hep-ph/9509348].
[70] I. Balitsky, *Factorization and high-energy effective action*, *Phys. Rev. D* **60** (1999) 014020, [hep-ph/9812311].
[71] Y. V. Kovchegov, *Small x F(2) structure function of a nucleus including multiple pomeron exchanges*, *Phys. Rev. D* **60** (1999) 034008, [hep-ph/9901281].
[72] Y. V. Kovchegov, *Unitarization of the BFKL pomeron on a nucleus*, *Phys. Rev. D* **61** (2000) 074018, [hep-ph/9905214].
[73] J. Jalilian-Marian, A. Kovner and H. Weigert, *The Wilson renormalization group for low x physics: Gluon evolution at finite parton density*, *Phys. Rev.* **D59** (1998) 014015, [hep-ph/9709432].
[74] J. Jalilian-Marian, A. Kovner, A. Leonidov and H. Weigert, *The Wilson renormalization group for low x physics: Towards the high density regime*, *Phys. Rev.* **D59** (1998) 014014, [hep-ph/9706377].
[75] H. Weigert, *Unitarity at small Bjorken x*, *Nucl. Phys.* **A703** (2002) 823–860, [hep-ph/0004044].
[76] E. Iancu, A. Leonidov and L. D. McLerran, *The Renormalization group equation for the color glass condensate*, *Phys. Lett. B* **510** (2001) 133–144, [hep-ph/0102009].
[77] E. Iancu, A. Leonidov and L. D. McLerran, *Nonlinear gluon evolution in the color glass condensate. 1.*, *Nucl. Phys.* **A692** (2001) 583–645, [hep-ph/0011241].
[78] E. Ferreiro, E. Iancu, A. Leonidov and L. McLerran, *Nonlinear gluon evolution in the color glass condensate. 2.*, *Nucl. Phys.* **A703** (2002) 489–538, [hep-ph/0109115].
[79] T. Altinoluk, N. Armesto, G. Beuf, M. Martinez and C. A. Salgado, *Next-to-eikonal corrections in the CGC: gluon production and spin asymmetries in pA collisions*, *JHEP* **07** (2014) 068, [1404.2219].
[80] I. Balitsky and A. Tarasov, *Rapidity evolution of gluon TMD from low to moderate x*, *JHEP* **10** (2015) 017, [1505.02151].
[81] I. Balitsky and A. Tarasov, *Gluon TMD in particle production from low to moderate x*, *JHEP* **06** (2016) 164, [1603.06548].

[82] G. A. Chirilli, *Sub-eikonal corrections to scattering amplitudes at high energy*, *JHEP* **01** (2019) 118, [1807.11435].

[83] J. Jalilian-Marian, *Quark jets scattering from a gluon field: from saturation to high p_t*, *Phys. Rev.* **D99** (2019) 014043, [1809.04625].

[84] J. Jalilian-Marian, *Rapidity loss, spin and angular asymmetries in scattering of a quark from color field of a proton (nucleus)*, 1912.08878.

[85] T. Altinoluk, G. Beuf, A. Czajka and A. Tymowska, *Quarks at next-to-eikonal accuracy in the CGC I: Forward quark-nucleus scattering*, 2012.03886.

[86] Y. V. Kovchegov and M. G. Santiago, *Quark sivers function at small x: spin-dependent odderon and the sub-eikonal evolution*, *JHEP* **11** (2021) 200, [2108.03667].

[87] T. Altinoluk and G. Beuf, *Quark and scalar propagators at next-to-eikonal accuracy in the CGC through a dynamical background gluon field*, 2109.01620.

[88] Y. V. Kovchegov and M. G. Santiago, *T-odd leading-twist quark TMDs at small x*, *JHEP* **11** (2022) 098, [2209.03538].

[89] T. Altinoluk, G. Beuf, A. Czajka and A. Tymowska, *DIS dijet production at next-to-eikonal accuracy in the CGC*, 2212.10484.

[90] T. Altinoluk, N. Armesto and G. Beuf, *Probing quark transverse momentum distributions in the Color Glass Condensate: quark-gluon dijets in Deep Inelastic Scattering at next-to-eikonal accuracy*, 2303.12691.

[91] T. Altinoluk, G. Beuf and J. Jalilian-Marian, *Renormalization of the gluon distribution function in the background field formalism*, 2305.11079.

[92] M. Li, *Small x Physics Beyond Eikonal Approximation: an Effective Hamiltonian Approach*, 2304.12842.

[93] G. 't Hooft, *A Planar Diagram Theory for Strong Interactions*, *Nucl. Phys. B* **72** (1974) 461.

[94] G. Veneziano, *Some Aspects of a Unified Approach to Gauge, Dual and Gribov Theories*, *Nucl. Phys. B* **117** (1976) 519–545.

[95] J. Borden and Y. V. Kovchegov, *Analytic Solution for the Revised Helicity Evolution at Small x and Large N_c: New Resummed Gluon-Gluon Polarized Anomalous Dimension and Intercept*, 2304.06161.

[96] D. Adamiak, Y. V. Kovchegov and Y. Tawabutr, *Helicity Evolution at Small x: Revised Asymptotic Results at Large N_c&N_f*, 2306.01651.

[97] Jefferson Lab Angular Momentum collaboration, D. Adamiak, Y. V. Kovchegov, W. Melnitchouk, D. Pitonyak, N. Sato and M. D. Sievert, *First analysis of world polarized DIS data with small-x helicity evolution*, *Phys. Rev. D* **104** (2021) L031501, [2102.06159].

[98] B. Lampe and E. Reya, *Spin physics and polarized structure functions*, *Phys. Rept.* **332** (2000) 1–163, [hep-ph/9810270].

[99] E. B. Zijlstra and W. L. van Neerven, *Order-α_s^2 corrections to the polarized structure function $g_1(x,Q^2)$*, *Nucl. Phys. B* **417** (1994) 61–100.

[100] R. Mertig and W. L. van Neerven, *The Calculation of the two loop spin splitting functions P(ij)(1)(x)*, *Z. Phys. C* **70** (1996) 637–654, [hep-ph/9506451].

[101] S. Moch and J. A. M. Vermaseren, *Deep inelastic structure functions at two loops*, *Nucl. Phys. B* **573** (2000) 853–907, [hep-ph/9912355].

[102] W. L. van Neerven and A. Vogt, *NNLO evolution of deep inelastic structure functions: The Singlet case*, *Nucl. Phys. B* **588** (2000) 345–373, [hep-ph/0006154].

[103] J. A. M. Vermaseren, A. Vogt and S. Moch, *The Third-order QCD corrections to deep-inelastic scattering by photon exchange*, *Nucl. Phys. B* **724** (2005) 3–182, [hep-ph/0504242].

[104] S. Moch, J. A. M. Vermaseren and A. Vogt, *The Three-Loop Splitting Functions in QCD: The Helicity-Dependent Case*, *Nucl. Phys. B* **889** (2014) 351–400, [1409.5131].

[105] J. Blümlein, P. Marquard, C. Schneider and K. Schönwald, *The three-loop polarized singlet anomalous dimensions from off-shell operator matrix elements*, *JHEP* **01** (2022) 193, [2111.12401].

[106] J. Blümlein and M. Saragnese, *The N3LO scheme-invariant QCD evolution of the non-singlet structure functions F2NS(x,Q2) and g1NS(x,Q2)*, *Phys. Lett. B* **820** (2021) 136589, [2107.01293].

[107] J. Davies, C. H. Kom, S. Moch and A. Vogt, *Resummation of small-x double logarithms in QCD: inclusive deep-inelastic scattering*, *JHEP* **08** (2022) 135, [2202.10362].

[108] J. Blümlein, P. Marquard, C. Schneider and K. Schönwald, *The massless three-loop Wilson coefficients for the deep-inelastic structure functions F_2, F_L, xF_3 and g_1*, *JHEP* **11** (2022) 156, [2208.14325].

[109] G. Altarelli, R. K. Ellis and G. Martinelli, *Large Perturbative Corrections to the Drell-Yan Process in QCD*, *Nucl. Phys. B* **157** (1979) 461–497.

[110] V. S. Fadin and L. N. Lipatov, *BFKL pomeron in the next-to-leading approximation*, *Phys. Lett.* **B429** (1998) 127–134, [hep-ph/9802290].

[111] M. Ciafaloni and G. Camici, *Energy scale(s) and next-to-leading BFKL equation*, *Phys. Lett.* **B430** (1998) 349–354, [hep-ph/9803389].

[112] B. I. Ermolaev, M. Greco and S. I. Troian, *QCD running coupling effects for the nonsinglet structure function at small x*, *Nucl. Phys.* **B571** (2000) 137–150, [hep-ph/9906276].

[113] B. I. Ermolaev, M. Greco and S. I. Troyan, *Running coupling effects for the singlet structure function g_1 at small x*, *Phys. Lett.* **B579** (2004) 321–330, [hep-ph/0307128].

[114] J. L. Albacete, N. Armesto, J. G. Milhano and C. A. Salgado, *Non-linear QCD meets data: A Global analysis of lepton-proton scattering with running coupling BK evolution*, *Phys. Rev. D* **80** (2009) 034031, [0902.1112].

[115] J. L. Albacete, N. Armesto, J. G. Milhano, P. Quiroga-Arias and C. A. Salgado, *AAMQS: A non-linear QCD analysis of new HERA data at small-x including heavy quarks*, *Eur. Phys. J. C* **71** (2011) 1705, [1012.4408].

[116] I. Balitsky, *Quark contribution to the small-x evolution of color dipole*, *Phys. Rev. D* **75** (2007) 014001, [hep-ph/0609105].

[117] E. Gardi, J. Kuokkanen, K. Rummukainen and H. Weigert, *Running coupling and power corrections in nonlinear evolution at the high-energy limit*, *Nucl. Phys.* **A784** (2007) 282–340, [hep-ph/0609087].

[118] Y. V. Kovchegov and H. Weigert, *Triumvirate of Running Couplings in Small-x Evolution*, *Nucl. Phys.* **A784** (2007) 188–226, [hep-ph/0609090].

[119] Y. V. Kovchegov and H. Weigert, *Quark loop contribution to BFKL evolution: Running coupling and leading-N(f) NLO intercept*, *Nucl. Phys.* **A789** (2007) 260–284, [hep-ph/0612071].

[120] J. L. Albacete and Y. V. Kovchegov, *Solving high energy evolution equation including running coupling corrections*, *Phys. Rev.* **D75** (2007) 125021, [arXiv:0704.0612 [hep-ph]].

[121] E. A. Kuraev, L. N. Lipatov and V. S. Fadin, *The Pomeranchuk Singularity in Nonabelian Gauge Theories*, *Sov. Phys. JETP* **45** (1977) 199–204.

[122] I. I. Balitsky and L. N. Lipatov, *The Pomeranchuk Singularity in Quantum Chromodynamics*, *Sov. J. Nucl. Phys.* **28** (1978) 822–829.

[123] D. de Florian, C. A. Garcia Canal and R. Sassot, *Factorization in semiinclusive polarized deep inelastic scattering*, *Nucl. Phys. B* **470** (1996) 195–210, [hep-ph/9510262].

[124] A. Bacchetta, M. Diehl, K. Goeke, A. Metz, P. J. Mulders and M. Schlegel, *Semi-inclusive deep inelastic scattering at small transverse momentum*, *JHEP* **02** (2007) 093, [hep-ph/0611265].

[125] A. Signori, A. Bacchetta, M. Radici and G. Schnell, *Investigations into the flavor dependence of partonic transverse momentum*, *JHEP* **11** (2013) 194, [1309.3507].

[126] A. Dumitru, A. Hayashigaki and J. Jalilian-Marian, *The Color glass condensate and hadron production in the forward region*, *Nucl. Phys. A* **765** (2006) 464–482, [hep-ph/0506308].

[127] G. A. Chirilli, B.-W. Xiao and F. Yuan, *One-loop Factorization for Inclusive Hadron Production in pA Collisions in the Saturation Formalism*, *Phys. Rev. Lett.* **108** (2012) 122301, [1112.1061].

[128] G. A. Chirilli, B.-W. Xiao and F. Yuan, *Inclusive Hadron Productions in pA Collisions*, *Phys. Rev.* **D86** (2012) 054005, [1203.6139].

[129] L. L. Frankfurt, M. I. Strikman, L. Mankiewicz, A. Schafer, E. Rondio, A. Sandacz et al., *The Valence and Strange Sea Quark Spin Distributions in the Nucleon From Semiinclusive Deep Inelastic Lepton Scattering*, *Phys. Lett. B* **230** (1989) 141–148.

[130] D. de Florian, L. N. Epele, H. Fanchiotti, C. A. Garcia Canal, S. Joffily and R. Sassot, *Next-to-leading order semiinclusive spin asymmetries*, *Phys. Lett. B* **389** (1996) 358–366, [hep-ph/9603302].

[131] V. Alexakhin, Y. Alexandrov, G. Alexeev, A. Amoroso, B. Badełek, F. Balestra et al., *Spin asymmetry a1d and the spin-dependent structure function g1d of the deuteron at low values of x and q2*, *Physics Letters B* **647** (2007) 330–340.

[132] T. Hobbs and W. Melnitchouk, *Finite-Q**2 corrections to parity-violating DIS*, *Phys. Rev. D* **77** (2008) 114023, [0801.4791].

[133] Y. Zhao, A. Deshpande, J. Huang, K. Kumar and S. Riordan, *Neutral-Current Weak Interactions at an EIC*, *Eur. Phys. J. A* **53** (2017) 55, [1612.06927].

[134] D. Wang, *Measurement of the Parity-Violating Asymmetry in Deep Inelastic Scattering at JLab 6 GeV*, Ph.D. thesis, Virginia U., 2013. 10.2172/1133072.

[135] JAM collaboration, N. Sato, C. Andres, J. J. Ethier and W. Melnitchouk, *Strange quark suppression from a simultaneous Monte Carlo analysis of parton distributions and fragmentation functions*, *Phys. Rev. D* **101** (2020) 074020, [1905.03788].

[136] E. Moffat, W. Melnitchouk, T. Rogers and N. Sato, *Simultaneous Monte Carlo analysis of parton densities and fragmentation functions*, 2101.04664.

[137] E142 Collaboration collaboration, P. L. Anthony et al., *Deep inelastic scattering of polarized electrons by polarized He-3 and the study of the neutron spin structure*, *Phys. Rev. D* **54** (1996) 6620–6650, [hep-ex/9610007].

[138] E154 Collaboration collaboration, K. Abe et al., *Precision determination of the neutron spin structure function g1(n)*, *Phys. Rev. Lett.* **79** (1997) 26–30, [hep-ex/9705012].

[139] E143 Collaboration collaboration, K. Abe et al., *Measurements of the proton and deuteron spin structure functions g(1) and g(2)*, *Phys. Rev. D* **58** (1998) 112003, [hep-ph/9802357].

[140] E155 Collaboration collaboration, P. L. Anthony et al., *Measurement of the deuteron spin structure function g1(d)(x) for 1-(GeV/c)**2 < Q**2 < 40-(GeV/c)**2*, *Phys. Lett. B* **463** (1999) 339–345, [hep-ex/9904002].

[141] E155 Collaboration collaboration, P. L. Anthony et al., *Measurements of the Q**2 dependence of the proton and neutron spin structure functions g(1)**p and g(1)**n*, *Phys. Lett. B* **493** (2000) 19–28, [hep-ph/0007248].

[142] European Muon Collaboration collaboration, J. Ashman et al., *An Investigation of the Spin Structure of the Proton in Deep Inelastic Scattering of Polarized Muons on Polarized Protons*, *Nucl. Phys.* **B328** (1989) 1.

[143] Spin Muon Collaboration collaboration, B. Adeva et al., *Spin asymmetries A(1) and structure functions g1 of the proton and the deuteron from polarized high-energy muon scattering*, *Phys. Rev. D* **58** (1998) 112001.

[144] Spin Muon collaboration, B. Adeva et al., *Spin asymmetries A(1) and structure functions g1 of the proton and the deuteron from polarized high-energy muon scattering*, *Phys. Rev. D* **58** (1998) 112001.

[145] Spin Muon Collaboration collaboration, B. Adeva et al., *Spin asymmetries A(1) of the proton and the deuteron in the low x and low Q**2 region from polarized high-energy muon scattering*, *Phys. Rev. D* **60** (1999) 072004.

[146] COMPASS Collaboration collaboration, M. G. Alekseev et al., *The Spin-dependent Structure Function of the Proton g_1^p and a Test of the Bjorken Sum Rule*, *Phys. Lett. B* **690** (2010) 466–472, [1001.4654].

[147] COMPASS Collaboration collaboration, C. Adolph et al., *The spin structure function g_1^p of the proton and a test of the Bjorken sum rule*, *Phys. Lett. B* **753** (2016) 18–28, [1503.08935].

[148] COMPASS collaboration, C. Adolph et al., *Final COMPASS results on the deuteron spin-dependent structure function g_1^d and the Bjorken sum rule*, *Phys. Lett. B* **769** (2017) 34–41, [1612.00620].

[149] HERMES Collaboration collaboration, K. Ackerstaff et al., *Measurement of the neutron spin structure function g1(n) with a polarized He-3 internal target*, *Phys. Lett. B* **404** (1997) 383–389, [hep-ex/9703005].

[150] HERMES Collaboration collaboration, A. Airapetian et al., *Precise determination of the spin structure function g(1) of the proton, deuteron and neutron*, *Phys. Rev. D* **75** (2007) 012007, [hep-ex/0609039].

[151] Spin Muon collaboration, B. Adeva et al., *Polarized quark distributions in the nucleon from semiinclusive spin asymmetries*, *Phys. Lett. B* **420** (1998) 180–190, [hep-ex/9711008].

[152] COMPASS collaboration, M. G. Alekseev et al., *Quark helicity distributions from longitudinal spin asymmetries in muon-proton and muon-deuteron scattering*, *Phys. Lett. B* **693** (2010) 227–235, [1007.4061].

[153] COMPASS collaboration, M. Alekseev et al., *Flavour Separation of Helicity Distributions from Deep Inelastic Muon-Deuteron Scattering*, *Phys. Lett. B* **680** (2009) 217–224, [0905.2828].

[154] HERMES collaboration, A. Airapetian et al., *Quark helicity distributions in the nucleon for up, down, and strange quarks from semi-inclusive deep-inelastic scattering*, *Phys. Rev. D* **71** (2005) 012003, [hep-ex/0407032].

[155] HERMES collaboration, K. Ackerstaff et al., *Flavor decomposition of the polarized quark distributions in the nucleon from inclusive and semiinclusive deep inelastic scattering*, *Phys. Lett. B* **464** (1999) 123–134, [hep-ex/9906035].

[156] F. E. Close and R. Roberts, *Consistent analysis of the spin content of the nucleon*, *Physics Letters B* **316** (1993) 165–171.

[157] Particle Data Group collaboration, R. L. Workman et al., *Review of Particle Physics*, *PTEP* **2022** (2022) 083C01.

[158] ECCE Consortium collaboration, *EIC Comprehensive Chromodynamics Experiment Collaboration Detector Proposal*, .

[159] Jefferson Lab Angular Momentum (JAM) collaboration, Y. Zhou, C. Cocuzza, F. Delcarro, W. Melnitchouk, A. Metz and N. Sato, *Revisiting quark and gluon polarization in the proton at the EIC*, *Phys. Rev. D* **104** (2021) 034028, [2105.04434].

[160] J. Collins, T. C. Rogers and N. Sato, *Positivity and renormalization of parton densities*, *Phys. Rev. D* **105** (2022) 076010, [2111.01170].

[161] H. Müller and R. Dingle, *Asymptotic expansions of mathieu functions and their characteristic numbers.*, *Journal für die reine und angewandte Mathematik (Crelles Journal)* (1962) .

[162] R. E. O'Malley and R. E. O'Malley, *The method of matched asymptotic expansions and its generalizations*, *Historical Developments in Singular Perturbations* (2014) 53–121.

[163] Y. Feng and H.-F. Zhang, *Double longitudinal-spin asymmetries in J/ψ production at RHIC*, *JHEP* **11** (2018) 136, [1809.04894].

[164] A. Dumitru and R. Paatelainen, *Sub-femtometer scale color charge fluctuations in a proton made of three quarks and a gluon*, *Phys. Rev. D* **103** (2021) 034026, [2010.11245].

[165] G. Altarelli and G. G. Ross, *The Anomalous Gluon Contribution to Polarized Leptoproduction*, *Phys. Lett.* **B212** (1988) 391–396.

[166] G. M. Shore and G. Veneziano, *The U(1) Goldberger-Treiman relation and the proton 'spin': A Renormalization group analysis*, *Nucl. Phys. B* **381** (1992) 23–65.

[167] A. Tarasov and R. Venugopalan, *Role of the chiral anomaly in polarized deeply inelastic scattering: Finding the triangle graph inside the box diagram in Bjorken and Regge asymptotics*, *Phys. Rev. D* **102** (2020) 114022, [2008.08104].

[168] A. Tarasov and R. Venugopalan, *Role of the chiral anomaly in polarized deeply inelastic scattering. II. Topological screening and transitions from emergent axionlike dynamics*, *Phys. Rev. D* **105** (2022) 014020, [2109.10370].

[169] S. Bhattacharya, Y. Hatta and W. Vogelsang, *Chiral and trace anomalies in deeply virtual Compton scattering*, *Phys. Rev. D* **107** (2023) 014026, [2210.13419].

[170] S. Bhattacharya, Y. Hatta and W. Vogelsang, *Chiral and trace anomalies in Deeply Virtual Compton Scattering II: QCD factorization and beyond*, 2305.09431.